DELFT UNIVERSITY OF TECHNOLOGY

FACULTY OF AEROSPACE ENGINEERING

Master of Science Thesis – 8 April 2016

Lamb Wave Propagation in Sandwich Composite Structures

- For the Detection of Impact Damage -

Ewoud Aaij


TECHNISCHE UNIVERSITEIT DELFT
MDCCCXLII

LAMB WAVE PROPAGATION IN SANDWICH COMPOSITE STRUCTURES

- FOR THE DETECTION OF IMPACT DAMAGE -

MASTER OF SCIENCE THESIS

For obtaining the degree of Master of Science in Aerospace Engineering at Delft University of Technology

Ewoud Aaij

8 April 2016

Faculty of Aerospace Engineering – Delft University of Technology

DELFT UNIVERSITY OF TECHNOLOGY

FACULTY OF AEROSPACE ENGINEERING

DEPARTMENT OF AEROSPACE STRUCTURES AND MATERIALS

STRUCTURAL INTEGRITY & COMPOSITES CHAIR

Graduation committee

Dated: 8 April 2016

Chair holder:

Prof.dr.ir. R. Benedictus

Committee members:

Dr. M.J. Martinez

Dr. W.J.C. Verhagen

Abstract

Lightweight composite sandwich structures are particularly susceptible to impact damage. Barely Visible Impact Damage (BVID) is known to affect the short and long term load bearing capacities of composite structures. Active acoustic Structural Health Monitoring (SHM) systems have the potential to detect such damages before they lead to structural failure, and could thus be applied in a condition based maintenance approach for the DragonFly fuselage.

This study was aimed at increasing the level of understanding on the propagation of ultrasonic (Lamb) waves through sandwich composite media and its response to the DragonFly fuselage structural integrity. These two aspects were combined to arrive at a theoretical prediction on the influence of BVID on the through-transmitted signal in an active acoustic SHM system with a pitch-catch setup. The propagation mode and impact response were verified experimentally. A Finite Element (FE) model was created to verify the predictive power of the FE modelling technique for the specific application of active acoustic SHM.

Two Lamb wave propagation modes were identified both theoretically and experimentally: the Global Lamb Wave mode and the Leaky Lamb Wave mode. Occurrence of these modes was dependent on the central frequency of the transmitted acoustic signal and the bulk wave velocities in the sandwich structure's core compared to the Lamb wave mode propagation velocity in the structure's skins. Other modes (True modes and Rayleigh modes) were identified theoretically, but could not be experimentally confirmed. It was expected and shown experimentally that the presence of impact damage on the propagation path of a signal with 120kHz central frequency reduced the time travelled by this signal between two points, while increasing the amount of energy lost. The latter effect was shown to be reversed at 160kHz, which was explained by the propagation of the signal at this frequency as Leaky Lamb Wave. The FE model could predict the overall trend at 120kHz, but not the exact magnitude of the influence of impact damage on the through-transmitted signal.

Acknowledgements

In my endeavour to obtain the degree of Master of Science in Aerospace Engineering I received support from many people: friends and family, colleagues and supervisors at work, fellow students and instructors at TU Delft University. But there are two people that I should thank the most, which is why I reserve the remainder of this page for them.

First and foremost, the completion of this thesis, and with that, my Masters would not have been possible without the continuous support of my wife. Her faith and understanding kept me focused on finishing my studies despite the many priorities our life confronted us with, most recently the birth of our beautiful daughter.

Second, I would like to thank my supervisor Dr. Marcias Martinez for his advice and guidance, and for setting the bar high even though my situation did not always allow me to dedicate myself fully to my graduation research.

Abbreviations

ASTM	American Society for Testing and Materials
BVID	Barely Visible Impact Damage
CAI	Compressive strength After Impact
CF	Carbon Fibre
CFRP	Carbon Fibre Reinforced Plastic
DSE	Design Synthesis Exercise
FAI	Fatigue life After Impact
FC	Fibre Composite
FE	Finite Element
FRP	Fibre Reinforced Plastic
GFRP	Glass Fibre Reinforced Plastic
GLW	Global Lamb Wave
HM	High Modulus
LLW	Leaky Lamb Wave
NDE	Non-Destructive Evaluation
PMI	Polymethacrylimide
PWAS	Piezoelectric Waver Active Sensors
RW	Rayleigh Wave
SH	Shear Horizontal
SHM	Structural Heath Monitoring
SPA	Sampling Phased Array
TAI	Tensile strength After Impact
TBD	To Be Determined
ToA	Time of Arrival
ToF	Time of Flight
UAV	Unmanned Aerial Vehicle
UD	Uni-Directional
WT	Wavelet Transform

Symbols

a	Diameter of area containing matrix cracks
A_0	Fundamental asymmetric mode
A_1	First asymmetric mode
b	Diameter of area containing debonding
c	Diameter of area containing crushed core
c_g	Group velocity
c_L	Bulk longitudinal velocity
c_p	Phase velocity
c_R	Rayleigh wave velocity
c_S	Bulk shear velocity
d	Period
de	Element size
E	Tensile modulus
f	Frequency
G	Shear modulus
h	Panel thickness
h_C	Core thickness
H	Drop height
m	Mass
N	Number of cycles in a tone burst
r	Error
S_0	Fundamental symmetric mode
S_1	First symmetric mode
t	Time
v	Velocity
V	Volume fraction
|WT|	Magnitude of the wavelet transform
γ	Wave number
θ	Radiation angle
λ	Wave length
ν	Poisson's ratio
ρ	Density
ω	Angular frequency
ω_C	Central frequency

Table of Contents

List of Figures

List of Tables

1 Introduction

In 2012/2013 a Design Synthesis Exercise (DSE) was conducted, leading to the design of a solar powered amphibious Unmanned Aerial Vehicle (UAV), called DragonFly (Martinez 2013). The primary mission of the DragonFly was surveillance of the maritime waters around the coasts of Curaçao (Netherland Antilles). For this purpose, the DragonFly was required to operate autonomously and for an extended period of time. Since the recharge rate was insufficient to allow for continuous flight, the DragonFly was designed to land and take off on water.

Starting from the DSE design, a realization project was defined in the Structures and Materials department to give graduating students the experience of working on an actual aircraft. At the current stage, the aim of this project is to produce a real size prototype incorporating Structural Health Monitoring (SHM) and load monitoring systems as part of the structure. Currently, the research team does not yet cover manufacturing of the hull of the prototype.

Since the DragonFly is operating autonomously it is beneficial to be able to monitor the structural health throughout the mission. This potentially extends the mission duration, as less downtime for inspection would be required. In addition, early detection of damage on the structure will allow for a condition based maintenance approach of the structure.

The hull of the DragonFly (see Figure 1) will be made of a lightweight Glass Fibre Reinforced Plastic (GFRP) sandwich structure. Such a structure is extremely sensitive to impact. Even if impact damage is not visible, the damage area can grow due to continued loading of the structure and ingress of (sea) water, eventually leading to loss of function. Early detection of impact damage in the hull could therefore greatly improve the reliability of the structure. To this end, an active SHM system relying on acoustic signals is proposed.

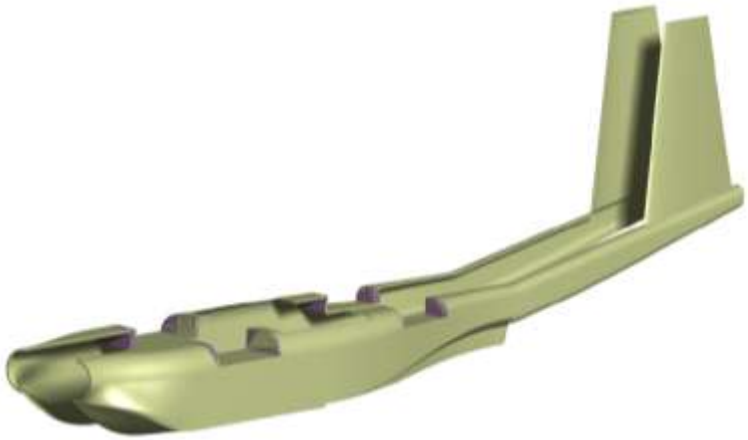

Figure 1 | Hull assembly rendering (Martinez 2013).

1.1 Structural Health Monitoring

Structural Health Monitoring is a field of engineering that deals with the identification, localization and quantification of damage in a structure. Staszewski (2009) proposed a categorization into active and passive SHM approaches. Active SHM systems involve actuation or excitation of the structure and consecutive measurement of the structure's response. Passive

systems do not require actuation, but measure the response of the structure to a damage event directly. The case studies Staszewski (2009) presented for the detection of impact damage showed that an active approach based on lamb wave response was more suitable for detection and measurement of the severity of impact damage. A passive approach based on acoustic emission was more suitable for impact location estimation. It was also noted that for anisotropic materials the passive approach relied on structural analysis to relate impact energy to structural damage, which introduced a source of error.

Another categorization of SHM approaches can be based on the nature of the signal used to measure the condition of the structure. The most common SHM technique used for composites is ultrasonic testing using pitch-catch or pulse-echo setups. Relying on the detection of reflected waves from damage locations, the pulse-echo setup is a powerful technique for both the identification and location of damage, as well as assessment of its magnitude. The pitch-catch setup relies on detection of a through-transmitted wave, where the damage existence and magnitude are derived from a comparison between the received signal and an undamaged baseline. Although this technique has high sensitivity, damage localization is more challenging since damage can only be detected when it is situated between the transmitter and a receiver. Pulse-echo and pitch-catch techniques have been applied widely in active acoustic SHM using Piezo-electric Wafer Active Sensors (PWAS).

Studies on the application of acoustics for SHM in composite materials are abundant. Some good examples of laboratory scale applications are presented by Staszewski (2009) and Raghavan and Cesnik (2007). Active SHM approaches based on acoustics employ guided waves (see section 3) that are generated in the structure and captured using sensor networks or phased arrays. Such SHM systems rely on the distinctive response of the structure in undamaged and damaged state to ultrasonic excitation utilizing for example a piezoceramic actuator. Any deviation in the structure from the undamaged baseline will cause the time and frequency response of the structure to be different. Sensors can be incorporated in or bonded to the structure to derive the presence, severity and location of damage by comparing the measured response to the response of the structure in an undamaged state.

There are two basic setups possible for active acoustic SHM incorporated into the structure: networks or phased arrays. In a network, a combination of actuators, sensors and/or transducers is used to create radiant guided waves and measure the structure's response. The damage location can be triangulated from the individual sensor readings. Phased transducer arrays are used to create a wave front and measure the echo or interference from damage sites. A detailed overview of network and array geometries is given by Rocha (2013), together with an introduction to response analysis.

Challenges in active acoustic SHM system design include determination of the proper signal frequencies and extraction of distinctive features from the response. Even more challenging is the research to the influence of material anisotropy, environmental conditions, operational conditions and structural geometry. For example, struts and stringers introduce boundary conditions to the structure that influence the propagation of acoustic signals, including reflection at the boundaries. The acoustic characteristics of a structure are also determined by the mechanical properties of the

material used. These are influenced by temperature, humidity and other environmental and operational conditions. In addition, they depend on the direction of wave propagation when anisotropic materials are concerned.

In overcoming these challenges, modelling of acoustic wave propagation and the interaction with damage can be of great importance. The influence of for example structural geometry suggests that findings on test specimen cannot readily be extended to the structure as a whole, which introduces the need for full scale specimens. However, modelling potentially allows for determination of signal frequencies and selection of features for extraction without the need for a full scale prototype structure with realistic defects and damages.

1.2 Research Objective

To investigate the functionality of active acoustic SHM using a pitch-catch setup for the detection of BVID in the DragonFly fuselage, a research project was conducted that may be characterized as both theoretical and practical (Verschuren 2010). The aim of this research project was to overcome some of the challenges in active acoustic SHM for the structure of interest. In the specific case of sandwich composite structures, two subjects were of particular interest: the classification of guided wave propagation modes and the influence on guided wave propagation of actual impact damage as opposed to simulated damage.

To increase the level of understanding on these two subjects, acoustic wave propagation in sandwich composite structures and, more in particular, the DragonFly fuselage structure needed further research. This was essential to the selection of the proper frequency. Furthermore, a good understanding of the impact response of the structure was required to define the damage modes that were to be detected. To this end, BVID was defined as impact damage that cannot be seen with the naked eye, where the visibility threshold was defined in terms of residual indentation at the impact location (see section 2.2.1). These two topics combined would allow for prediction of the response to impact damage and selection of the features to be extracted from the received signal. Verification through experiments and FE modelling was conducted to confirm these findings.

The division between theoretical and practical can be applied along the line of research components. A literature study was conducted, which encompassed the theory-oriented part and was to result in:

1. a theoretical model for the propagation of acoustic waves in sandwich composite structures;
2. an overview of the state of art on active acoustic SHM systems with a pitch-catch setup for the detection of impact damage in sandwich composites;
3. a model for the simulation of impact damage in the given structure;
4. data analysis model (feature discrimination) for the response to impact damage in the DragonFly fuselage structure.

The practical part of the research was to result in:

1. verification of the data analysis model (feature discrimination);
2. a verified theoretical model of a flat sandwich composite panel with SHM system;
3. SHM system capable of detecting BVID.

To arrive at the deliverables listed above, the research questions were formulated as follows:

1. *How can BVID in a lightweight sandwich composite structure be characterized and how can this characterization be translated to FEM simulations?*

2. *How do acoustic waves propagate through a lightweight sandwich composite structure and how is this propagation affected by BVID?*

3. *Can we develop a digital twin formulation of this type of structure with active acoustic SHM system that allows us to predict the effect of BVID on selected features of the through-transmitted acoustic signal?*

1.3 Report Setup

The theory oriented part of this study is divided into two sections. First, the Operational Evaluation provided in section 2 gives a short analysis of the DragonFly fuselage from a structural perspective and a theoretical analysis of impact damage in the sandwich composite fuselage structure. Second, an introduction on Guided Waves and literature reviews on the use of Guided Waves in the detection of impact damage in sandwich composite structures is demonstrated in section 3. These two theoretical parts served as input for the practical part of this research.

The practical part is again divided in two sections: experiments and modelling. The experimental setup and results are treated in section 4. Experiments were required for three purposes: (i) the determination and verification of mechanical properties used in the theoretical model; (ii) investigation of the structure's response to impacts; and (iii) verification of the model for the response to acoustic signals. The production of test coupons also served as production experiments for production of the fuselage structure. Mechanical tests were conducted according to ASTM standards where applicable (for example D7136 (ASTM 2005) for measuring impact damage resistance).

The specifics of the modelling technique and the results of simulations are provided in section 5. The digital twin formulation and simulations were run in Abaqus CAE®. The model was created such that simulation results could be compared to experimental results, which provided a basis for the evaluation of the model accuracy.

Finally, answers to the research questions and an evaluation of the research are discussed in section 6. In this section, some recommendations for future research are also included.

2 Operational Evaluation

In this chapter, the structural considerations relevant to SHM are considered. This information serves as input for sections 3, 4 and 5. First, the initial structural design is briefly presented, including deviations from this design within the current study. Then, a short theoretical review on impact damage is presented, followed by a definition of the damage to be considered by the SHM system.

2.1 Structural Design

The structural design of the DragonFly is treated extensively in Martinez (2013). As shown in Figure 2 and Table 1, the largest portion of the DragonFly fuselage is to be produced from a GFRP/foam sandwich construction. The materials selected by the designers are E-glass/Epoxy composite skins and a Polymethacrylimide (PMI) foam core. Since the material properties vary depending on for example brand and production process and parameters, typical material properties were used by Martinez (2013) (see Table 2).

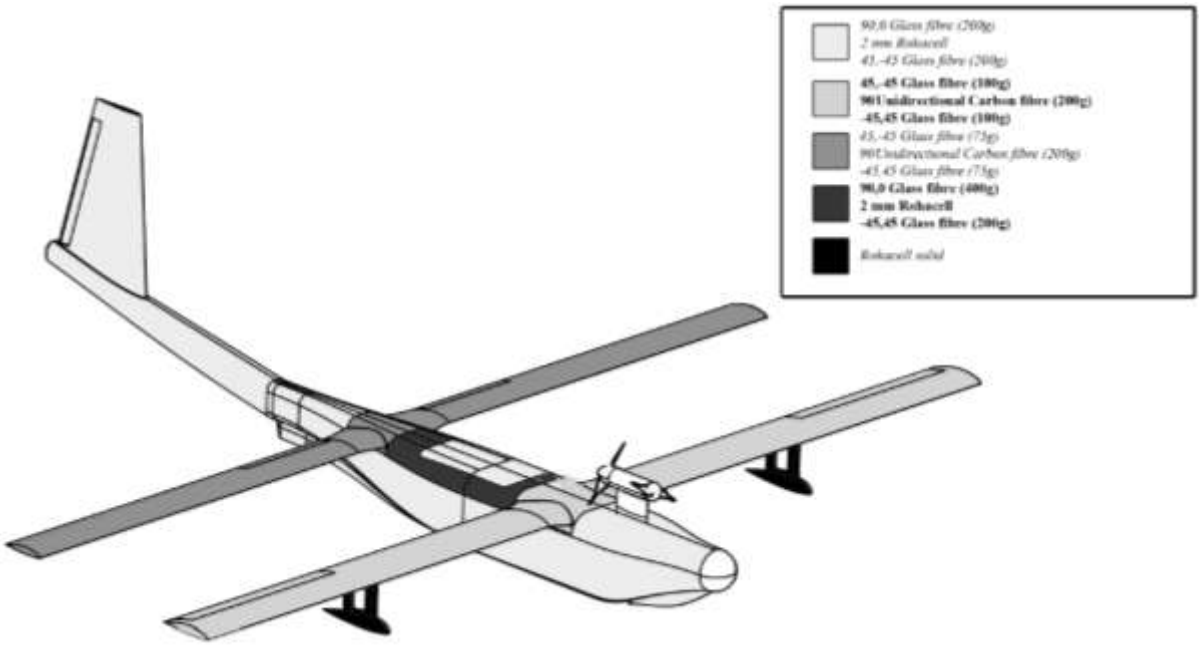

Figure 2 | Laminate build-up of structural members (Martinez 2013).

Additional reinforcement is created around the access panel by doubling the amount of GFRP on the outer skin (the dark grey shaded section of the fuselage between the wings in Figure 2). Also, it should be noted that the sandwich structure is asymmetrical and unbalanced, since the outer skin is constructed with 0-90 degree glass fibre/epoxy laminate and the inner skin with ±45 degree. The zero degree direction is, however, not indicated by Martinez (2013), which means that the actual orientation of the fibres relative to the body axes is not defined.

The production process selected by Martinez (2013) for the fuselage is vacuum infusion. The outer skin is selected as the tool side (see Figure 3) to ensure a smooth surface finish. As can be seen in Table 2, a high density Rohacell A foam is used for the core (Rohacell 110A, see datasheet in Appendix I). Still, compared to the skins, the density of the core is extremely low. This makes

the sandwich construction significantly different from monolithic laminates when ultrasonic wave propagation is considered, since the density of the medium has a large effect on the behaviour of ultrasonic waves. This is further investigated in section 3.

Table 1 | Material usage map (Martinez 2013).

Part	Material(s) used
Wing	E-glass FC; HM carbon FC; PMI foam
Floater & floater-wing connection	E-glass FC; PMI foam
Hull	E-glass FC; PMI foam
Tail boom	E-glass FC; PMI foam
Vertical tail plane	E-glass FC; PMI foam
Motor mount	E-glass FC; PMI foam; Al 2024-T3
Propeller	TBD
Camera dome	Polycarbonate
Structural connections	Stainless steel; Al2024-T3

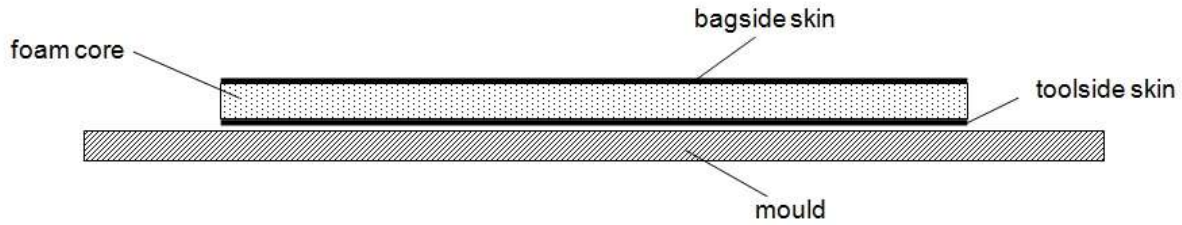

Figure 3 | Sandwich constituent definition.

Table 2 | Material characteristics. All composite fibres are UD in epoxy resin with 60% fibre content, cured at 120°C (Martinez 2013).

Material name	Density [g/cc]	Modulus [GPa]	Tens. strength [MPa]	Compr. strength [MPa]	Ult. tens. strain [%]	Ult. compr. strain [%]
E-glass composite	1.90					
- longitudinal		40	1000	600	2.50	1.50
- transverse		8	30	110	0.35	1.35
High-modulus CF composite	1.60					
- longitudinal		175	1000	850	0.55	0.45
- transverse		8	40	200	0.50	2.50
Rohacell® 110A PMI foam	0.110	0.160	3.50	3.00	4.5	-
Al 2024-T3	2.77	69	345	-	18	-
Stainless steel 405	7.8	200	170 (yield)	-	20	-
Polycarbonate	1.2	2.38	62.1 (yield)	-	6 (yield)	-

2.1.1 DEVIATIONS

In the current study some deviations are introduced to the structural design described above, as summarized in Table 3.

The mechanical properties used by Martinez (2013) and reproduced here in Table 2 suggest a cure at 120 ˚C. In the current study, it was decided to use room temperature curing to simplify test coupon production. As this production parameter is used consistently, it shall not influence the results of the current study.

A further simplification was the use of 200 g/m^2 E-glass weaves for the GFRP skins, instead of a cross-ply of 100 g/m^2 UD. In fact, a dry glass fibre UD of such a low weight per unit area may be very hard to find. More importantly, serious complications may be encountered during production of the hull through vacuum infusion when handling such a fabric. To approximate the UD lay-up a HexForce 2/2 twill weave with a 50/50 fibre weight distribution between the 0˚ and 90˚ directions is selected (see the data sheet in Appendix I). Three examples of commonly available weaves are given in Figure 4. Generally, fabrics with less interlacing (such as the satin weave) have better drapability and improved strength and stiffness, but are less resistant to in-plane shear and distort more easily during handling. The 2/2 twill weave is chosen as a trade-off between higher strength and stiffness and ease of handling during production.

Contrary to the initial design, a balanced and symmetrical laminate build-up was used. This means that the skins have the same fibre orientation and are mirrored with respect to the centre plane of the sandwich construction. This was expected to simplify the analysis of wave propagation. The skins are thus produced with one single ply of fabric.

Table 3 | Structural design deviations.

Design parameter	Deviation
Cure temperature	Room temperature
Glass fibre reinforcement	HexForce 2/2 twill weave 200 g/m^2
Skin laminate	Single ply [0/90˚]
Laminate lay-up	Balanced and symmetrical

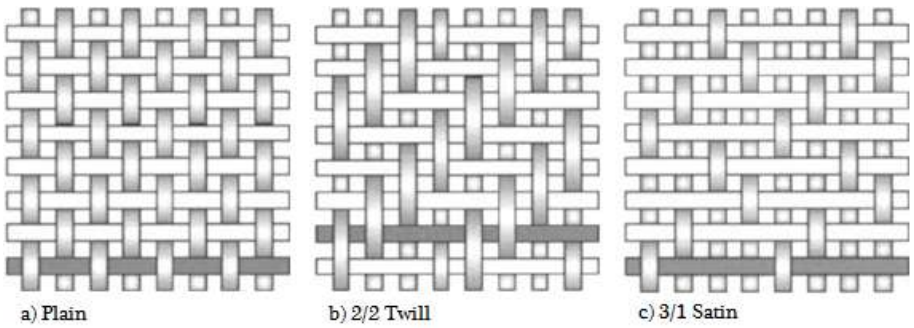

Figure 4 | Weave styles (Campbell 2004).

2.2 Damage Definition

A useful definition of damage was given by Worden, Farrar et al. (2007): *'Damage* is when the structure is no longer operating in its ideal condition, but it can still function satisfactorily, but in suboptimal manner.' In a hierarchical order Worden, Farrar et al. (2007) placed damage before *fault*, when the structure can no longer operate satisfactorily, and after *defect*, which is an imperfection inherent to the material or the production of the structure.

The current study deals with the detection of BVID in a sandwich composite structure. Therefore, this paragraph is focused on the definition and quantification of BVID in such structures specifically. The aim is to determine from which point an impact should be considered a damage event and which measure can be used to quantify that point. Furthermore, the aim is to determine in which range of impact damage severity an SHM system should operate to achieve maximum effectiveness within the limits of technical possibilities. The different damage modes connected to impact damage in sandwich composites are described first, followed by a paragraph on damage tolerance where the point from which an impact should be considered a damage event is further specified. Then, the specific case of the DragonFly fuselage structure is further defined in terms of impact resistance and damage tolerance. In the final paragraph the boundaries for damage detection through SHM are set.

It should be noted that the analysis in this section is predominantly qualitative. Analytical models and quantitative studies of impact behaviour and damage are considered to be outside the scope of the current study.

2.2.1 Impact Damage in Sandwich Composites

Due to the detrimental effect of BVID on the residual strength and fatigue life of sandwich composites the subject has received attention in many studies (Tomblin, Raju et al. (2001); Edgren, Asp et al. (2004); Shipsha and Zenkert (2003); Freeman, Schwingler et al. (2005)). A majority of researchers have focused on the influence of impact conditions (e.g. energy, impactor geometry) and specimen properties (e.g. density and flexural rigidity of the core, layup and relative thickness of skins) on the impact response of the structure and constituent materials (e.g. impact force history, damage size and residual indentation) (Caprino and Teti (1994); Anderson and Madenci (2000); Daniel, Abot et al. (2012)). Such studies provide a good overview of possible damage modes.

A simple approach to analyze the impact response of a structure is the energy balance model (Abrate 2001). Under the assumption that the structure behaves quasi-statically, the kinetic energy of an impactor has been completely used to deform the structure when it reaches maximum deflection. The energy balance equation can then be formulated as:

$$\tfrac{1}{2} m v^2 = E_b + E_s + E_m + E_c \qquad (2.1)$$

Where m and v are the impactor mass and velocity respectively, E stands for energy and the subscripts b, s, m and c refer to bending, shear, membrane stretching and contact effects respectively. As can be seen from the experimental results obtained by Hazizan and Cantwell

(2002), membrane stretching is negligible when the impact energy is sufficiently low compared to the structure's stiffness. The energy balance model also offers some insight into the possible failure modes of sandwich composites due to impact.

Neglecting membrane stretching, three sources for damage based on the energy balance model can be distinguished: bending, shear and contact effects. Since those sources occur simultaneously, the corresponding failure modes will occur simultaneously as well. However, the way in which impact energy is absorbed by a sandwich panel is highly dependent on the geometry and material properties of both the panel and the impactor, in addition to the impact energy and boundary conditions (i.e. support of the specimen).

In general, damage immediately after impact can be categorized as follows (list compiled from Caprino and Teti (1994), Daniel, Abot et al. (2012) and Edgren, Asp et al. (2004):

1. Matrix cracking
2. Core compression
3. Delamination in the skin
4. Skin/core de-bonding
5. Fibre breaking
6. Skin indentation
7. Core crushing
8. Core shear failure
9. Skin penetration

These damage modes can occur simultaneously. Roughly speaking, the damage modes as listed here can be associated with increasing impact energy. In a coated sandwich panel where internal damage is not visible, the modes numbered 1-4 may fall into the non-visible impact damage range, whereas 5-7 could fall in the BVID range.

Useful graphical illustrations of non-visible and barely visible impact damage were given by Shipsha, Hallstrom et al. (2003) and Lacy and Hwang (2003) and reproduced here in Figure 5. These figures schematically show the failure modes numbered 2-7 (excluding fibre breaking). Also, the distinction between foam and honeycomb core is made here. It can be seen from Figure 5 (a) that in a foam core sandwich de-bonding can occur between skin and core, where the separation actually occurs in the core at a small distance from the skin (Shipsha, Hallstrom et al. 2003). This illustrates that impact damage can be quite severe without leaving visible indentation of the skin.

In experimental studies it was shown that residual indentation does occur in foam core sandwich constructions (Anderson and Madenci 2000). Residual indentation is indicated in Figure 5 (b). The two figures combined give the characteristic dimensions that were used to quantify impact damage in the current study.

Considering the above, it is not possible to relate BVID to a range of impact energies. Rather, BVID can only be defined by visual standards and the related impact energies and velocities have to be determined for each individual structure and impactor. In this study, impact damage was

considered to be barely visible when the residual indentation (indicated in Figure 5 (b) as δ_I) is 0.5 mm or less (0.2" after Tomblin, Raju et al. (2001)). As was shown experimentally by Tomblin, Raju et al. (2001), the planar damage area can be orders of magnitude larger than the residual indentation, depending largely on impact energy and the size of the impactor. For example, they found planar damage areas with diameter up to ~110 mm in sandwich panels with a ~10 mm honeycomb core impacted with a 3" (76.2mm) diameter spherical impactor, while the residual indentation was well below the 0.5 mm visibility threshold.

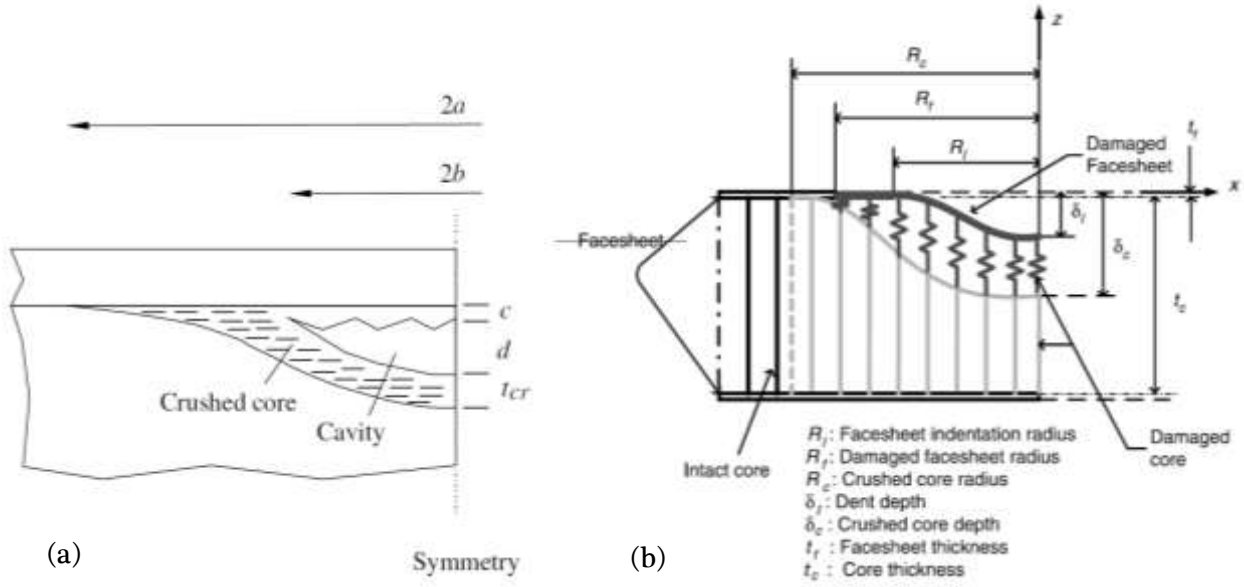

Figure 5 | Impact-damaged region in (a) foam core sandwich without skin indentation (Shipsha, Hallstrom et al. 2003) and (b) honeycomb core sandwich with skin indentation (Lacy and Hwang 2003).

2.2.2 IMPACT DAMAGE TOLERANCE

For the current study we are interested in determining at which point BVID leads to a decrease of strength or fatigue life of such an extent that it must be considered a damage event. This point can be expressed in terms of damage size. To that end, the mechanical properties after impact can be defined in several ways. Three frequently used measures are Tensile strength After Impact (TAI), Compressive strength After Impact (CAI) and Fatigue life After Impact (FAI).

Tensile Strength After Impact (TAI)

Since the number of possible combinations of constituent materials, specimen dimensions and experimental parameters are limitless, an analytical model that predicts the residual properties after impact could be extremely complex. An elegant and simple model that relates the impact energy to the residual tensile strength for a given material was presented by Caprino and Teti (1994). They compared the tensile strength of notched laminate specimen to the residual tensile strength of sandwich skins that were separated from the core after impact. They concluded that the TAI of the skin could be accurately predicted by comparing the zone of damaged fibres to a circular through-thickness hole of the same size. Based on this comparison they developed the following relation:

$$\frac{\sigma_c}{\sigma_0} = \left(\frac{U_0}{U}\right)^m \qquad (2.2)$$

In which:
σ_c – residual tensile strength
σ_0 – tensile strength of the pristine material
U – impact energy
U_0 – limit impact energy
m – constant, accounting for the intensity of the stress field around the damage

Where U_0 and m are determined experimentally. This relation holds when the damage size is linearly proportional to the impact energy, an assumption that Caprino and Teti (1994) confirmed with experimental results. Also, the relation holds in the range $U_0 \leq U \leq U_p$, where U_p is the skin penetration energy. Beyond penetration energy, damage size is expected to be constant and thus no further reduction of TAI is to be expected. Furthermore, equation (2.2) suggests that a limit of the impact energy exists, below which the TAI is equal to the original tensile strength. The existence of this limit was experimentally confirmed by Caprino and Teti (1994) and shown to correspond to the impact energy that marks the transition from matrix cracking to fibre breaking as damage mode in the impacted skin.

Figure 6 shows the results of tensile tests conducted by Caprino and Teti (1994) on the 1.3 mm thick GFRP skins of sandwich specimen with different 15 to 25 mm thick PVC foam core types, impacted at energies ranging from 2 to 20 J. This graph shows that the TAI reduced dramatically with increasing damage size D, where damage was defined as the zone containing broken fibres.

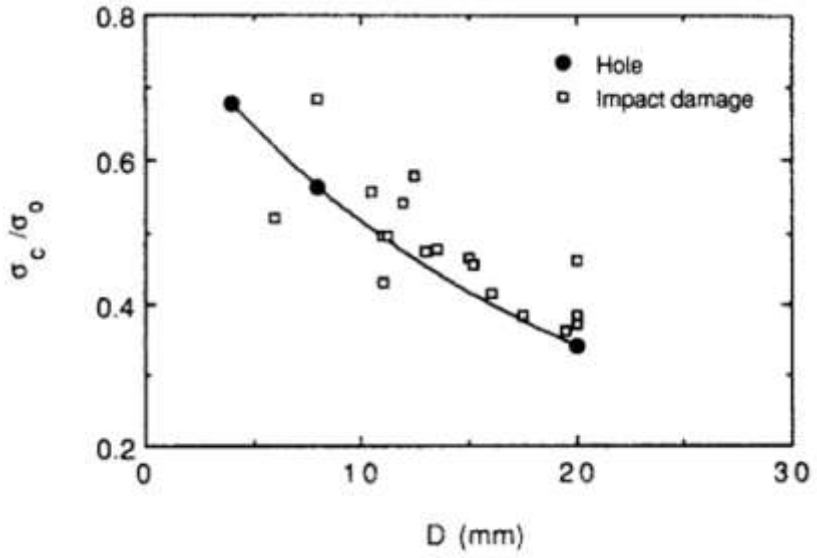

Figure 6 | Non-dimensional residual tensile strength of facing material, σ_c/σ_0, against damage diameter D. D represents the zone containing broken fibres. (Caprino and Teti 1994).

Although the TAI values found by Caprino and Teti (1994) were not corrected for the specimen finite width, Figure 6 shows that small damage sizes can have a detrimental effect on the TAI.

However, this is only the case if fibre breaking occurs and this only happens above the limit impact energy.

Compressive Strength After Impact (CAI)

A frequently used standard for determining the CAI of FRP panels is ASTM D7137 (ASTM 2012). This standard applies to laminate plates and gives a measure for ultimate compressive residual strength and effective compressive modulus after impact. Application of this standard to sandwich composites was not encountered, but CAI was applied as a measure of residual properties of sandwich composites by Tomblin, Raju et al. (2001); Edgren, Asp et al. (2004) and Daniel, Abot et al. (2012) among others.

Edgren, Asp et al. (2004) studied the failure mechanisms in sandwich composite panels when subjected to in plane compressive loading after impact. Both visible and barely visible impact damage were studied. Impact damage observed in the skins consisted of matrix cracks, delaminations in the skin, fibre breaking and residual indentation. It was concluded by Edgren, Asp et al. (2004) that the dependence of CAI on impact energy was very small, because the strains at failure did not differ much between panels subjected to different impact energies. Also, the compression stiffness of the skins appeared to be largely unaffected by impact damage. Damage initiation in the form of kink bands was observed at 50-70% of the failure load. This was attributed to stress concentrations and local bending. According to the authors, local bending originated from residual indentation and local material asymmetry of the skin caused by delaminations, whereas stress concentrations were caused by matrix cracks, fibre breaking and delaminations.

An explicit comparison of compressive failure load between damaged and pristine sandwich panels was not made by Edgren, Asp et al. (2004). In an earlier study, Tomblin, Raju et al. (2001) made this comparison for sandwich panels of 267 x 216 mm with honeycomb core and CFRP skins of different thicknesses. They reported a decrease of CAI of tested panels down to 40%. A selection of their results from the lowest impact energy range is reproduced in Figure 7. The damage dimension in this figure was calculated from the damage area measured from C-scan images as reported by Tomblin, Raju et al. (2001), assuming a circular shape.

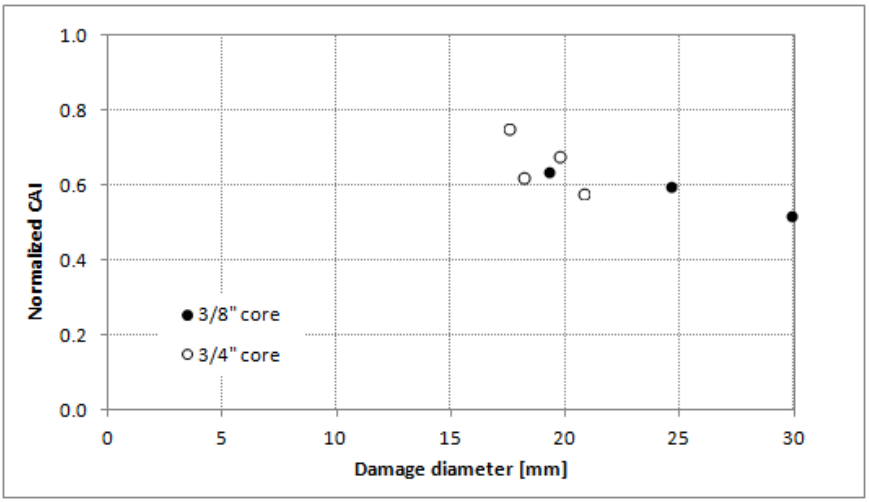

Figure 7 | Compression after impact strength values as a function of planar damage area for [(90/45)/CORE/(45/90)] panels. Data adapted from Tomblin, Raju et al. (2001).

A compressive strength reduction to 40% was also found experimentally by Daniel, Abot et al. (2012). In their study, a rectangular coupon was sectioned from an impacted sandwich panel and loaded in compression at the ends. After impact the specimen showed delamination damage and residual indentation of 0.9 mm. Failure of the specimen occurred at the impacted skin, where delamination from impact resulted in kink band formation and final failure. Comparison to a pristine specimen showed a reduction of compressive strength by 60%.

Fatigue Life After Impact (FAI)

Of the large body of scientific research on fatigue life after impact of fibre reinforced plastics, only a very small portion concerns the specific case of sandwich composites. A study to the four point bending fatigue response of sandwich composite beams with non-visible impact damage was conducted by Shipsha and Zenkert (2003). In their experiments, cylindrical rather than spherical impactors were used, resulting in two dimensional impact damage across the width of the beams, consisting of crushed core and debonding. The failure process under cyclic four point bending was characterized by the authors with three steps: crack growth at the interface between the top skin and the core in the crushed core zone (see Figure 5 a)); crack initiation at the interface between crushed and undamaged core; crack propagation into the core towards the opposite skin. It was found by Shipsha and Zenkert (2003) that the fatigue life of impacted beams was mainly dependent on the maximum cyclic load, and hardly on the load ratio (the ratio between minimum and maximum load). This can be seen in Figure 8, which also gives an impression of the potentially detrimental effect of impact damage on the fatigue life.

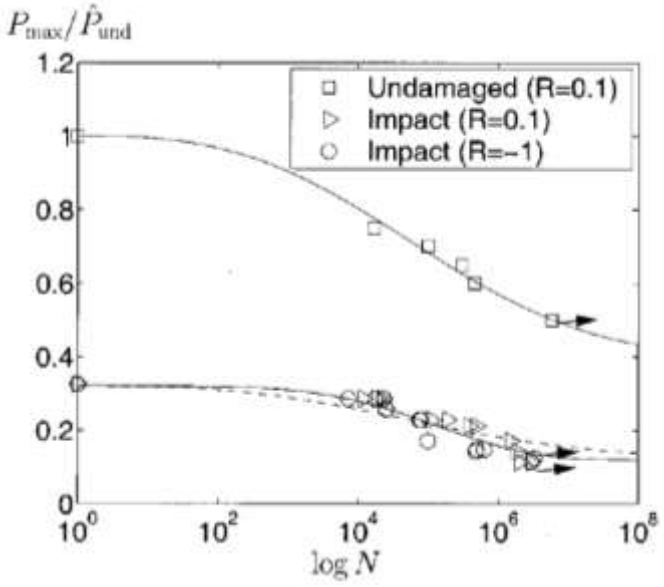

Figure 8 | S-N diagram for undamaged and impact-damaged specimens tested at R=0.1 and -1 (Shipsha and Zenkert 2003). Solid arrows indicate that the corresponding specimen did not fail within the scope of the fatigue test.

The strength of the tested beams was characterized in static four point bending tests by Shipsha and Zenkert (2003) in terms of the bending load at failure. The static strength of impacted specimen was reduced to 55% compared to undamaged specimen, whereas the static strength after

the first step in the failure process was reduced to 32%. This first step was shown to proceed over roughly 20,000 cycles. Furthermore, it was found by Shipsha and Zenkert (2003) that the fatigue threshold was around 35% of the static strength after the first failure step. Simple calculation learns that the fatigue threshold was thus 11% of the static strength of the undamaged specimens.

Contrary to the findings of Shipsha and Zenkert (2003), the four point bending fatigue experiments conducted by Freeman, Schwingler et al. (2005) on sandwich composite beams showed that impact damage does not necessarily result in a reduction of fatigue life. Impacted samples with a foam core of 106 kg/m^3 failed at the support of the bending fixture, the same location as undamaged specimens. Specimens with a higher density core (164 kg/m^3), however, did fail at the impact location. This change of failure mode effectively increased the fatigue life of the impacted specimens compared to undamaged specimens.

A possible explanation for these apparently contradicting findings may be found in two differences in the cited experiments. First, Freeman, Schwingler et al. (2005) used a spherical impactor of 12.7 mm on beams of 304.8 x 76.2 mm and used a clamping fixture for the impact setup, whereas Shipsha and Zenkert (2003) mounted the specimens on a rigid plate support and used a cylindrical impactor as described before. This results in different impact damage modes, among others because in the latter case impact energy cannot be converted into bending of the beam and membrane stretching.

Second, Shipsha and Zenkert (2003) used a low density Rohacell WF51 core with GFRP skins, while Freeman, Schwingler et al. (2005) produced their samples from high density polyurethane cores and CFRP facings. This, again, gives different damage modes and sizes. Another complicating factor when attempting to determine the FAI is that four-point bending is only one type of cyclic loading that can result in fatigue damage and failure. As noted by Edgren, Asp et al. (2004), for example, the fact that damage growth occurred in their experiments at load levels of 50-70% of the failure load indicates that impact damage could have a large influence on compression fatigue.

Considering the above, it is currently not possible to relate a damage size to the fatigue tolerance of the DragonFly fuselage structure. It was shown, however, that impact damage could grow under the influence of fatigue loading and thus initiate failure due to fatigue.

From the references presented here it is apparent that impact damage can have a large influence on the ability of a sandwich composite to perform its function. Especially the finding of Shipsha and Zenkert (2003) that as a result of BVID the fatigue threshold could reduce to 11% of the undamaged static strength after roughly 20,000 loading cycles indicates that early detection of impact damage of small sizes is vital to the structure's performance.

If we are to determine at which point BVID leads to a reduction of strength or fatigue life of such an extent that detection through SHM is required, we may be tempted to say that such a system should be able to detect even the smallest damage. We should keep in mind, however, that an active SHM system can be designed to detect damage within a safe range of fatigue cycles in order to allow for some damage growth to take place before detection occurs. Based on the results of static TAI and CAI experiment that were reproduced in Figure 6 and Figure 7, a minimum detectable damage diameter of 10mm was considered reasonable for an active acoustic SHM

system in the DragonFly fuselage. In other words, an impact resulting in 10mm diameter damage was identified as the minimum damage event to be detected.

2.2.3 Impact Resistance of the Structure Concerned

In the previous paragraph, the minimum detectable damage size was determined in terms of a damage diameter of 10mm. To quantify the ability of a structure to resist impact, however, impact energy is a more useful measure. Also, an impact energy range was required for impact experiments. To determine this, a qualitative estimation of the relation between impact energy and damage size was made from literature research.

Despite the vast amount of research done in the field of impact damage in composite structures, few publications were found that treated structures comparable to the DragonFly fuselage structure. Three sources are presented here and used to come to a rough estimate of the impact resistance of the fuselage structure.

Caprino and Teti (1994) studied the impact response of sandwich panels with GFRP skins and PVC foam cores. The 1.3 mm thick skins were produced from a plane weave prepreg with layup $(0\text{-}90/\pm45)_S$ and three different core densities were used (49, 55 and 130 kg/m^3) with thickness 20mm. The panels were clamped in a circular support of 60mm diameter and impacted at energy levels ranging from 2 to 20 J with a 20 mm diameter, 1 kg hemispherical tup. Following impact, a damage parameter was chosen as the maximum width of the zone in the impacted skin containing broken fibres. Measurements of this parameter, as reported for the back surface of the impacted skin, are reproduced in Figure 9 for comparison.

In an experimental investigation facilitating the modelling of impact damage, Shipsha, Hallstrom et al. (2003) impacted sandwich composite beams with a cylindrical impactor. The beams were manufactured with a 50 mm thick Rohacell WF51 PMI foam core of density 52 kg/m^3. The skins were produced from a quasi-isotropic E-glass/Vinylester laminate with thickness 2.4 mm. A cylindrical impactor with diameter 25 mm and length 60 mm and total mass 7.73 kg was used at impact energies 6.6, 13.3, 20.0, 26.5 and 40 J. The diameter of skin-core delamination area was reported as a damage parameter and is reproduced here in Figure 9 after truncating at 20 J and averaging the reported damage ranges.

Ugale, Singh et al. (2013) studied thin sandwich panels under impact, three point bending and transverse central loading. The thickness of their specimens was close to 3 mm with skins made of GFRP using a 360 g/m^2 plain weave reinforcement and three types of core material: polyester foams Coremat XM and Coremat Xi and a core that consisted of two layers of jute fabric. These core materials are impregnable, which greatly improved the tensile modulus of the core (1.10 GPa for epoxy impregnated Coremat Xi and 1.00 GPa for epoxy impregnated Coremat XM). Thus, the sandwich composites tested by Ugale, Singh et al. (2013) are not fully comparable to the structure of the DragonFly fuselage. The specimens were clamped in a square support with dimensions 150x150mm and impacted with a 30mm diameter, 1.084kg hemispherical impactor at energy levels ranging from 6 to 24 J. A damage parameter was identified by holding the impacted panels against a strong light and measuring the size of delamination. The average area of this zone was

reported for impact energies 6, 12 and 18 J. This data is reproduced here in Figure 9 after calculating the damage diameter from the reported surface area (approximated to be circular).

Although the input parameters for the experiments of Ugale, Singh et al. (2013), Shipsha, Hallstrom et al. (2003) and Caprino and Teti (1994) are very different, their combined results as presented in Figure 9 show a trend that suggests a comparable relation between impact energy and damage size. However, damage size in this figure corresponds to different damage parameters as defined in the respective studies. Further verification of this trend is not available at this time, because most studies on impact damage in sandwich composites do not report a comparable quantity for damage size.

Two impacts (see section 4.3) from a series of four impacts made on the sandwich structure under investigation are included in Figure 9 (specimen 20150313SW1). The impact energy was selected to fall in the middle of the range of 0 to 20J, and the results give some confirmation that the impact resistance of the specimen can indeed be compared to that of the specimens from cited literature. Figure 9 provides some insight into the impact energies required to induce impact damage in sandwich composites. It was estimated from this figure that impact energies should be as low as possible to create damage with a characteristic diameter of 10mm and above.

It is worth noting that BVID was defined in section 2.2.1 in terms of residual indentation, while for SHM considerations impact damage was quantified by in plane damage size. A complication is that the relation between those parameters is dependent on impactor geometry and mechanical properties and thickness of the skin and core (Tomblin, Raju et al. 2001). As a result, whether the determined damage size threshold of 10mm diameter fell in the visible, barely visible or non-visible range could not be determined theoretically. For this reason, residual dent depth was measured for all impact experiments to verify that the damage was indeed barely visible.

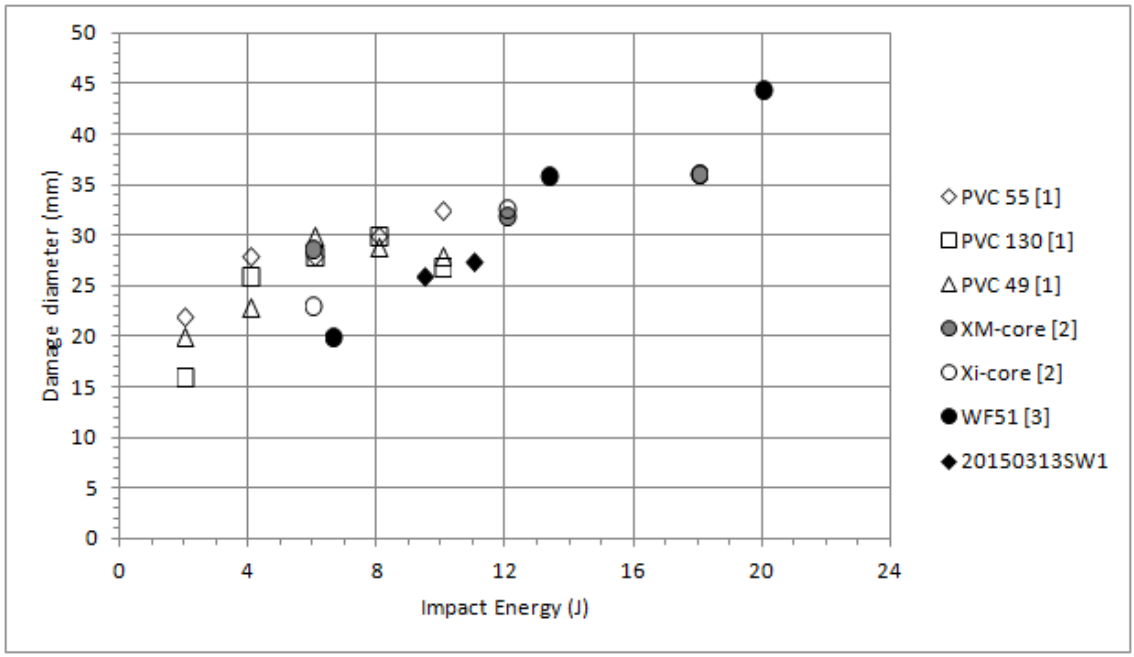

Figure 9 | Damage in sandwich composite plates after impact. Data taken from [1] Caprino and Teti (1994), [2] Ugale, Singh et al. (2013) and [3] Shipsha, Hallstrom et al. (2003) (data from the latter source has been truncated and averaged).

3 Guided Waves

This section deals with the fundamentals of acoustic wave propagation in plate-like media, more in particular in sandwich constructions. Some general characteristics of guided waves are introduced in section 3.1, followed by the more specific case of wave propagation in sandwich panels in section 3.2. A distinction is made here between different modes of propagation in sandwich-like media. Finally, this distinction is used to give an ordered overview of the current state of art on active acoustic SHM in sandwich composites with a pitch-catch setup. This section is concluded with the relevant considerations for mode selection in the structure of interest.

3.1 Guided Wave Characteristics

The body of publications on the analysis of guided waves is vast and dates back to the work of Lord Rayleigh from 1885 (Rayleigh 1885) on the propagation of elastic waves on the free surface of a semi-infinite solid. Since then, the shear horizontal (SH) and Lamb wave types, both guided plate waves, have been identified by Love (1911) and Lamb (1917) respectively. Many studies are available on the properties of guided waves and their propagation through solids. In the current study, the work of Giurgiutiu (2008) is discussed.

Rayleigh waves, also known as surface acoustic waves or surface-guided waves, propagate close to the body surface and have little effective penetration into the depth (less than a wavelength). They are found in solids with at least one free surface. The particle motion is circular, in the plane made up by the normal to the surface and the parallel to the propagation direction (see Figure 10).

Figure 10 | Simulation of Rayleigh wave in a semi-infinite medium (Giurgiutiu 2008).

The motion of SH waves is contained in the horizontal surface and takes place only in the direction perpendicular to the propagation direction. In a half space, SH waves are surface guided and called Love waves, which have a limited penetration depth. In a sufficiently thin plate with two parallel free surfaces, SH waves occur through the thickness as guided plate waves. Both symmetric and anti-symmetric modes can be distinguished, referring to the distribution of particle motion direction through the thickness. Figure 11 shows the first three symmetric and anti-symmetric modes, where the wave propagates along the x-axis and the particle motion is along the z-axis. Which modes appear depends on the properties of the medium as well as the frequency of the wave.

Lamb waves are characterized by a particle motion similar to that of Rayleigh waves, but contrary to Rayleigh waves, Lamb waves are guided plate waves, and hence penetrate through the full thickness of the medium. As a result, symmetric and anti-symmetric modes can be distinguished. The first (a.k.a. fundamental) symmetric (S_0) and anti-symmetric (A_0) modes are depicted in Figure 12. The existence of higher order lamb modes depends on the medium properties and thickness as well as the frequency of the wave. In a plate-like medium of finite thickness, then, we may theoretically find an infinite number of symmetric and anti-symmetric Lamb wave modes, as well as an infinite number of symmetric and anti-symmetric SH wave modes. For the purpose of SHM, however, the application is often limited to the fundamental modes to avoid high complexity of signal analysis. Displacement profiles for the fundamental symmetric and asymmetric modes at different frequencies are given in Figure 13 and Figure 14.

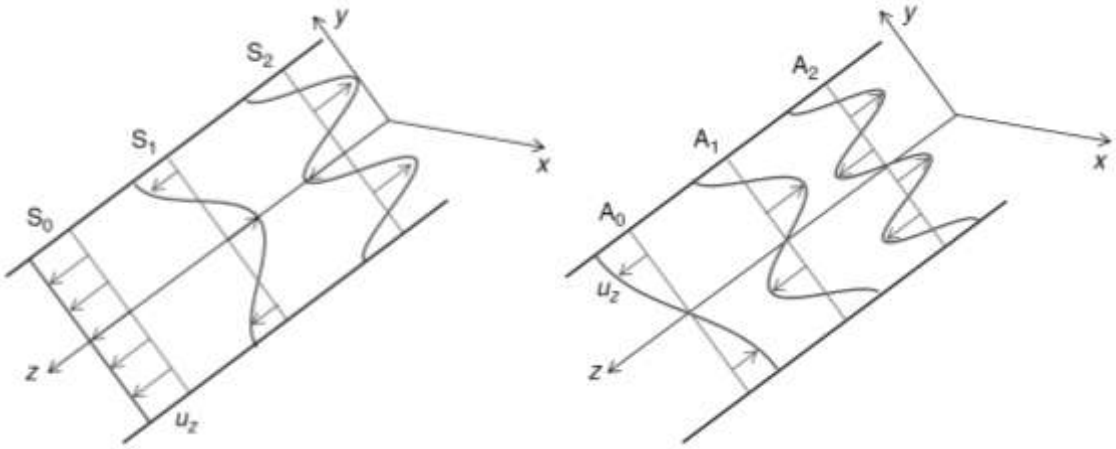

Figure 11 | Plot of the first, second and third symmetric (left) and anti-symmetric (right) modes of the SH waves (Giurgiutiu 2008).

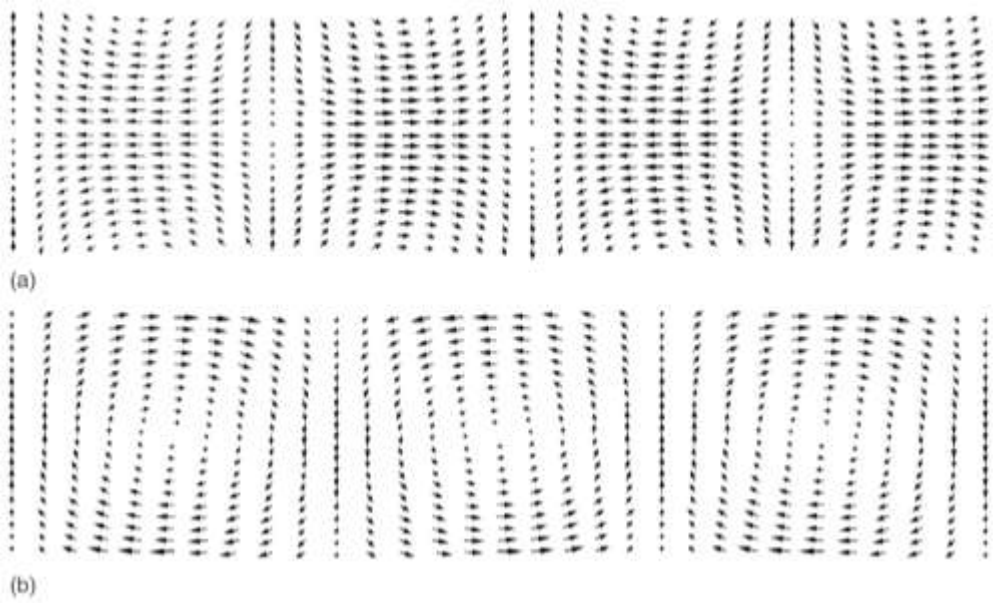

Figure 12 | Simulation of Lamb waves: (a) symmetric S_0 mode; (b) anti-symmetric A_0 mode (Giurgiutiu 2008).

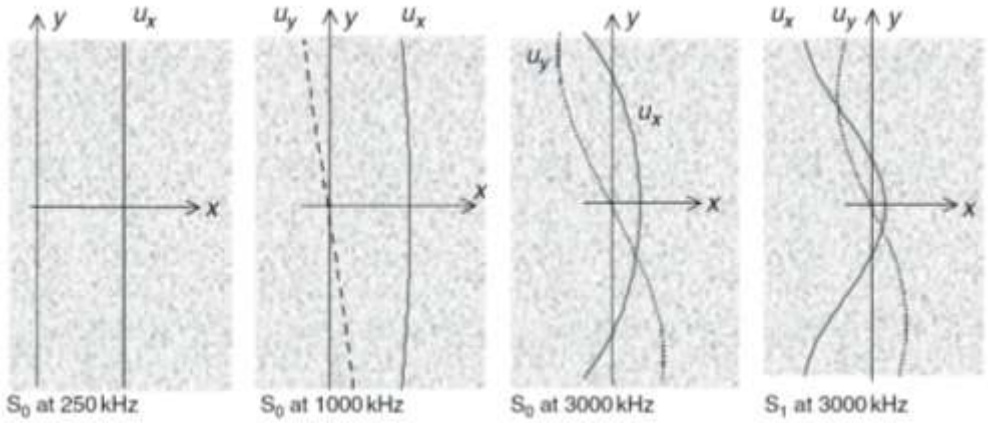

Figure 13 | Across the thickness displacement fields in a 1 mm thick aluminium plate for various symmetric Lamb modes at various frequencies (Giurgiutiu 2008).

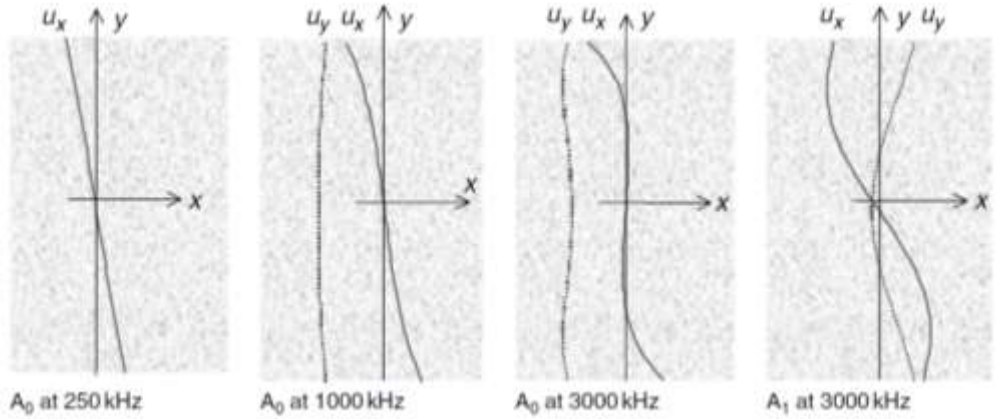

Figure 14 | Displacement fields across the thickness for various anti-symmetric Lamb modes at various frequencies in an aluminium plate (Giurgiutiu 2008).

In order to generate a wave packet in an active SHM approach, the amplitude of a single frequency carrier wave is modulated to generate a transient tone burst. In the literature on active SHM of sandwich composites, the most common window function for modulation is the Hanning window (Bourasseau, Moulin et al. (2000), Diamanti, Soutis et al. (2005)). This type of tone burst generates a narrow frequency band that, although having one central frequency ω_c, consists of a multitude of frequencies centred around ω_c as a result of the windowing operation. This means that if the wave speed depends on the frequency of the wave, the shape of the tone burst will change in time as it propagates through the medium. This phenomenon is called dispersion, and is more severe for narrow windows than it is for broad windows. In other words, an inverse relation exists between the time duration of the tone burst and its frequency spread.

The dispersive characteristics of a medium can be summarized in dispersion curves, showing the relation between the frequency-thickness product and the phase velocity, group velocity or wave number. Phase velocity dispersion curves for Lamb waves propagating in 0° direction of the GFRP skin are given in Figure 15. These curves were calculated using the Matlab code developed by Pant, Laliberte et al. (2014) and material properties as determined in section 4.1. Dispersion curves are of great importance to the mode selection, providing information on the occurrence of

both symmetric and anti-symmetric modes, as well as the degree of dispersion of those modes for any given frequency and/or plate thickness.

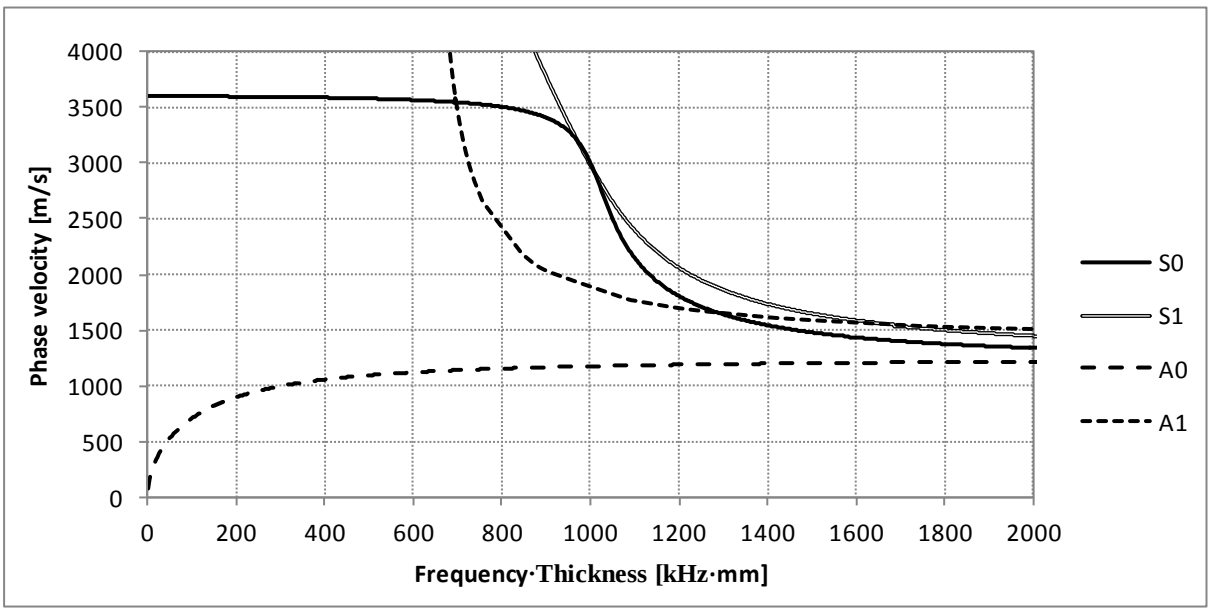

Figure 15 | Lamb wave phase velocity dispersion curves as function of frequency-thickness (*fh*) product for the 0° direction of the GFRP laminate.

Since a tone burst contains a range of frequencies, it is important to distinguish between group velocity and phase velocity. Group velocity represents the velocity with which the energy of the wave packet travels. It was measured in this study from the arrival time of the wavelet energy peak at two receivers at a known distance from each other (Meo, Zumpano et al. 2005). Group velocity is defined as:

$$c_g = \frac{d\omega}{d\gamma} \qquad (3.1)$$

Where ω is the angular frequency and γ the wave number, and hence dω/dγ is a medium characteristic which can be determined from a wave number dispersion curve. Phase velocity is the velocity related to an individual frequency in the tone burst and is given by:

$$c_p = \frac{\omega}{\gamma} \qquad (3.2)$$

Phase velocity was measured in this study from the arrival time of the wavelet energy peak at a single frequency.

It is apparent that, for dispersive media, group velocity and phase velocity differs, and that each wave mode contains a range of phase velocities that can be derived from the dispersion curve. The shape of the wave changes over time accordingly, and the rate of change is directly related to the rate of change of phase velocity with frequency-thickness. In other words, if the central

frequency of a tone burst is chosen in a flat region of the dispersion curve, the dispersion will be low.

Guided waves can travel at large distances with little energy loss, which makes them particularly attractive for the SHM of large, plate-like structures. The distance that guided waves can travel is governed by attenuation. If the attenuation is high, the propagation distance is limited and vice versa. Since attenuation is mode and frequency dependent, curves similar to dispersion curves can be used in the selection of modes for SHM (Guo and Lim (1996); Castaings and Hosten (2003); Qi, Rose et al. (2008)). A figure from Guo and Lim (1996) is reproduced here in Figure 16 to illustrate this point. The attenuation curve in this figure represents theoretical values for attenuation in an aluminium/aramid honeycomb sandwich construction. It can be seen that attenuation of the A_0 and S_0 modes is low at low frequencies, but increases rapidly when the frequency reaches above 3 MHz. At the low frequency region, the attenuation was predicted to be around 0.025 Nepers/mm, which is around 0.217 dB/mm (1 Neper = 8.7 dB). This means the amplitude drops to roughly 61% of its initial value for every 20 mm travelled. It is clear, then, that even the slightest increase of attenuation can greatly decrease the distance at which the signal can be recognized and separated from noise.

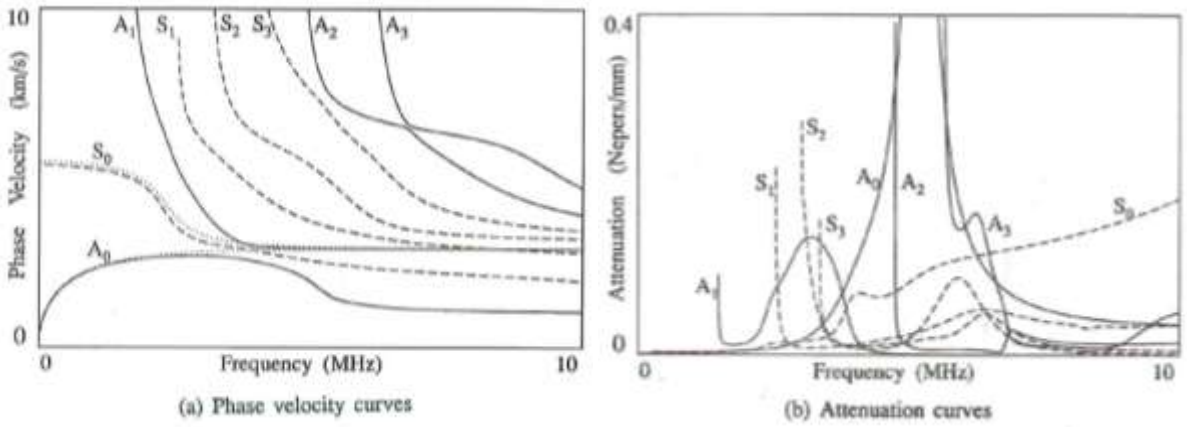

Figure 16 | Dispersion curves for Lamb waves in a 1mm thick aluminium honeycomb (1mm aluminium + 0.1mm epoxy with half space aramid core), dotted lines represent curves for the aluminium plate alone (Guo and Lim 1996).

In sandwich composites, attenuation is higher than in monolithic laminates due to the presence of the core. For foam cores, attenuation is highly influenced by the density of the core. This was shown by Bourasseau, Moulin et al. (2000), who compared the attenuation of a 400kHz tone burst in a GFRP skin panel to that in sandwich panels made of the same skin material and two foam cores with different density. The measurements reported showed a significant attenuation when the skin alone was compared to the sandwich. The measured amplitude of the 400 kHz tone burst after travelling a 17 cm distance in the sandwich structure (with 130 kg/m^3 core density) was roughly 10% of the amplitude measured in the skin alone under similar conditions. For the higher density core (160 kg/m^3) this number was roughly 2%.

3.2 Wave Propagation in Sandwich Structures

The introduction to wave propagation modes in section 3.1 is limited to isotropic media. In sandwich composites, however, the through-thickness stiffness and density distribution of the medium is highly anisotropic. Also, skin and core may be produced from anisotropic materials, introducing material property dependence on propagation direction. The propagation of guided waves in sandwich structures thus differs greatly from that in a single, isotropic plate.

Depending on the acoustic impedance of the core, the sandwich construction can be approximated with different analytical models. If the acoustic impedance of the core can be neglected, the skins can be approximated as monolithic, layered media surrounded by semi-infinite half space vacuum on both sides. This suggests that no acoustic coupling exists between the two skins. In general, however, the acoustic impedance of the core cannot be neglected, and the assumption of semi-infinite half space vacuum is not valid. This requires a semi-infinite half space with the core properties to be incorporated in the model, which allows for acoustic coupling to occur between the two skins. Whether coupling occurs, and how it manifests itself, depends on the material properties as well as relative and absolute thickness of both skin and core, and the wavelength and phase velocity of the signal under consideration (and therefore frequency).

In this section, four modes of wave propagation are considered, the occurrence of which depends on the central frequency of the pulse: Global Lamb Waves (GLWs)[1], True Modes, Leaky Lamb Waves (LLWs) and Rayleigh Waves (RWs) (Mustapha and Ye 2014). The overview presented here was compiled from open literature to come to a comprehensive classification of guided wave propagation modes in sandwich composite structures.

3.2.1 Global Lamb Waves (GLWs)

When the wave length is about twice the panel thickness or longer, flexural (e.g. A_0) Lamb Waves propagate through the sandwich construction as if it were a single plate, thus bounded by the outer surfaces of the two skins (Thwaites and Clark 1995). Song, Huang et al. (2009) identified the A_0 GLW in a FE model of an aluminium/Nomex sandwich structure at a frequency-thickness product of 85 kHz·mm, at which point the wave length was roughly 5 times the sandwich panel thickness. Further analysis showed that the sensor response to GLWs can be adequately modelled using FEA and a simplified continuum model of a honeycomb sandwich structure as a three-layered composite material.

Contrary to asymmetric modes, S_1 GLWs have been shown to occur also for wavelengths less than twice, but larger than once the panel thickness (Gao, Ali et al. 2010). An explanation may be found from the displacement profiles in Figure 13 and Figure 14. If we approximate the displacement in the x-direction by a sine function, we can see that the profile of the A_0 mode corresponds to one half wavelength or less, and that of the S_1 mode to approximately one wavelength. Experimental results confirming similar relations for other modes were not found in this literature study. By extension, however, we may argue that the displacement profile of the S_0 mode in the x-direction corresponds to roughly 1/8 wavelength.

[1] For lack of a generally accepted term, 'Global Lamb Waves' is introduced here after Song, Huang et al. (2009).

The above suggests that the theoretical frequency threshold for the occurrence of GLWs depends on the Lamb wave mode under investigation, and thus on frequency-thickness product as can be derived from the dispersion curves. For the structure under investigation, the frequency threshold for A_0 GLWs is determined by plotting the line $\lambda=2h$ in the dispersion curves for the sandwich structure. The same was done for the frequency threshold for S_0 GLWs by plotting the line $\lambda=8h$.

The results are shown in Figure 17, with the unit of the horizontal axis taken as frequency only. The dispersion curves in this figure were calculated using the Matlab® code developed by Pant Pant, Laliberte et al. (2014). For these calculations, a lumped model of the sandwich structure was used, treating it as a monolithic panel made of isotropic material. The mechanical properties of this material were that of the sandwich constituents, taken in the 0° direction, combined and averaged over their respective thicknesses. This approach was expected to be reliable for the S_0 mode at low frequencies only, where the wavelength was much larger than the panel thickness. The dispersion curves of the S_0 mode were verified experimentally (see section 4.2). From Figure 17 it can be seen that A_0 GLW's should be expected to occur for frequencies below 200kHz, whereas S_0 GLW's may be expected to occur for frequencies below 120kHz.

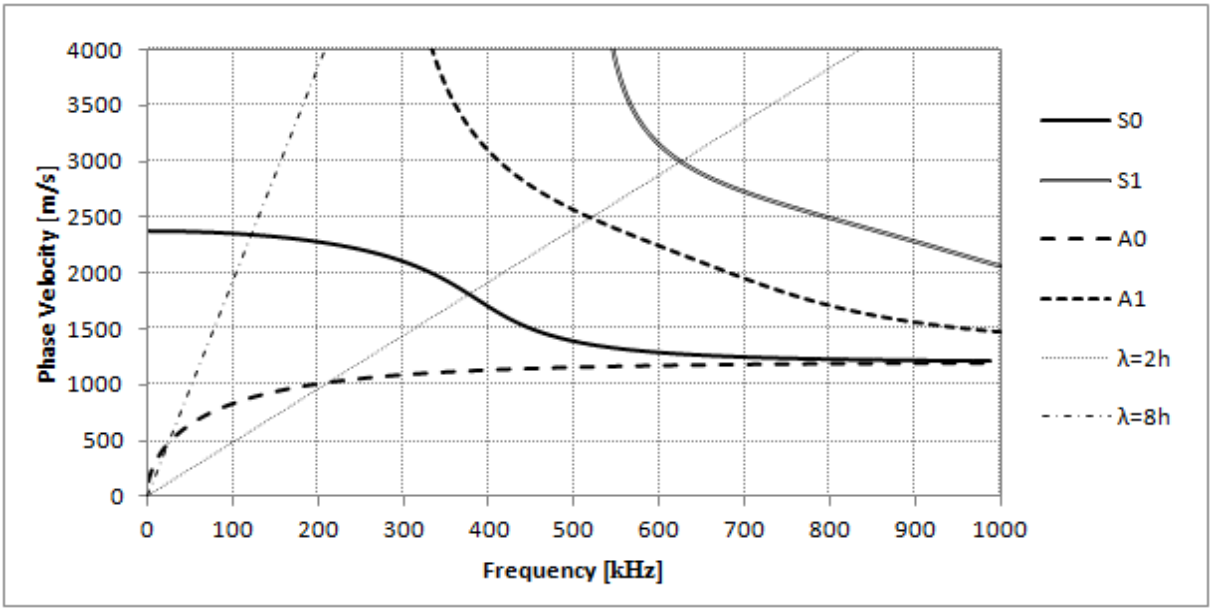

Figure 17 | Sandwich phase velocity dispersion curves with A_0 and S_0 GLW threshold.

Attenuation of GLWs in sandwich composites is high when compared to single laminates due to the presence of the core. Nonetheless, GLWs have been successfully used at distances up to roughly 900 mm (Mustapha, Ye et al. 2011).

It should also be noted here that multilayered composites, such as sandwich structures, do not necessarily have a symmetric centre plane. As a result, the conventional displacement fields of the symmetric and asymmetric Lamb wave modes may not apply (Gao, Ali et al. 2010). Also, due to the large difference in both thickness and stiffness between core and skins, wave energy of GLWs in sandwich composites is mostly concentrated in the skin. This may be beneficial for SHM

applications, since wave energy concentration in the skin suggests higher sensitivity to damage in that region (Lowe and Cawley 1994).

3.2.2 True Modes and Leaky Lamb Waves

When the frequency is increased above the GLW threshold, the lamb waves start to become contained in the skin alone as true modes (Lowe and Cawley (1994); Bertoni and Park (1981)). True modes exist when their phase velocity is lower than the bulk shear velocity of the core and are characterized by low attenuation, comparable to that of bulk waves. The presence of the core has little to no influence on the dispersion characteristics of true modes (Soutis and Diamanti 2008).

When the phase velocity of the mode contained in the skin exceeds the bulk shear velocity of the core, the mode can be characterized as Leaky Lamb Wave (Bertoni and Park 1981). In this mode, most of the wave energy is contained in the skin, while attenuation is large due to energy dissipation into the core in the form of waves travelling in the thickness direction. In a dispersion curve of the skin, leaky modes can be indicated to occur in two stages: shear leaking when the Lamb wave speed exceeds the bulk shear velocity (c_S) of the core, and both shear and longitudinal leaking when the Lamb wave speed also exceeds the bulk longitudinal velocity[2] (c_L) of the core (Lowe and Cawley (1994), Fujita and Toda (2004)).

In the current study, the bulk shear and longitudinal wave velocities in an isotropic medium are calculated from (Giurgiutiu 2008):

$$c_S = \sqrt{\frac{G}{\rho}} \tag{3.3}$$

$$c_L = \sqrt{\frac{1-\nu}{(1+\nu)(1-2\nu)}\frac{E}{\rho}} \tag{3.4}$$

With G, ρ, ν and E the medium's shear modulus, density, Poisson's ratio and tensile modulus respectively. By plotting these velocities as calculated for the core in the dispersion curve of the sandwich, the regions of leaky and non-leaky behaviour can be identified (see Figure 18). Since the bulk wave velocities in the core material depend on the physical properties, each sandwich construction will show different LLW characteristics.

Guo and Lim (1996) showed that modelled attenuation in an aluminium honeycomb sandwich composite (1 mm aluminium skin, 0.1 mm epoxy adhesive, semi-infinite aramid core assumed to be isotropic) is highly dependent on mode and frequency. This suggested that the amount of wave leakage not only depends on geometry and acoustic impedance of the core, but also on the mode and frequency under investigation. This was confirmed by Song, Huang et al. (2009), who found that the attenuation of LLWs is larger for the A_0 mode than it is for the S_0 mode. They attributed this difference to the wave field profiles through the thickness. Since the out-of-plane particle

[2] The bulk shear and longitudinal velocity is the velocity of 3-D shear and longitudinal waves in an isotropic medium, where shear waves are characterized by a particle motion perpendicular to the propagation direction of the wave and longitudinal waves by a particle motion parallel to the propagation direction (Giurgiutiu 2008).

displacement is dominant in the A_0 mode, more wave energy can be dissipated into the core. In the S_0 mode the in-plane displacement is dominant and thus most wave energy is retained in the skin.
Apart from increased attenuation, the presence of the core material has no significant influence on the shape of LLWs. It was shown in various studies that in the LLW frequency range, the dispersion of signals in a sandwich construction was identical to that of the same signal in the skin alone (Guo and Lim (1996), Bourasseau, Moulin et al. (2000); Osmont, Devillers et al. (2001); Song, Huang et al. (2009)). A small reduction of group velocity of roughly 4% under the presence of a honeycomb core was reported by Mustapha, Ye et al. (2011) and a non-quantified reduction was also reported by Bertoni and Park (1981).
Studies have shown that the energy dissipated into the core is not necessarily lost, depending on the core thickness and acoustic impedance. Refracted waves propagating through the core can reach the opposite skin, generating new LLWs. These LLWs refract again into the core and the process continues, as illustrated in Figure 19. Occurrence of this phenomenon depends on the acoustic impedance of the core. Acoustic impedance of a lower density foam may be too weak to induce significant wave leakage, thus not allowing the wave energy to reach the opposite skin (Bourasseau, Moulin et al. 2000).

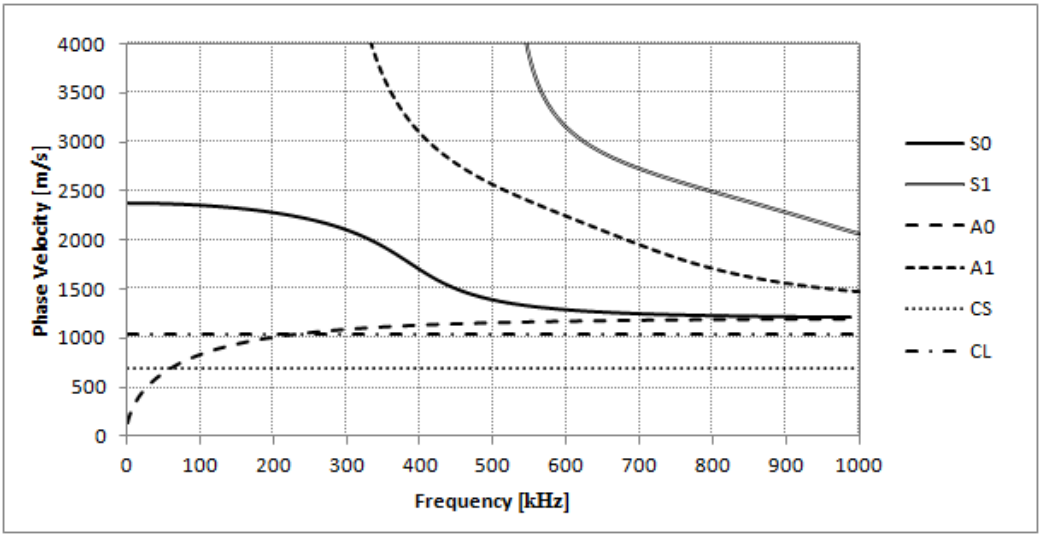

Figure 18 | Sandwich phase velocity dispersion curve with bulk velocities.

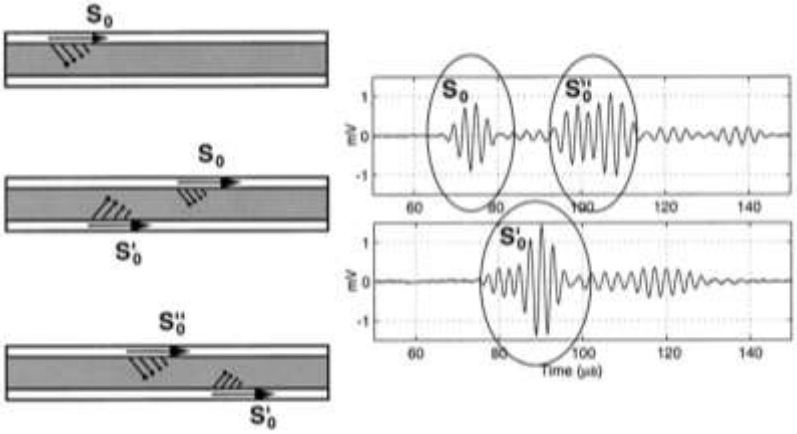

Figure 19 | Sequence of S_0 leaky modes (Bourasseau, Moulin et al. 2000).

To arrive at an estimation of the time difference between refracted waves, we can calculate the distance travelled in the core through the radiation angle ϑ (see Figure 20). The radiation angle of longitudinal wave leakage into the core can be calculated from (Fujita and Toda 2004):

$$\theta = \sin^{-1} \frac{c_{L,c}}{c_{P,s}} \qquad (3.5)$$

Where $c_{P,s}$ is the phase velocity in the skin and $c_{L,c}$ the longitudinal bulk velocity of the core. Replacing $c_{L,c}$ by the shear bulk velocity of the core $c_{S,c}$, the radiation angle of shear leakage into the core can be calculated. Combined with the respective bulk velocities and the thickness of the core, the radiation angles can be used to estimate the time required for the leaky waves to reach the opposite skin (Δt), using:

$$\Delta t = \frac{h_c}{c_{L,c} \cos\theta} \qquad (3.6)$$

Where h_c is the thickness of the core and $c_{L,c}$ can be replaced by $c_{S,c}$ for shear leakage. It is assumed here that the core is isotropic, and thus the longitudinal and shear bulk velocities are independent of propagation direction.

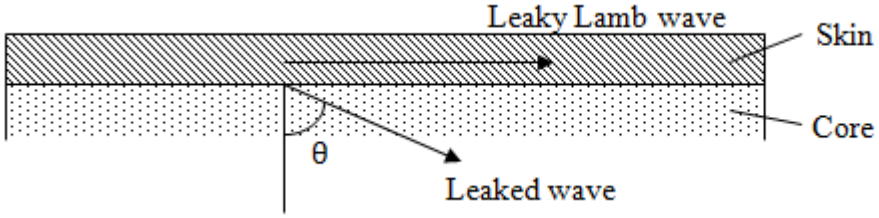

Figure 20 | LLW Radiation angle.

The expected time difference between refracted LLWs for the sandwich structure under consideration was estimated as follows. Using a frequency of 200kHz, the phase velocity in the skin was derived from the skin dispersion curves in Figure 15, giving a phase velocity of 3,600 m/s for the S_0 mode and 450 m/s for the A_0 mode. Next, $c_{L,c}$ and $c_{S,c}$ were calculated from equations (3.3) and (3.4) to be 1,043 m/s and 685 m/s, with the core mechanical properties from Table 6. From this, it was concluded that the S_0 mode is (shear and longitudinal) leaky at 200kHz because it's phase velocity exceeds both the longitudinal and shear bulk velocities of the core, while the A_0 mode is not. Using equation (3.5), the radiation angle of the S_0 LLW at 200kHz was then calculated to be anywhere between 0.2 and 0.3 radians, which resulted in a Δt of 2 to 3μs when the core thickness in equation (3.6) was taken to be 2 mm. Thus, two subsequent refracted LLWs may be expected to be spaced 4 to 6μs, since the second waveform crossed the core twice.

If the pulse used is a 5 cycle Hanning windowed tone burst at central frequency 200kHz, the duration of the tone burst can be calculated to be 25μs, roughly five times the time difference calculated above. Clearly, then, the refracted waveforms should be expected to overlap, which will

make it next to impossible to identify them. For this reason, it was concluded that LLWs should be avoided in an active acoustic SHM system for the DragonFly fuselage.

3.2.3 RAYLEIGH WAVES

When the thickness of the medium is one wavelength or higher, a convergence of the A_0 and S_0 guided wave modes to Rayleigh waves occurs (Fujita and Toda (2004); Mustapha and Ye (2014)). Rayleigh waves are non-dispersive, which is reflected by flat regions in the dispersion curve. This can be recognized in the dispersion curve for a given medium by the convergence of the A_0 and S_0 modes at high frequency-thickness products. As may be obvious, such convergence can be achieved either by increasing the frequency, or by increasing the thickness of the medium. A common approximation of the Rayleigh wave speed c_R is given by (Giurgiutiu 2008):

$$c_R = c_S \left(\frac{0.87 + 1.12\nu}{1+\nu} \right) \qquad (3.7)$$

Where ν is the medium's Poisson's ratio.

Rayleigh waves are surface waves that penetrate at most one wavelength into the depth. This means that energy dissipation into the core may not occur if the wavelength is less than the skin thickness. Also, attenuation of Rayleigh waves is near zero. Hence, Rayleigh waves allow for long propagation distance with high sensitivity to defects near the surface. However, the high frequency-thickness products required will cause higher order Lamb wave modes to occur which greatly complicates signal processing.

3.3 Sensitivity to Impact Damage

The sensitivity of a wave mode to a given damage type and location depends on wave length and through-thickness particle displacement profile. Dependency on wavelength is contained in the diffraction limit, which states that a flaw is detectable when its size is in the order of one half wavelength or more (Worden, Farrar et al. 2007). Smaller flaws generally create insufficient scatter to be detected in an active acoustic SHM system. As Worden, Farrar et al. (2007) pointed out, several researchers have found evidence that damage detection below the diffraction limit is possible.

Apart from the diffraction limit, we may expect that a guided wave mode is most sensitive to damage at the (through thickness) location where the wave energy is highest and when the damage is perpendicular to the direction of wave energy propagation. For example, true, LLW and RW modes are largely contained in the skin, and will therefore be particularly sensitive to the properties and boundary conditions of the skin. GLWs on the other hand may be affected by the properties and boundary conditions of the entire sandwich structure, where specific sensitivity depends on the displacement profile of the Lamb Wave mode concerned (Lowe and Cawley 1994).

As will be seen in this section, no application of true and RW modes was encountered in open literature. This is understandable for two reasons. First, generation of these modes requires relatively high frequency-thickness products, which promotes the occurrence of multiple Lamb

wave modes. Researchers generally avoid this because it greatly complicates the analysis of received signals. Second, both true and RW modes are contained in the skin while for BVID the most significant damage modes in terms of size are contained in the core (e.g. core crushing) and in the skin-core interface (e.g. debonding), as was found in section 2.2. As a result, the sensitivity of true and RW modes to BVID may be expected to be very low. GLWs and LLWs do show sensitivity to impact damage and numerous applications of these modes were found in open literature.

3.3.1 Simulated Impact Damage

In the majority studies concerning active acoustic SHM for the detection of impact damage in sandwich composites using a pitch-catch setup, impact damage was reduced to a simulated form of skin-core debonding. This was done for example by inserting a Teflon film between skin and core during specimen production (Thwaites and Clark (1995), Song, Huang et al. (2012)), by leaving out adhesive (Hay, Wei et al. (2003)) or by inserting a sharp blade to locally separate the skin from the core (Qi, Rose et al. (2008), Mustapha, Ye et al. (2011) & (2014)). The study of actual impact damage has received far less attention, as such this topic is addressed further in section 3.3.2.

Because GLWs propagate through the sandwich construction as a whole, it is reasonable to assume that minor changes in the properties of sandwich constituents that are orders of magnitude thinner than the sandwich as a whole (e.g. the skins) may not significantly affect GLWs (Lowe and Cawley 1994). It has been shown, however, that GLWs can be used in sandwich structures using a pitch-catch setup, most notably for the detection of skin-core debonding.

Thwaites and Clark (1995) investigated the influence of different types of damage in honeycomb/CFRP sandwich plates on the phase velocity of A_0 mode GLWs of frequencies up to 30 kHz. They simulated different types of damage, including: crazed core by perforating the honeycomb before lay-up and delamination by introducing 25 mm square Teflon wafers between skin and core during lay-up. Wave source and transducer were moved in the transverse direction along the damage location, thus generating data for the pristine and damaged structure in a continuous fashion.

Measurements showed a clear decrease of phase velocity under the presence of crazed core, due to local decrease of stiffness in the core. The same was shown for delamination, which was attributed by Thwaites and Clark (1995) to scattering of the incident wave from the defect causing distorted phase fields. Similar findings were presented by Osmont, Devillers et al. (2001), who simulated debonding in a foam/GFRP sandwich panel – and consequential uncoupling between the skins – with through thickness holes in the core. They used holes of 20, 40 and 60 mm diameter and low frequency Lamb waves of 10 to 30 kHz. Scattering was found in their experiments for damage sizes above the diffraction limit, and numerical simulations showed that when the wave packet entered the area where the defect in the core began (e.g. no core is present), the speed of the waves was reduced.

This reduction of GLW propagation velocity under the presence of debonding is highly dependent on damage size, as was found by Mustapha, Ye et al. (2011). They studied the ToF of a boundary

reflected signal of the A_0 GLW mode at low frequency (6.5 kHz) in CFRP/honeycomb sandwich composite beams and compared measurements for an undamaged benchmark with measurements for beams with de-bonding of different sizes, which was simulated by introducing a cut between the core and the skin. Figure 21 shows how the delay of ToF depended on damage size.

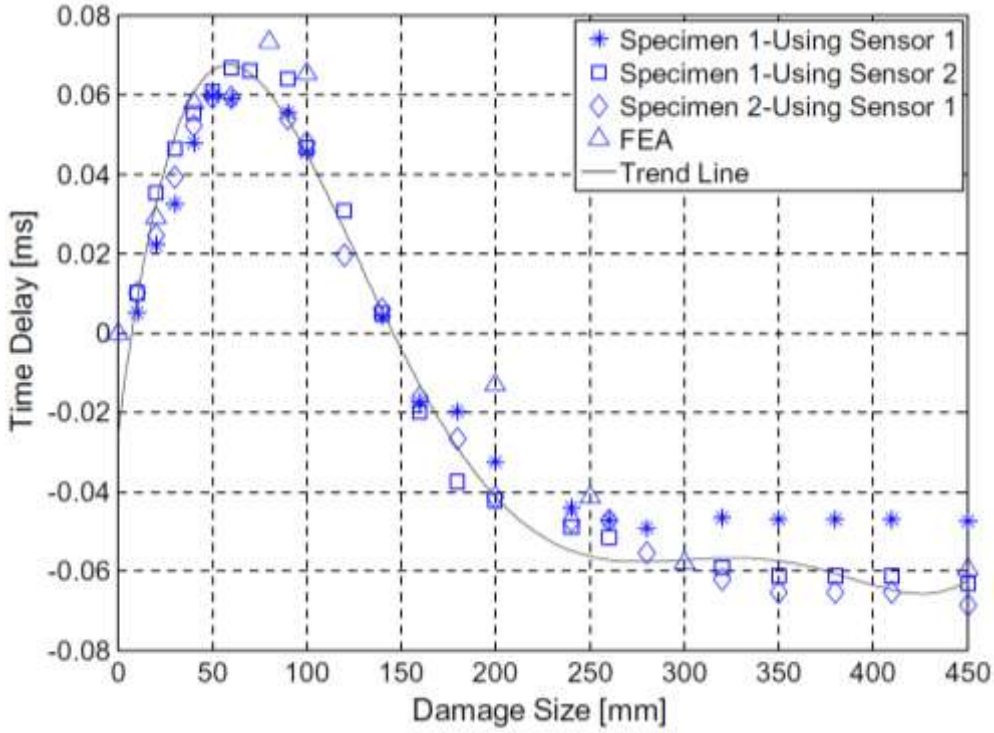

Figure 21 | Correlation between debonding extent and delay in ToF in sandwich composite beams (Mustapha, Ye et al. 2011).

The results showed that an increasing time delay occurred when GLWs encountered de-bonding and that a maximum existed after which the time delay decreased and became negative, i.e the ToF was decreased instead of increased. This phenomenon was explained through the notion that the Lamb waves travelled in the skin when de-bonding became large, which allows them to travel faster due to higher medium stiffness.

Another feature of GLWs that is affected by debonding is the magnitude of the through-transmitted signal. Mustapha and Ye (2014) demonstrated that the magnitude of an A_0 GLW decreased as compared to an undamaged benchmark when it propagated through a region with de-bonding. A comparable feature was used by Gao, Ali et al. (2010) to detect delamination in a copper/brass layered structure used as a bulk material for coin production. They measured the amplitude of the first symmetric (S_1) GLW mode transmitted through an area with de-bonding of increasing size. Both experimental and FE simulation results showed a periodic behaviour of the through-transmitted amplitude as a function of de-bonding width (see Figure 22).

This phenomenon was explained through the notion of mode decomposition: when the GLW entered the de-bonded zone, the wave was decomposed into two separate modes propagating in the

two separate de-bonded layers, in the following referred to as sub-systems. Both modes had their own phase and group velocity, which resulted in interference when the end of the de-bonding was reached. Mode conversion then generated transmitted and reflected wave modes. The periodicity of the through-transmitted amplitude occurred because the two wave modes arrived at the end of the de-bonding either in phase or out of phase, and as a result the original mode was either well or poorly transmitted through the de-bonding.

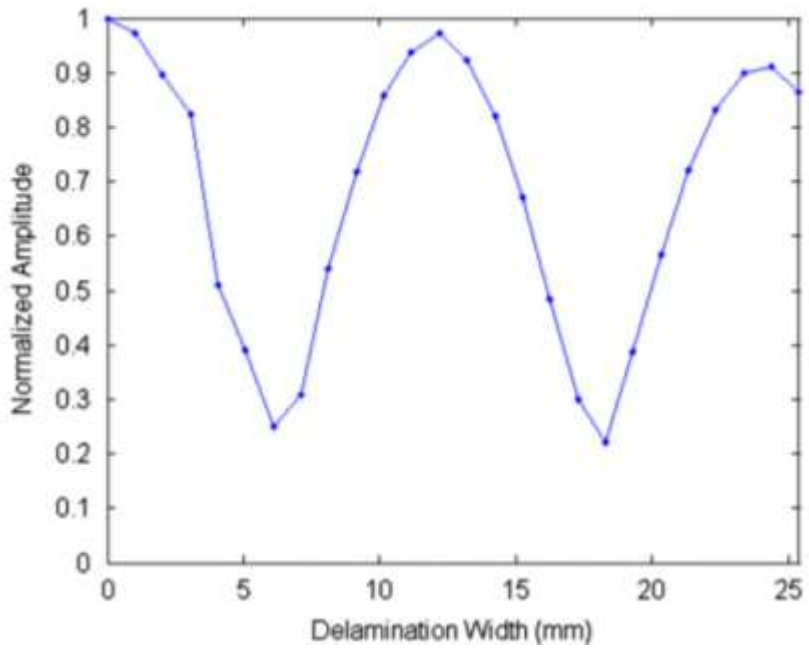

Figure 22 | Simulated result of guided wave amplitudes as a function of defect width (Gao, Ali et al. 2010).

An effective feature of LLWs for the detection of skin-core de-bonding in a pitch-catch setup is amplitude. If an LLW encounters skin-core de-bonding on its propagation path, less energy can dissipate into the core and the attenuation may be expected to be less severe when compared to a pristine specimen. In the application of this principle, a trade-off has to be made between sensitivity and propagation distance, since higher attenuation gives higher sensitivity but shorter propagation distance (Mustapha and Ye 2014).

This principle was employed by Hay, Wei et al. (2003), who found an increased amplitude of an LLW transmitted through a de-bonded area when compared to a pristine specimen. In their experiments, de-bonding was simulated by leaving out skin-core adhesive in a circular and rectangular area. They showed that sensitivity to de-bonding was higher for a wave mode where the particle displacement was concentrated at the skin-core interface. The specimen was fabricated from a single CFRP skin bonded to a honeycomb core with epoxy. Measurements were conducted with wedge transducers at 400 and 500 kHz, with phase velocities 4200 and 3900 m/s respectively.

Using a comparable simulated de-bonding Song, Huang et al. (2012) were also able to show an increased amplitude of an LLW transmitted through a de-bonded area. In their experiments, debonding was simulated by inserting a rectangular Teflon film (30 x 10 x 0.1 mm) into the skin-core interface of an aluminium/Nomex honeycomb sandwich panel of total thickness 19 mm. In FE simulations as well as laboratory experiments the increasing effect of debonding on the

amplitude of an LLW was demonstrated. In the FE simulation, a tone burst with central frequency of 110 kHz was used and the A_0 mode was shown to be more sensitive than the S_0 mode. The same trend was found in the laboratory experiments at a central frequency of 175 kHz, while at a central frequency of 375 kHz only the S_0 mode was clearly seen. No scattering from the simulated damage was seen. The higher sensitivity of the A_0 mode was explained from the particle displacement profile, which shows more out of plane displacement compared to the S_0 mode. As a result, the A_0 mode was expected to leak more energy into the core and thus show higher sensitivity to debonding.

After filtering the received signals using the Fourier transform and a frequency band filter set at the frequency band of the excitation signal, the normalized magnitude in the frequency domain was used by Song, Huang et al. (2012) as a more sensitive feature for debonding assessment. The filtered signals also showed that no severe dispersion was caused by the debonding.

Mustapha and Ye (2014) measured the magnitude of the through-transmitted S_0 and A_0 Lamb mode with a frequency ranging from 25 to 400 kHz for three sandwich composite beams containing foam and honeycomb cores. Damage was simulated by inserting a sharp blade between core and skin to create debonding. They demonstrated that, when leaky behaviour occurred, the magnitude of the signal increased when specimens with debonding were compared to a benchmark specimen. This was attributed to the fact that in the debonded region no energy leakage into the core can occur, and as a result the wave loses less energy when it propagates. They were also able to show that the difference in magnitude increased when the size of the debonding was increased.

Qi, Rose et al. (2008) calculated the through transmission energy as the integral of the squared voltage express function in the time domain. They found a positive linear relation between debonding length (the width was kept constant) and normalized through-transmitted energy of an LLW. Debonding was simulated by inserting a sharp blade at the skin-core interface of a sandwich composite beam with FRP skins and Nomex honeycomb core. The input signal used was a 5 cycle pulse at central frequency 300 kHz.

3.3.2 Actual Impact Damage

In the previous section it was seen that GLWs slow down or speed up under the presence of debonding, depending on debonding size. In addition, it has been documented that crushed core decreases the GLW speed. The amplitude of GLWs was shown to be influenced by debonding as well, and may decrease or increase depending on debonding size. For LLWs, debonding was shown to increase the through-transmitted amplitude. These results were obtained for simulated, singular damage modes. The investigation on actual impact damage has shown less consistent results.

In a study to the sensitivity of LLWs to actual impact damage, Bourasseau, Moulin et al. (2000) used a sandwich composite structure used for radar domes, which are typically made of a GFRP/foam sandwich construction for minimal interference with radar signals. In this case, a 10 mm thick, low density foam (130 and 160 kg/m^3) was used with 1 mm GFRP skins to produce a sandwich panel. The selected feature for further analysis was the amplitude of the S_0 mode, because it was shown to have non-dispersive properties below a frequency of 1 MHz. Also, at 400

kHz it was shown that higher order modes do not appear, which simplified the interpretation of signals.

Panels were impacted with a 1 kg hemispherical impactor at impact energies 10 and 20J. A 400 kHz, 5 cycles Hanning windowed tone burst was emitted on one skin and captured on both skins using the standard wedge method. It was hypothesized by the authors that local loss of coupling between skin and core due to impact damage could reduce attenuation because less wave energy leaked into the core. This implied that a de-bond between skin and core could be detected by comparing the attenuation in the undamaged structure to that in the damaged structure. The researchers were unable to experimentally confirm this hypothesis. As indicated by the authors, the most probable explanation was that other damage modes (e.g. matrix cracking and broken fibres) increased attenuation, thereby cancelling the effect of de-bonding. This also explains why their findings contradicted those of researchers who used simulated debonding (Hay, Wei et al. (2003), Song, Huang et al. (2012)).

Measurements performed by Bourasseau, Moulin et al. (2000) demonstrated the feasibility of using the second waveform (see section 3.2.2 and Figure 19) to detect de-bonding and damages in the core by selecting the feature of amplitude. When transmitted through a damaged zone, the amplitude of the second waveform reduced significantly when compared to the pristine sample because no energy could leak from the first waveform into the second when core damage was present.

A consistent trend was found by Soutis and Diamanti (2008), who studied the ToF of the far boundary reflection of an A_0 LLW transmitted through impact damage of increasing severity. Specimens were impacted with a 1.54 kg hemispherical impactor with 12.5 mm diameter. Impact tests were repeated with higher energies until substantial damage had accumulated, which consisted of de-bonding of the skin, crushed core and delaminations in the skin. Then, a 6.5-cycles, 15 kHz sinusoidal pulse enclosed in a Hanning window with amplitude ±10 V was transmitted from one end of the beam and the reflection from the far boundary was received by receivers on the top and bottom skin on the same end. The measurements showed that the ToF of the far boundary reflection increased up to 6% with increasing impact energy. This effect was attributed to a decrease of effective thickness in the delaminated area, giving a decrease of frequency-thickness product and consequently a decrease of phase and group velocity according to the dispersion characteristics of the A_0 mode. The amount of time increase was shown to correlate with the size of damage in the propagation direction.

3.4 Mode Selection

The aim of the current study was to investigate the interrogation of the outer skin of a sandwich structure with actuators and sensors placed on the inner skin. This required a signal that either excites the entire structure, here referred to as Global Lamb Waves (GLWs), or a signal that propagates through the thickness and back, here referred to as Leaky Lamb Waves (LLWs).

Starting with the latter, it was found in section 3.2.2 that the time spacing between subsequent leaky waveforms was 4 to 6 μs in the DragonFly fuselage structure. As a result, waveforms would

overlap and features for damage detection would be very difficult to extract. For this reason alone, the LLW mode was considered to be a poor candidate for active acoustic SHM using a pitch-catch setup. For thicker sandwich structures, this mode has shown promising results when the waveforms do not overlap.

Compared to LLWs, GLWs appeared to be the more obvious choice for the application under consideration. Especially since GLWs should be easy to generate as the structure was thin. As was seen in section 3.3.2, no studies were found in open literature that used GLWs in a pitch-catch setup for the detection of real impact damage. Rather, only simulated, singular damage modes (i.e. debonding and core crushing) have been investigated.

When using GLWs in a pitch-catch setup, the S_0 mode was expected to be sensitive to all damage modes because it causes particle displacement through the thickness. Mode decomposition was expected to occur when debonding was present. Since the propagation velocity of the S_0 was much higher in the skin, mode decomposition was expected to result in a decrease of ToF. Under the presence of multi mode impact damage, it was expected that attenuation of the signal would increase, thus decreasing the through-transmitted energy.

Since no reference studies on the use of GLWs in a pitch-catch setup for the detection of actual impact damage were found in open literature, a proper analysis of the sensitivity of ToF and attenuation to impact damage in sandwich composites required additional research. For this reason, the current study was focused on a pitch-catch setup using GLWs. Modelling and experimental verification were used to provide a better understanding of the sensitivity to impact damage in such a setup and facilitate implementation of SHM in the DragonFly fuselage.

3.5 Feature Extraction

To determine the Time of Flight (ToF), group velocity and energy of a received signal, a post processing technique was required that enables analysis of transient signals in the time-frequency domain. The Wavelet Transform (WT) is a powerful technique that offers good resolution in both the time and frequency domain (Giurgiutiu 2008). The continuous WT of a time-domain signal $f(t)$ is given by (Reda Taha, Noureldin et al. (2006); Sohn, Park et al. (2004)):

$$WTf(a,\tau) = \frac{1}{\sqrt{a}} \int_{-\infty}^{\infty} f(t)\psi\left(\frac{t-\tau}{a}\right)dt \qquad (3.8)$$

Where $\psi(t)$ is the wavelet function that is used as basis function in the WT and a and τ are the scaling and shift parameters of the wavelet function. The WT of $f(a,\tau)$ gives the time-frequency component of $f(t)$ near time τ and frequency ω_0/a. By calculating the WT of $f(t)$ while independently changing a and τ, the time-frequency component of $f(t)$ can be obtained on the time-frequency plane.

Various basis functions $\psi(t)$ can be used in the WT. Recorded signals were processed using AGU-Vallen Wavelet R2014.0414.3 software, which generates the wavelet transform (WT) using the Gabor wavelet. It was shown by Kishimoto, Inoue et al. (1995) that the square magnitude of the

WT calculated with the Gabor wavelet corresponds to the energy spectrum. Furthermore, the Gabor wavelet has a proven track record in the analysis of dispersive waves in SHM (Kishimoto, Inoue et al. (1995); Wang and Yuan (2007)). The Gabor wavelet is given by:

$$\psi_g(t) = \frac{1}{\sqrt[4]{\pi}}\sqrt{\frac{\omega_0}{\gamma}}\exp\left[-\frac{\left(\omega_0/\gamma\right)^2}{2}t^2 + i\omega_0 t\right] \quad (3.9)$$

Where ω_0 and γ are positive constants. The wavelet function was scaled at 500 data points to obtain a good trade-off between time and frequency resolution (Giurgiutiu 2008).

An example of a WT diagram is given in Figure 23. In a WT diagram, the magnitude of the WT is indicated using colour scaling on a time-frequency grid. This allows us to determine at which time a peak occurs for which frequency. By measuring the time travelled by a WT peak at a chosen frequency between two sensors placed at known distance from each other, we can accurately calculate the group velocity (Kishimoto, Inoue et al. 1995) from:

$$c_g = \frac{ds}{dt} = \frac{ds}{ToF} \quad (3.10)$$

Where ds is the distance between two locations and ToF the Time of Flight: the time travelled by the WT peak between those locations at a given frequency. The ToF between two locations 1 and 2 can be calculated by subtracting the Time of Arrival (ToA) at those two locations:

$$ToF = ToA_2 - ToA_1 \quad (3.11)$$

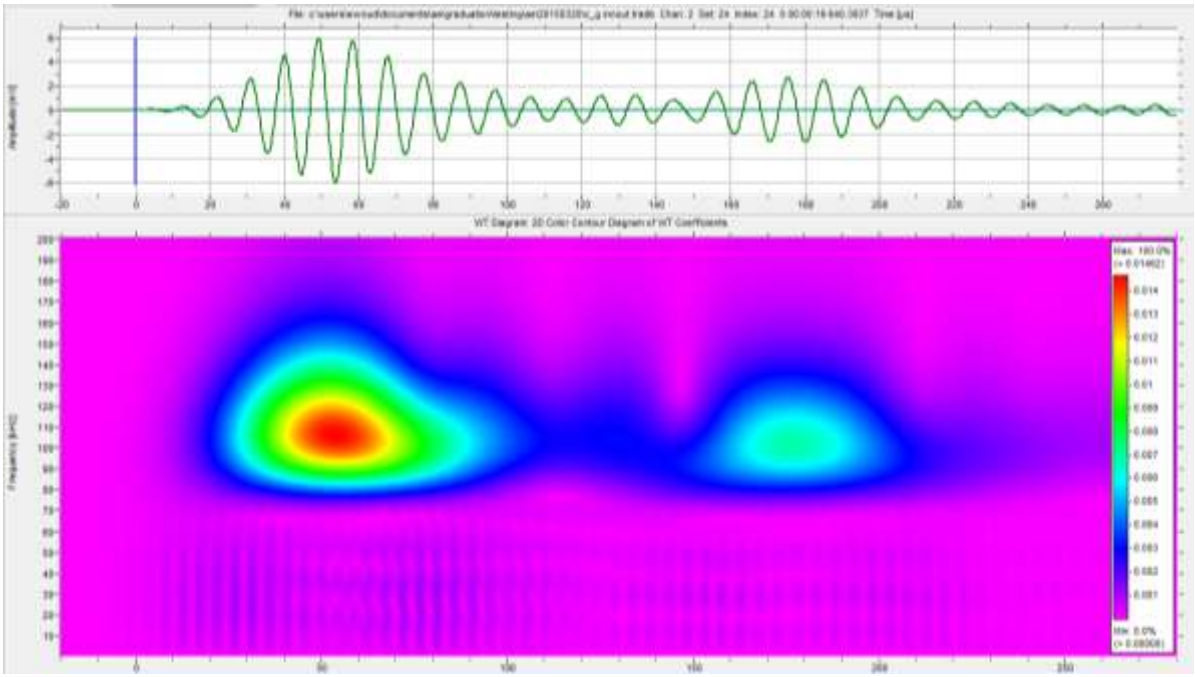

Figure 23 | Example of a received signal and its WT diagram.

To determine the sensitivity of the signal peak energy to damage, the energy level was defined as follows:

$$E = |WT|^2 \qquad (3.12)$$

Where $/WT/$ indicates the magnitude of the wavelet transform peak at the selected frequency.

When the amount of attenuation between two locations 1 and 2 was calculated, it was also determined based on the energy of the WT peak at the selected frequency:

$$Attenuation = \frac{|WT_2|^2 - |WT_1|^2}{|WT_1|^2} \cdot 100\% \qquad (3.13)$$

Thus, attenuation was considered in terms of percentage loss of energy.

4 Experimental Setup and Results

Four series of experiments were conducted in this study: material characterization, frequency selection, impact tests and SHM experiments. The material characterization was performed to generate the input engineering constants for modelling. The experimental setup for the required tests is given in section 4.1. Frequency selection experiments are treated in section 4.2. The aim of these experiments was to select a frequency for reliable results in the SHM experiments and thus verify some of the theoretical results on the propagation of Lamb waves through the structure of interest. Section 4.3 treats the impact experiments conducted for the controlled creation of impact damage in specimens, while section 4.4 deals with the experiments focused on the detection of this damage through active acoustic SHM.

4.1 Material Characterization

For an overview of the sandwich structure under investigation in this study, reference is made to section 2.1. The constituent materials of the sandwich structure (i.e. the foam core and the composite laminate skins) were characterized individually to enable accurate modelling of the sandwich specimen that were used in the active acoustic SHM experiments described in section 4.4.

The Rohacell A110 core material used for sandwich specimen preparation was chosen to represent the material to be used for the DragonFly fuselage. Therefore, this material was ordered in panels of 2mm thickness. As a result, ASTM standard test methods for rigid cellular plastics material characterization could not be adhered to, because test specimens of the required dimensions could not be produced from these 2mm thick panels. Since mechanical testing would thus not yield reliable results, engineering constants of the Rohacell A110 core material as provided by the supplier were used.

The GFRP material used for the skins of the sandwich specimens could be produced with the required thickness and the engineering constants of this composite laminate were determined according to ASTM standards as much as possible. The method of testing and calculation is described in the following paragraphs.

4.1.1 Characteristics to be Determined

The GFRP material characteristics as required for dispersion curve calculations and FE modelling are listed in Table 4, together with the method used to measure their corresponding values. The coordinate system referred to in this table is given in Figure 24. Since the material under investigation consisted of a matrix that was assumed to be isotropic an a twill weave fabric reinforcement with equal amount of fibres in the x_1 and x_2 directions, the engineering constants of the laminate in the x_1 and x_2 directions were expected to be identical. This was verified by measuring the Young's modulus in both directions.

Not all engineering constants could be directly determined through ASTM testing procedures and therefore needed to be estimated using the following calculations, all of which are reproduced from the work by Kollár (2003).

Direct estimation of E_3 through tensile testing was deemed impractical, since this would require a laminate thickness of 250 mm. Assuming a series connected model for the transverse direction (constituents under equal stress) and applying the rule of mixtures, the theoretical value E_{3t} of a UD laminate can be calculated from:

$$\frac{1}{E_{3t}} = \frac{V_f}{E_{f3}} + \frac{V_m}{E_m} \tag{4.1}$$

Where E_{f3} and E_m are the fibre transverse and matrix Young's Modulus respectively and V_f and V_m their volume fractions. Because in a cross-ply laminate the plies are rotated around the x_3 axis only, the calculated value of E_{3t} can be used for the out of plane stiffness of the laminate.

G_{23} can be calculated utilizing the same formulation as for E_3. This calculation is also based on the assumption of a cross-ply laminate of isotropic constituents connected in series:

$$\frac{1}{G_{23}} = \frac{V_f}{G_{f23}} + \frac{V_m}{G_m} \tag{4.2}$$

Where G_{f23} is the fibre shear modulus in the x_2-x_3 plane and G_m the matrix shear modulus. For G_{f23} a textbook value of 30 GPa was used (Daniel and Ishai 1994).

Assuming isotropic properties for the matrix material, the shear modulus G_m can be calculated from:

$$G_m = \frac{E_m}{2(1+\nu_m)} \tag{4.3}$$

With ν_m the Poisson's ratio of the matrix.

The Poisson's ratio of the laminate ν_{23} (which is equal to ν_{13} for a cross-ply laminate) may then be calculated from the relation between E_2 and G_{23} for transversely isotropic materials:

$$G_{23} = \frac{E_2}{2(1+\nu_{23})} \tag{4.4}$$

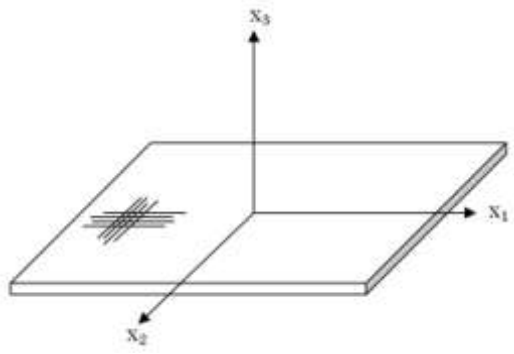

Figure 24 | Coordinate axes definition.

Table 4 | Engineering constants to be determined.

Symbol		Unit	Standard	Specimen (l x w x t)	Material	Plies	Specimen
Skin Material							
E_1	Young's modulus in x_1 direction	MPa	ASTM D3039 (ASTM 2000a)	250x25x2.5	GFRP	16	5
E_2 (=E_1)	Young's modulus in x_2 direction	MPa	ASTM D3039 (ASTM 2000a)	250x25x2.5	GFRP	16	5
E_3	Young's modulus in x_3 direction	MPa	Calculated		GFRP		
v_{12}	Poisson's ratio in x_1-x_2 plain	-	ASTM D3039 (ASTM 2000a)	250x25x2.5	GFRP	16	5
v_{13}	Poisson's ratio in x_1-x_3 plain	-	Calculated		GFRP		
v_{23}(=v_{13})	Poisson's ratio in x_2-x_3 plain	-	Calculated		GFRP		
G_{12}	Shear modulus in x_1-x_2 plain	MPa	ASTM D3518 (ASTM 1994)	250x25x2.5	GFRP	16	5
G_{13}	Shear modulus in x_1-x_3 plain	MPa	Calculated		GFRP		
G_{23}(=G_{13})	Shear modulus in x_2-x_3 plain	MPa	Calculated		GFRP		
ρ	Density	kg/m^3	ASTM D792 (ASTM 2000b)	>20x20x2.5	GFRP	16	2
V_f	Fibre volume fraction		ASTM D3171 (ASTM 2006)	>20x20x2.5	GFRP	16	1
V_m	Matrix volume fraction		ASTM D3171 (ASTM 2006)	>20x20x2.5	GFRP	16	1
t_p	Ply thickness	mm	ASTM D3171 (ASTM 2006)	>20x20x2.5	GFRP	16	1
Core Material							
E	Young's modulus	MPa	Manufacturer data sheet		Rohacell 110A		
G	Shear modulus	MPa	Manufacturer data sheet		Rohacell 110A		
v	Poisson's ratio	-	Manufacturer data sheet		Rohacell 110A		
ρ	Density	kg/m^3	Manufacturer data sheet		Rohacell 110A		

For comparison, we may also model the laminate with a parallel connected model in which the isotropic constituents are under equal strain. The Poisson's ratio then simply follows from the rule of mixtures:

$$\nu_{23} = V_f \nu_f + V_m \nu_m \qquad (4.5)$$

Where ν_f is the Poisson's ratio of the fibres. Because the laminate under investigation may be seen as a combination of both the series and parallel models, ν_{23} is calculated as an average of the two values.

More accurate estimations may result from the modified rule of mixtures, which models the fibre as surrounded by matrix material:

$$\frac{1}{E_3} = \frac{\sqrt{V_f}}{E_{b3}} + \frac{1-\sqrt{V_f}}{E_m} \text{ where } E_{b3} = \sqrt{V_f} E_{f3} + \left(1-\sqrt{V_f}\right) E_m$$
$$\frac{1}{G_{23}} = \frac{\sqrt{V_f}}{G_{b23}} + \frac{1-\sqrt{V_f}}{G_m} \text{ where } G_{b23} = \sqrt{V_f} G_{f23} + \left(1-\sqrt{V_f}\right) G_m \qquad (4.6)$$

Where the voids content of the laminate is assumed to be negligible. When calculating the properties, Equations (4.6) showed a more consistent trend with textbook values from Daniel and Ishai (1994). For that reason, values as calculated with the modified rule of mixtures were used.

4.1.2 Experimental Setup

All material characterization tests were conducted according to the ASTM standards listed in Table 4 and found in the References section of this thesis. Detailed test reports are included in Appendix III to Appendix V.

Coupons were produced through vacuum injection. Details on the production parameters are included in the coupon production logbook sheet (Appendix II).

4.1.3 Results of Material Characterization

Detailed results of the material characterization tests are provided in Appendix III to Appendix V. Table 5 lists the experimental results as determined according to the applicable ASTM standards. Calculated values are added to this table. In the case of E_3, G_{13} and G_{23} the results from the modified rule of mixtures (equations (4.6)) were closer to textbook values from Daniel and Ishai (1994) than the results of the standard rule of mixtures. Hence, these values were used.

Engineering constants of the core were provided by the manufacturer (Appendix I) as listed in Table 6. It is noted here that the value for Poisson's ratio was provided separately through email correspondence with the manufacturer's Technical Sales Manager Rohacell. All engineering constants were determined according to ISO or DIN standards. No statistical data was available.

Table 5 | Skin laminate engineering constants.

Symbol	Experimental value			Calculated value	Unit
	Mean	Standard deviation	Coefficient of variation		
E_1	23.5	0.16	0.69		GPa
E_2	23.4	0.39	1.68		GPa
E_3				7.9	GPa
v_{12}	0.13	0.003	2.18		-
v_{13}				0.32	-
v_{23}				0.32	-
G_{12}	3.8	0.038	1.01		GPa
G_{13}				3.0	GPa
G_{23}				3.0	GPa
ρ	1852	0.71			kg/m^3
V_f				0.45	-
V_m				0.55	-
t_p				0.17	mm

Table 6 | Core engineering constants.

Symbol	Value	Unit	Standard
E	160	MPa	ISO 527-2
G	50	MPa	DIN 53294
v	0.38	-	DIN 53455
ρ	106.6	kg/m^3	ISO 845

4.2 Mode Verification and Frequency Selection

The experiments described in this section were conducted for two purposes. Primarily, to verify the group velocity dispersion curves for the S_0 mode calculated in section 3.2.1. Second, measurements were used to investigate several factors of influence on Lamb wave propagation. The findings of these experiments were used in the selection of excitation frequency for the detection of impact damage through active acoustic SHM (see §4.4). As was seen in section 3.2.1, GLWs were expected to occur for frequencies below 120kHz for the S_0 mode. Above these frequencies, the Lamb waves were expected to become leaky. To verify this expectation, the experimental frequency range was chosen between 80 and 180kHz and 240 and 320kHz. In the study to the effect of damage on the propagation of an acoustic pulse through the sandwich composite DragonFly fuselage structure, the following factors of influence on Lamb wave propagation were considered.

Structural Variations

The sandwich specimens in this study were produced through vacuum infusion. Due to this production process, the surface roughness of the tool side and bag side of the structure differ greatly. Also, the thickness may vary between the two skins as well as within a single skin. This will affect the dispersion and propagation velocity of the acoustic signals, since those depend on the medium thickness. In addition, the efficiency of wave generation and detection with

piezoelectric transducers may be affected by the surface roughness, as the interaction between transducer, adhesive and structure may be different. To obtain some indication on the spread of phase velocity and wave energy, both features were measured on both sides of a sandwich panel.

Attenuation

As was seen in section 3.1, the attenuation of a guided wave is dependent on its frequency. Because an acoustic pulse contains a range of frequencies, some frequency content of the pulse may be more attenuated than others. This means that the shape of the pulse in the frequency domain changes due to attenuation. It is therefore very well possible that the energy peak in a signal shifts in the frequency domain. This, in turn, affects the propagation velocity of the energy peak. If we are to measure the time travelled by the energy peak in a pulse, attenuation will thus have effect on the measurement if no filter for frequency is used. Selecting the frequency that shows the least attenuation may reduce this effect. Another important reason to minimize attenuation is to maximize propagation distance. The amount of attenuation was therefore measured for the frequency range of interest.

Wave Generation

The efficiency of wave generation with piezoelectric transducers depends on the piezoelectric properties and geometry of the transducer, as well as the properties of the interface between transducer and structure (i.e. the adhesive) and the geometry and mechanical properties of the structure itself. For every transducer setup, the generated amplitude changes with frequency as a result of these influences. This should be taken into account when selecting the excitation frequency, since the amplitude greatly influences the distance a guided wave can travel through the structure. To determine the wave generation efficiency, the dependence of wave peak energy on frequency was measured in the frequency range of interest.

Wave Propagation Mode

As was concluded in section 3.4, the current study was focused on the use of GLWs. In order to verify that the wave propagation mode was indeed the GLW and not a mode contained in the sandwich panel skin (e.g. the true or leaky Lamb wave modes), waves were generated on one side of the specimen and captured on both sides. By comparing the wave profiles on both sides, an assessment of the propagation mode was made. As was estimated in section 3.2.2, the time required for an LLW to reach the opposite skin is 2 to 3μs. This time difference was expected to show in the recorded signals.

4.2.1 Experimental Setup

Sandwich panel specimens were produced in a one-shot vacuum assisted resin transfer moulding process, a detailed logbook sheet is provided in Appendix VI. Locations A, B and C were defined at an interval of 10cm on both the toolside (index *t*) and the bagside (index *b*) of specimen 05032015SW2 (see Figure 25). Four transducer arrangements, numbered 1 through 4, were defined as given in Table 7. Arrangements 1 and 3 allowed measurement of group velocity and amplitude

on toolside and bagside respectively, whereas arrangements 2 and 4 allowed measurements on waves transmitted through the entire thickness of the sandwich construction.

The following equipment was used in the experimental setup, given schematically in Figure 26: Laptop running Vallen Acquisition and Vallen VisualAE™, versions R2014.0414.3; Agilent 33500B Series waveform generator; Vallen AMSY-6 (consisting of piezoelectric transducers type 150-RIC, pre-amplifiers and an acoustic signal processor). A waveform generator was used because the AMSY-6 system did not offer the option of sending customized signals. The output of the Waveform Generator was connected to both the transducer at A and the input of the acoustic signal processor, to enable processing of the transmitted signal. Transducers were connected to the specimen using Apizon M grease, which offered sufficient adhesion for transducers to be placed upside down (in arrangements 2 and 4).

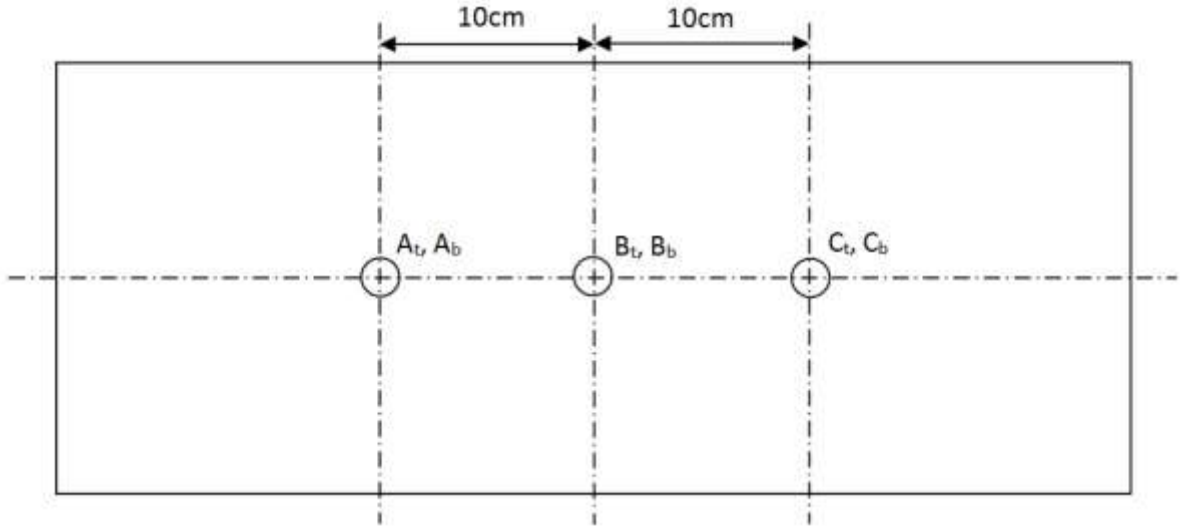

Figure 25 | Transducer arrangement.

Table 7 | Transducer arrangements.

#	Transmitter	Receivers
1	A_t	B_t and C_t
2	A_t	B_b and C_b
3	A_b	B_b and C_b
4	A_b	B_t and C_t

The signal used in this experiment was a Hanning-windowed sinusoidal tone burst. The duration d of the signal depends on the amount of cycles in the tone burst N and the central frequency f:

$$d = \frac{N}{f} \qquad (4.7)$$

The frequency bandwith of the tone burst is directly proportional to f/N (Wang and Yuan 2007). This means that a longer tone burst will give a smaller frequency bandwith, which is favourable because it reduces dispersion and prevents higher mode generation. However, a longer tone burst would inevitably reduce the usefulness of measurements to this experiment, because it increases

the likelihood of overlapping Lamb modes and boundary reflections. Given the distance between transmitter and receivers, a number of 5 cycles was considered to offer a good trade-off between overlapping and frequency bandwidth. Waveforms were created using a Matlab code that applied the Hanning window operation on a signal of user-selected frequency with a user selected number of cycles. These waveforms were uploaded to the waveform generator, which was set to generate waveforms at a sampling frequency of 250 MHz with a 20V peak-to-peak output.

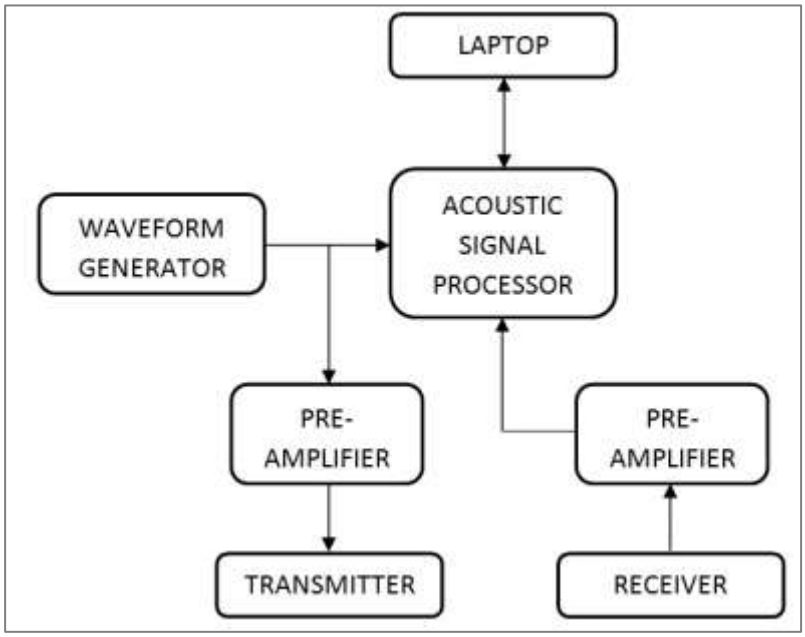

Figure 26 | Equipment setup.

A total of 9 central frequencies were used: 80, 100, 120, 140, 160, 180, 240, 260 and 280kHz. The transducers used have a good frequency response in those frequency ranges (Vallen 2012). For each of the transducer arrangements given in Table 7 the excitation frequency was set to each of the 9 frequencies subsequently, and the transducer output from location B and C as well as the waveform generator output was recorded. The settings of the acoustic signal processor for recording were:

- Transient recording with sampling rate 10MHz, maximum 8192 samples per set,
- Threshold value 30.1dB,
- 200 pre-trigger samples,
- Duration discrimination time 200μs,
- Rearm time 0.4ms.

It should be noted that the efficiency of wave generation depends on the properties of the bonding layer. When changing setup all transducers were removed and reattached without control over the bonding layer thickness. Therefore, the generated wave magnitude could not be compared between transducer setups. However, comparison was possible between different frequencies within each setup. This meant that a difference in efficiency between generation on the tool- and

bagside of the specimen could not be reliably determined, while the influence of frequency could be studied.

4.2.2 Data Collection and Processing

For the purpose of this experiment, the following features were extracted from the recorded signals. All features were extracted from the first wave peak to arrive, because this was expected to be the S_0 mode.

Time of Arrival (ToA) and WT magnitude at location B

The ToA of the first wavelet energy peak at location B on both tool- and bagside was required as starting point for ToF measurements between locations B and C. It is noted here that the ToA is differs from the ToF. The ToA is the local time at which the energy peak arrives at any single location, while the ToF is the time travelled between two locations. As such, the ToF is calculated from the ToA at two locations, as is reflected in equation (3.11). The WT magnitude at location B served as a measure of the wave generation efficiency and as a starting point for attenuation measurements between locations B and C.

ToA and WT magnitude at location C

The ToA of the first wavelet energy peak at location C was used to determine the ToF between locations B and C for both tool- and bagside, which was used in group velocity calculations. The magnitude of the WT at location C was used to calculate the attenuation between points B and C.

Recorded signals were processed using AGU-Vallen Wavelet R2014.0414.3 software, as described in section 3.5. The AGU-Vallen Wavelet allowed determining the time of occurrence of the WT peak at any chosen frequency. This was of great benefit to the calculation of group velocity for two reasons. First, it enabled repeatability of method for any desired frequency, thus giving a reliable basis for comparison between frequencies. Second, it ruled out the effects of attenuation and dispersion, as described in the introduction of this section. In addition, it lead to a better comparability to FE modelling results, since attenuation and dispersion were not accurately modelled.

Group velocity was calculated using equation (3.10) and attenuation using equation (3.13). Wave peak energy was calculated as the square of the WT peak magnitude (equation (3.12)) at the frequency under investigation. The amplitude in the time domain of recorded signals was stored for comparison between tool- and bagside of the sandwich specimen.

4.2.3 Results and Discussion

In general it should be noted that the amplitude of received signals at frequencies above 160kHz was very low. In some cases, the signal barely crossed the threshold value of 30.1dB. When calculating the ToF, it was therefore not certain that the same energy peak was measured at location B and C, because the energy peak that was measured at location B may have been

attenuated below the threshold value at location C. Results for frequencies above 160 kHz are therefore reported here with limited confidence.

The results of the group velocity dispersion curve verification experiments are given in Figure 27. The dots in this figure resemble the group velocity measured for signals generated and received on the toolside and bagside of the specimen. It shows that the theoretical group velocity dispersion curve of the S_0 mode closely follows the experimental results. It is apparent that the measured group velocity differs between the tool- and bagside of the specimen. An increase of group velocity was found at frequencies 160kHz on the bagside and 180kHz on both sides. The values found at those frequencies were near the group velocity of the S_0 mode in the skin composite laminate (see the dispersion curves in Figure 15). This indicated that the waves may have been contained in the skin, propagating as LLWs.

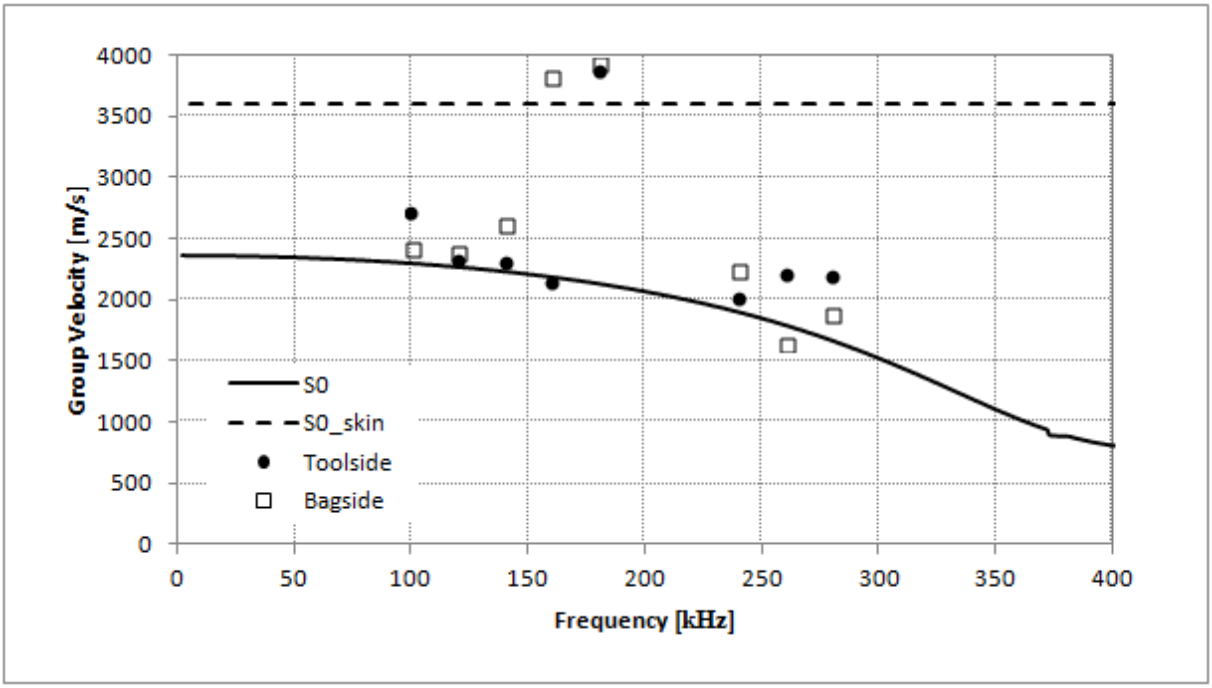

Figure 27 | Theoretical S_0 group velocity dispersion curves (lines) with experimental results (dots).

The energy of the first wave peak as a function of frequency is presented in Figure 28. Measurements show that the generated wave energy was highest at 100 and 120kHz, and was generally higher when the transmitter was placed on the bagside of the specimen. This may be explained by the fact that the bagside is rough and thus allows more energy to be transferred from the transmitter to the structure through friction. It should be noted, however, that the generator was bonded to the specimen without much control over the bonding quality. Further experiments would therefore be required to make a substantiated comparison of the efficiency of wave generation on the toolside and bagside of the DragonFly fuselage structure. It was concluded from these measurements that in the setup used, frequencies ranging between 100 and 140kHz would result in higher pulse energy and thus higher propagation distance.

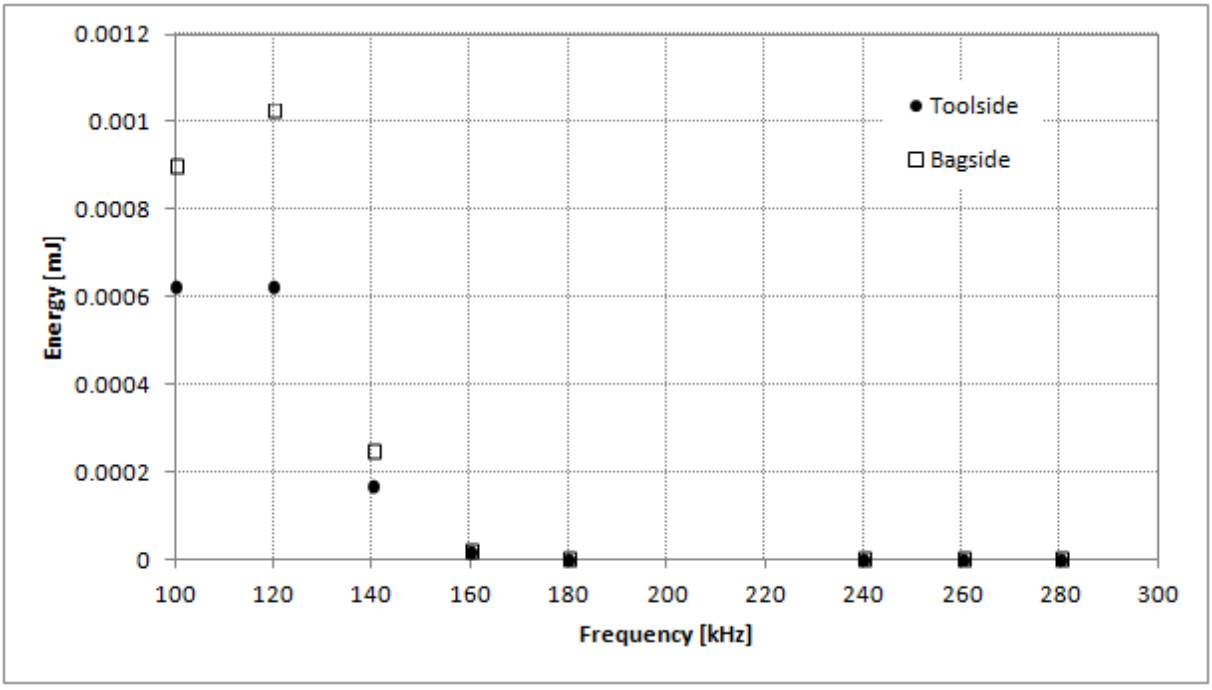

Figure 28 | Wave energy at location B of signals generated and received on the toolside and bagside.

The higher energies at 100 and 120kHz were also partly due to a lower attenuation at those frequencies, as can be seen from Figure 29. This figure shows the attenuation as percentage loss of energy of the first wave energy peak between location B and C. It is apparent that attenuation was generally higher on the bagside of the specimen.

From the results in Figure 28 and Figure 29 it was concluded that 120kHz was the best frequency to be used for SHM experiments. At this frequency, attenuation was relatively low, while the generated wave energy was high. Although attenuation at 100kHz is lower, 120kHz was favoured because it results in a more narrow Hanning windowed tone burst, thus reducing the risk of overlapping wave modes.

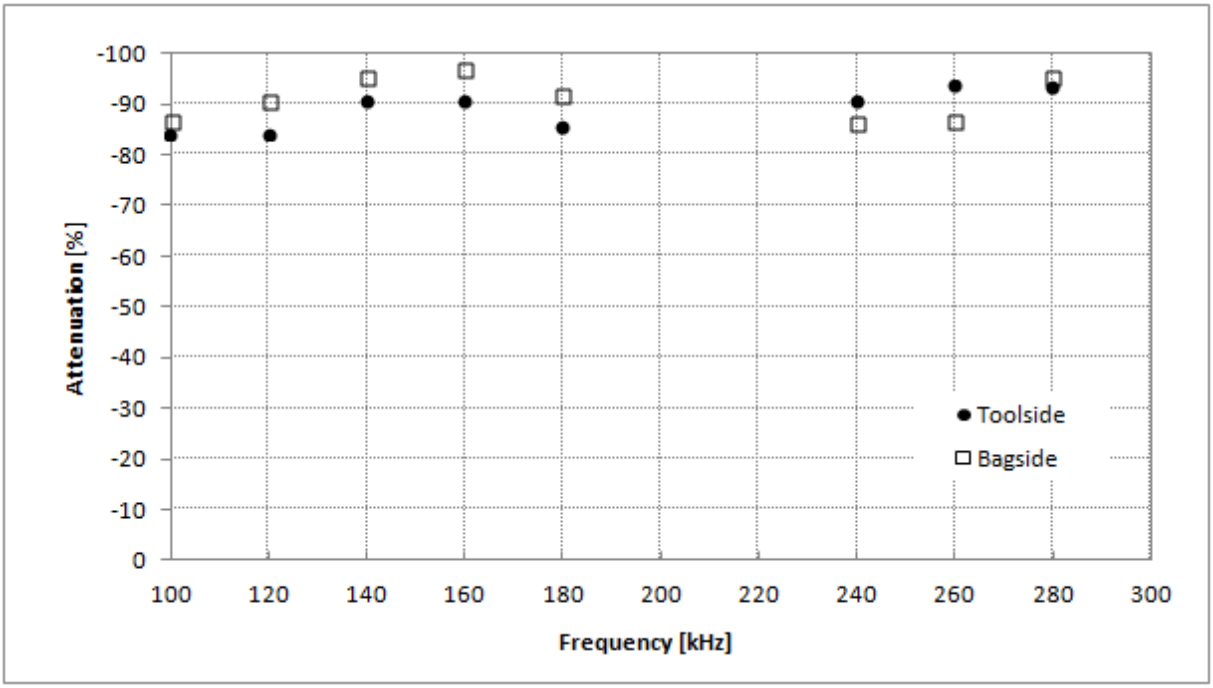

Figure 29 | Attenuation (percentage loss of energy) between location B and C on the tool- and bagside.

In an attempt to verify the impression from group velocity measurements that LLW propagation occurred at 160 and 180kHz, the transient amplitude of a signal transmitted with central frequency 160kHz and 120kHz and received at location B is plotted in Figure 30 and Figure 31 respectively. These figures show the received signal on either side of the specimen in an overlay plot. If the propagation mode was LLW, a phase shift was expected between the received signals on tool- and bagside. If the propagation mode was GLW, the signals were expected to overlap perfectly. Figure 31 shows that the latter was true at 120kHz central frequency, while Figure 30 shows a slight phase shift at 160kHz central frequency, but smaller than the expected 2 to 3µs. Hence, insufficient data was found to confirm the LLW propagation mode. Further experiments performed to obtain additional data to confirm this are described in section 4.4.

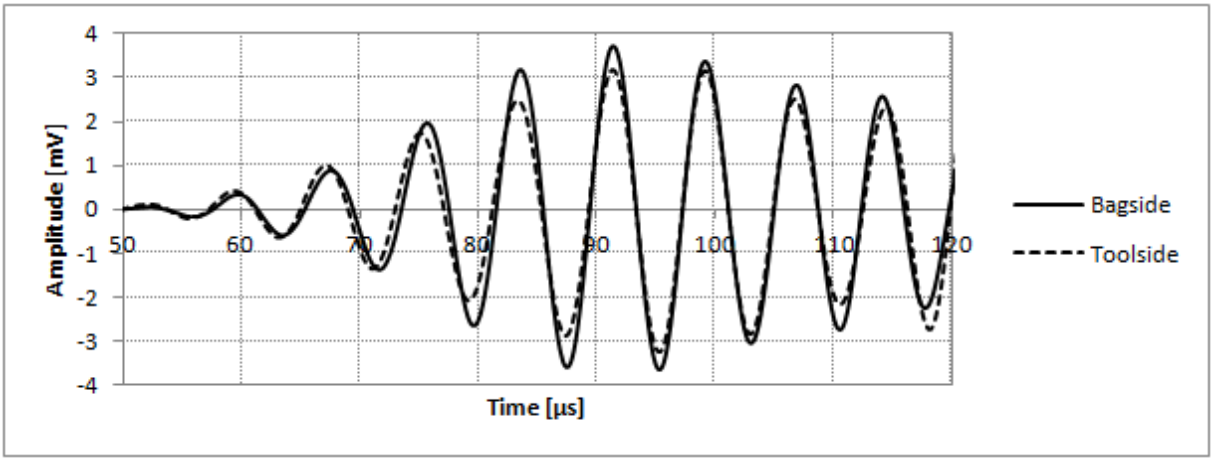

Figure 30 | Received signal (160kHz) at location B, transmitted on the bagside.

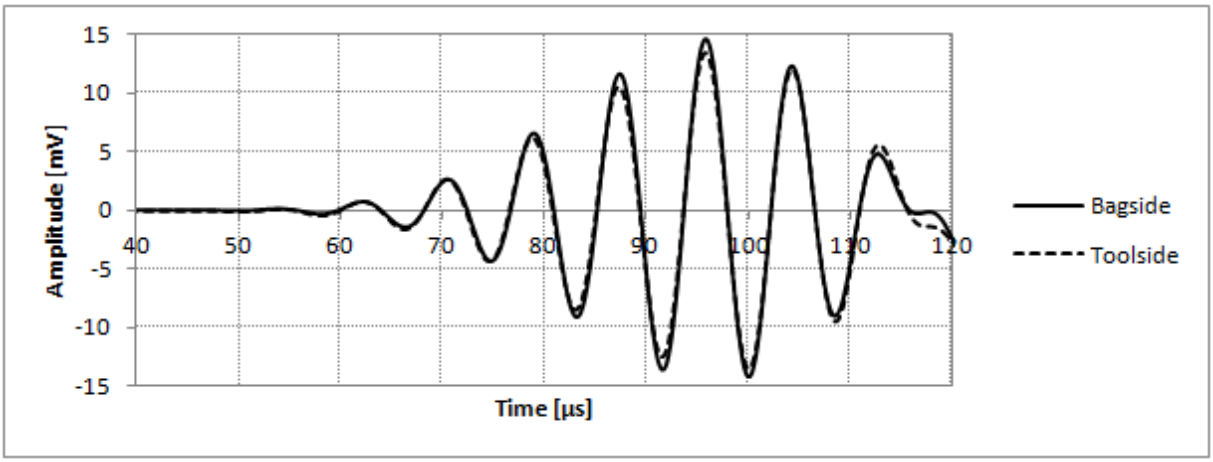

Figure 31 | Received signal (120kHz) at location B, transmitted on the bagside.

4.3 Impact Tests

A series of impact tests was conducted to verify the qualitative relationship between impact energy and damage diameter found in section 2.2.3. Impact tests were performed using test standard ASTM D 7136 (ASTM 2005) as a guideline. Deviations and simplifications were made where appropriate, since a full characterization of the DragonFly fuselage structure in terms of damage resistance was not required. Rather, the use of impact testing in the current study was to produce different damage sizes for SHM experiments as described in section 4.4.

4.3.1 Experimental Setup

Sandwich panel specimens were produced in a one-shot vacuum assisted resin transfer moulding process, a detailed logbook sheet is provided in Appendix VI. A drop tower equipped with a 37mm diameter hemispherical striker tip and impactor mass 1.25kg was used for the impact tests. The specimens were clamped between two aluminium plates on a fixture with a 150x150 mm opening (see Figure 32). This method of support ensured that the boundary conditions for each impact were identical. The drop height of the impactor H was calculated as follows:

$$H = \frac{E_p}{m_d g} \tag{4.8}$$

Where E_p is the desired potential energy of the impactor prior to the drop, m_d is the mass of the impactor for drop height calculation in kg and g the acceleration due to gravity, 9.81m/s^2.

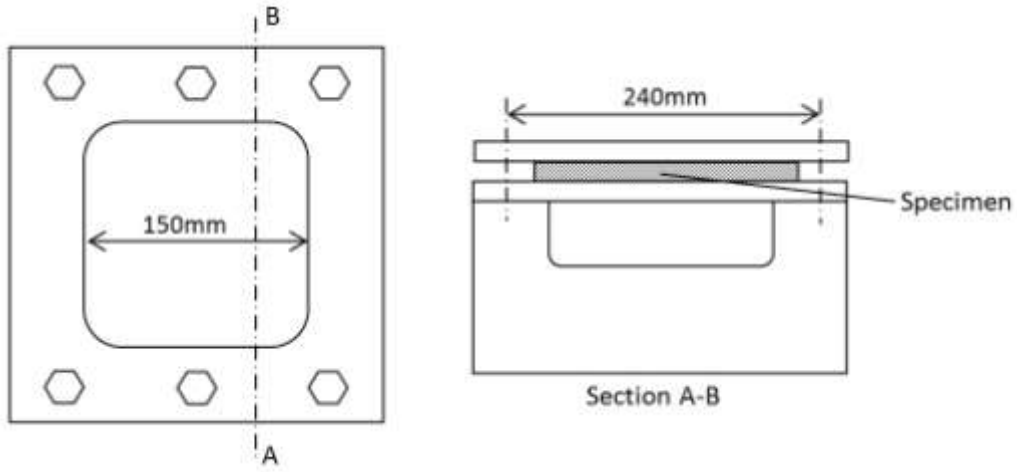

Figure 32 | Impact support fixture.

Directly after the initial impact had occurred, an aluminium plate was inserted between the fixture and impactor, to prevent additional impacts from occurring. This was done to make sure that damage modes were comparable between impacts. Any additional impacts that occurred despite this prevention method were reported. After impact, panels were subjected to C-scan with 1mm accuracy to determine the damage size.

Impact tests were conducted in two series. The first series was used to determine at which energy levels the second series should be conducted. The second series contained the specimens for SHM experiments. In the first series, a single specimen (Laminate ID 26022015SW1) was impacted at several locations. After the C-scan, the panel was cut through the impact locations to study the failure modes under an optical microscope.

In the second series, 3 specimens (Laminate ID 05032015SW2, 19032015SW3a and 19032015SW3b) were impacted individually at energy levels ranging from 0 to 10J (see Table 8), a range that was determined from the first series. Specimens were impacted at two locations iI and iII as indicated in Figure 33 and Table 8, thus making a total of 6 impacts. These specimens were used in the SHM experiments described in section 4.4.

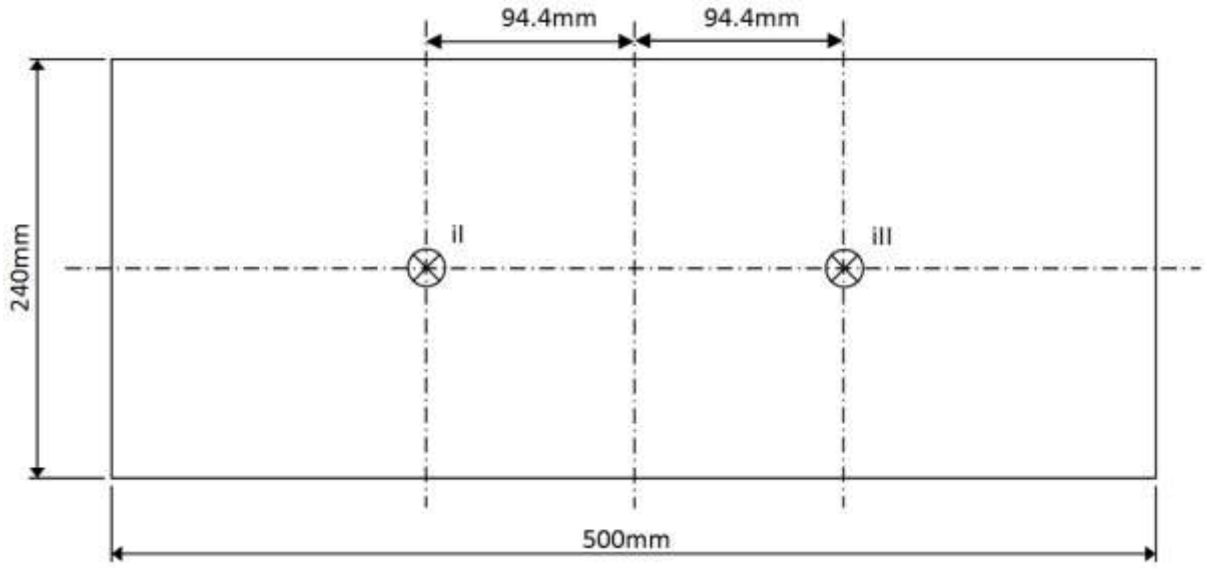

Figure 33 | Impact location definition.

Table 8 | Impact energies of the second series.

#	Specimen (location)	H [mm]	Ep [J]
1	05032015SW2 (iI)	206	2.53
2	19032015SW3a (iII)	348	4.28
3	19032015SW3b (iII)	499	6.13
4	19032015SW3b (iI)	648	7.96
5	05032015SW2 (iII)	651	8.00
6	19032015SW3a (iI)	805	9.89

4.3.2 Data Collection and Processing

The characteristic damage dimensions to be determined for each pre-defined impact energy level are defined in Figure 34. Only damage modes matrix cracks (a), delamination (b) and crushed core (c) were considered in this study, as was concluded in section 2.2.

Before impact, the actual drop height H was measured. After impact, the number of 'bounces' (i.e. the number of times the impactor hit the specimen after the initial impact event) was recorded. In the second impact series, dent depth δ_I was measured using a calliper.

The sample 26022015SW1 from the first impact series was subjected to a C-scan and subsequently cut through the impacted zones to study the cross section using a Zeiss SteREO Discovery.V8 optical microscope equipped with an AxioCam ERc5s camera. This was done to determine which failure mode corresponded to which area as identified in the C-scan images. C-scan data was processed using ALIS (Automated Laminate Inspection System) version 1.1 software, and the damage dimensions *a*, *b* and *c* were calculated as the average of the horizontal and vertical dimension of the damaged area.

The samples from the second impact series were subjected to a C-scan only, because they needed to remain intact for SHM experimentation. The same damage characteristic dimensions were recorded as for the first impact series. Identification of failure modes was based on similarity to specimen 26022015SW1.

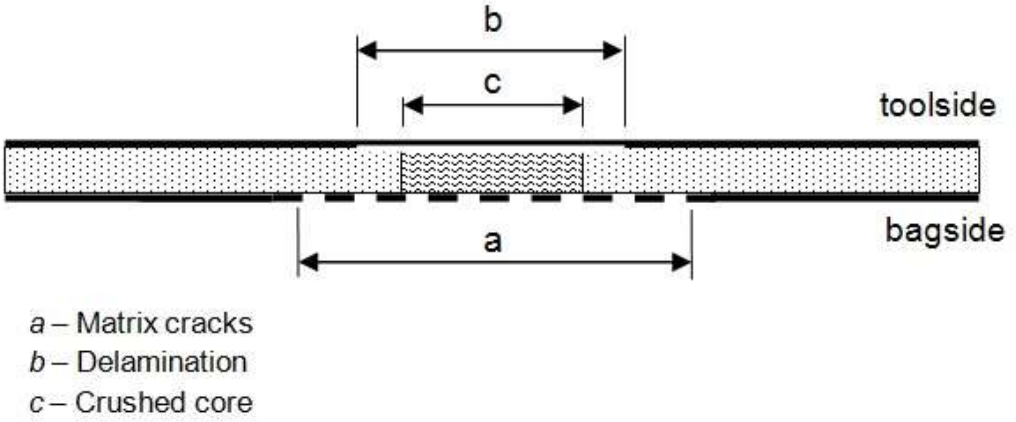

Figure 34 | Damage characteristic dimensions.

4.3.3 Results and Discussion

C-scan images of each specimen are provided in Appendix VII. A detailed C-scan image of specimen 26022015SW1 is given in Figure 35, indicating the area of damage that was reported for this specimen. Recorded data for this impact series are given in Table 9, which also includes a visual assessment of whether the damage could fall in the BVID range. Damage was considered BVID when the residual indentation was less than 0.5mm (as determined in section 2.2.1). Based on these results, an impact energy range of 0 to 10J was determined for the second impact series.

In the C-scan image, three damage zones were identified as indicated in Figure 35. Optical microscopy revealed core crushing in the zone that is coloured dark purple in this figure. The light purple coloured zone was found to be dominated by debonding between the core and the toolside skin. The dark blue zone appeared to contain some matrix cracking, predominantly in the interface matrix layer between bagside skin and the core. Some images from the optical microscope are reproduced in Appendix VII. However, due to the quality of the camera, not all damage features that were identified through the eyepiece can be properly seen in the images. For FE modelling, the characteristic damage dimensions as measured through C-scan were considered to correspond to the following failure modes:

a. matrix cracking in bagside skin
b. debonding between core and toolside skin
c. crushed core

Recorded data for the second impact series is given in Table 10. The three damage dimensions *a*, *b* and *c* from all impacts performed in the second series are plotted against impact energy in Figure 36. As can be seen, the damage dimensions of impact 5 are slightly off the trend. Since there was no apparent cause for this difference and no other reference impacts were available, this was attributed to inaccuracies in the experimental method and measurements, and not further investigated. For the purpose of SHM experimentation and FE modelling, this impact was not considered.

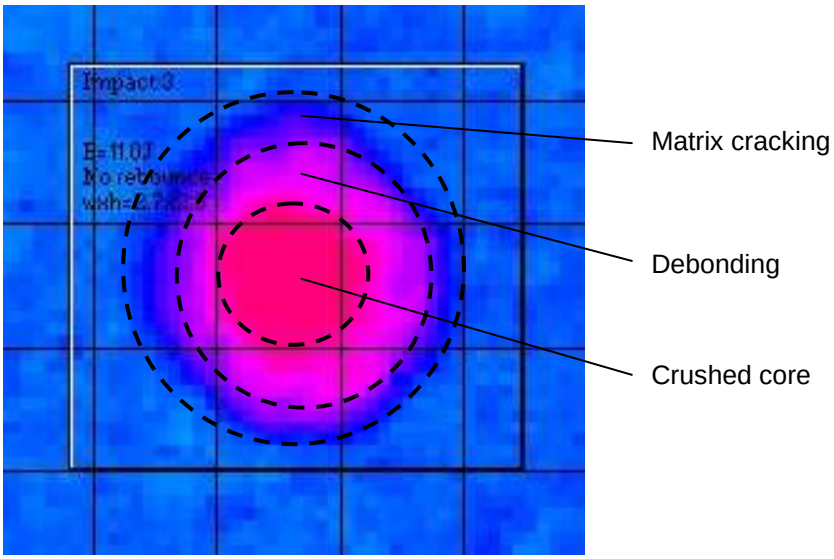

Figure 35 | Example of damage size measurement in C-scan data.

Table 9 | Impact results (first series).

#	H [mm]	Ep [J]	D [mm]	Bounces	BVID
1	615	7.56	28.5	4	no
2	770	9.46	26	0	yes
3	895	11.00	27.5	0	yes
4	743	9.13	19.5	1	yes

Table 10 | Impact results (second series).

#	H [mm]	E_p [J]	Matrix cracks [mm]	De-bonding [mm]	Crushed core [mm]	δI [mm]	Bounces
1	206	2.53	18.5	11.0	4.5	0.1	0
2	348	4.28	22.0	18.5	11.0	0.15	0
3	499	6.13	25.0	20.5	13.5	0.25	0
4	648	7.96	27.0	23.0	15.5	0.30	0
5	651	8.00	25.0	17.0	10.0	0.30	0
6	805	9.89	29.0	26.0	19.5	0.35	0

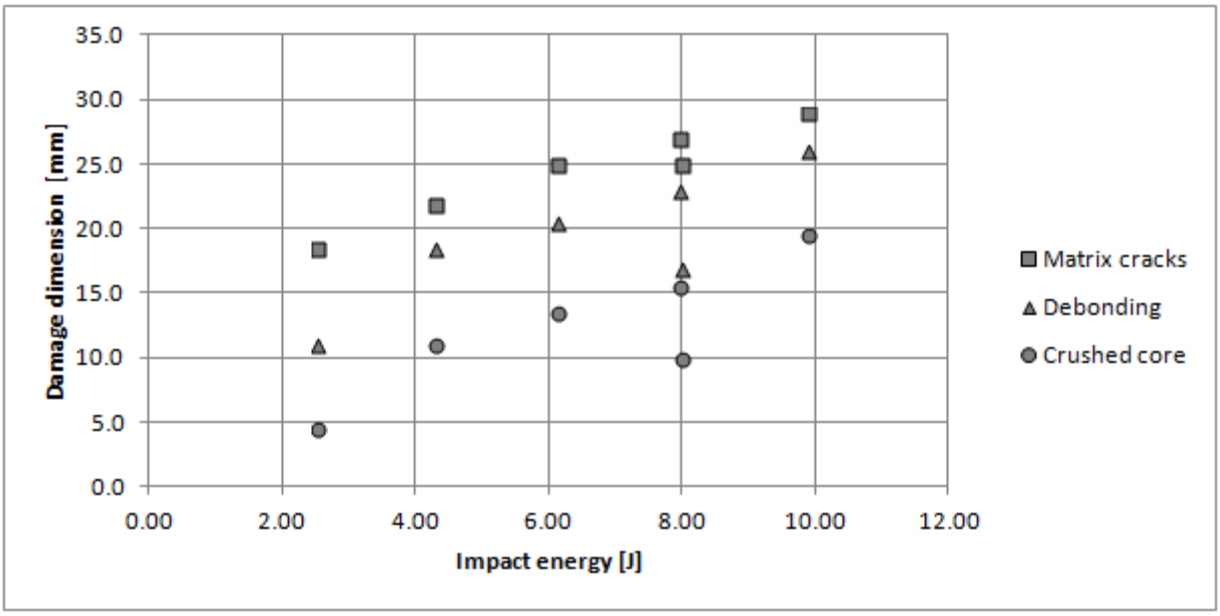

Figure 36 | Impact damage dimensions against impact energy.

4.4 SHM Experiments

This section is dedicated to the experiments that were conducted to verify the results from FE modelling and to show that active acoustic SHM can be used to detect actual (i.e. not simulated) impact damage in the DragonFly fuselage sandwich structure. Furthermore, these experiments served to verify the hypothesis developed in section 3.4, which stated that both the ToF and the through-transmitted magnitude would decrease under the presence of impact damage.

4.4.1 Hypotheses to be Verified

The aim of the current study was to verify the expected influence of barely visible impact damage on the ToF and magnitude of a through-transmitted guided wave, used in a pitch-catch configuration in the DragonFly fuselage structure. As was concluded from the experiments described in section 4.2, a central frequency 120kHz was considered to be the most appropriate choice for active acoustic SHM with GLWs in this structure.

It was hypothesized in section 3.4 that debonding as a damage mode would cause mode decomposition of a GLW in the damaged zone. The pulse would then propagate through the skins alone, and since the propagation velocity in the skins was higher than that in the sandwich the ToF would reduce. This reduction was expected to increase with increasing debonding size. Furthermore, crushed core was expected to hinder wave propagation through the damaged zone and thus increase attenuation, again to a larger extent for increasing damage size.

From the experiments discussed in section 4.2 insufficient confirmation were found that LLW propagation of the S_0 mode occurred at 160 kHz central frequencies. As was seen in section 3.3, the response of LLWs to the presence of impact damage is fundamentally different from that of GLWs. While impact damage was expected to increase attenuation of GLWs, it was expected to decrease attenuation of LLWs. This is due to the fact that debonding between skin and core

prevents leakage of the LLW energy into the core. To verify this experimentally, SHM experiments were executed at a frequency range from 100 to 160kHz. It was expected that an increase of through-transmitted energy would be seen at 160kHz, as opposed to the other frequencies.

4.4.2 Experimental Setup

Sandwich panel specimens were produced in a one-shot vacuum assisted resin transfer moulding process, a detailed logbook sheet is provided in Appendix VI. The experimental setup was mostly identical to that described in section 4.2.1. Only deviations from this setup are described here.
The transducer arrangement is shown schematically in Figure 37. The distance between transmitter and receiver was chosen such that the first reflections from the three nearest boundaries arrive at the transmitter at roughly the same time. This simplified the received signals considerably and improved the distinction between the direct signal and boundary reflections.

All transducers were placed on the bagside skin to mimic the situation as foreseen for the DragonFly fuselage. The transmitter and receivers were bonded to the structure using Dow Corning® 734 silicon adhesive. Then, a baseline measurement was performed at 100, 110, 120, 140, 150 and 160kHz and subsequently the sample was subjected to impacts as described in section 4.3. This way, it was ensured that the properties of the transducer-bonded interface were identical before and after impact. After the impacts were made, a second measurement was performed at 100, 110, 120, 140, 150 and 160kHz.

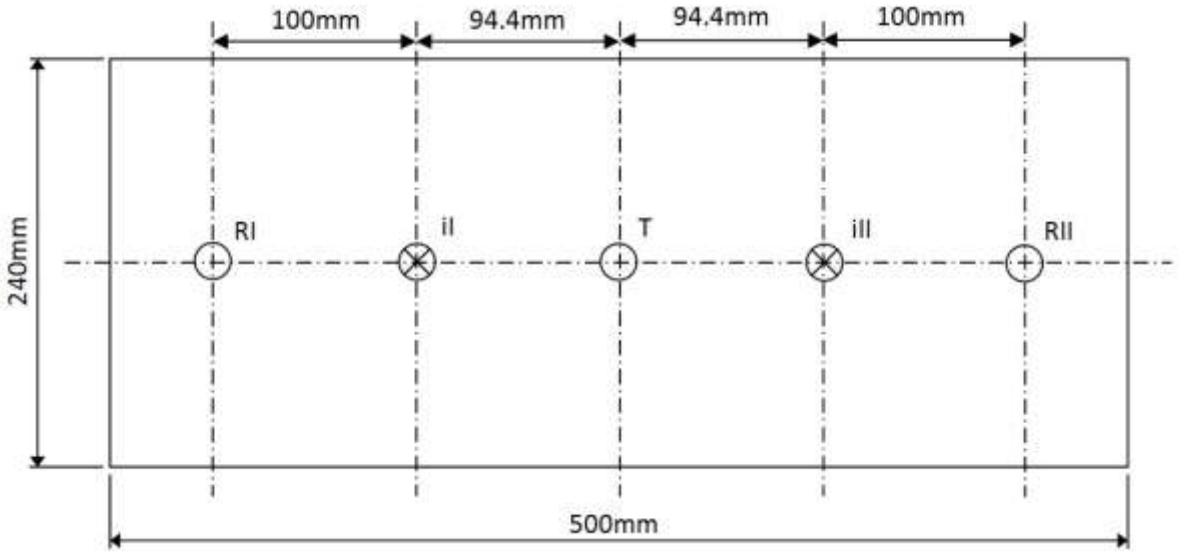

Figure 37 | Transducer arrangement for SHM experiments with receivers RI and RII, transmitter T and impact locations iI and iII.

4.4.3 Data Collection and Processing

Recorded signals were processed in a fashion similar to that described in sections 3.5 and 4.2.2. The time of transmission as well as the Time of Arrival (ToA) and WT magnitude */WT/* at RI and RII were measured before and after impacting the specimens. The time of transmission was measured from the waveform generator output and the time required for the tone burst to be generated in

the specimen was not known. As a result, the Time of Flight (ToF) could not be readily determined from the measurements. However, the difference in ToA before and after impacting the specimen was assumed to be equal to the difference in ToF, since the time required for the tone burst to be generated was expected to be unchanged after impacting.

4.4.4 Results and Discussion

The ToA and */WT/* at RI and RII for the undamaged and damaged specimens measured at 120kHz central frequency is reported in Table 11. From this data, the absolute difference in ToA (Figure 38) and the relative difference in through-transmitted energy (Figure 39) were calculated and plotted as a function of debonding size *b* and crushed core size *c* respectively. For these calculations, the measurements on the undamaged specimens were used as baseline. It should be noted that the influence of damage parameters *a*, *b* and *c* could not be separated in these experiments, and the choice of damage parameter for the figures in this section is rather arbitrary and considered to be representative of the more general notion of damage size.

Table 11 | SHM experimental results (f=120kHz).

#	b [mm]	ToA [μs]		|WT| [mV]	
		Undamaged	Damaged	Undamaged	Damaged
1	11.0	107.40	106.93	0.0177	0.0163
2	18.5	104.95	104.50	0.0149	0.0136
3	20.5	104.05	103.20	0.0098	0.0089
4	23.0	104.65	102.85	0.0115	0.0102
6	26.0	102.90	101.20	0.0101	0.0088

Figure 38 and Figure 39 suggest a correlation between damage size and ToA and through-transmitted energy at a central frequency of 120kHz, where both were decreased under the presence of damage and increasingly so in a linear fashion with increasing damage size. As was expected, the energy of the received signal was reduced under the presence of damage. This effect may be attributed to the crushed core, which hinders the propagation of the GLW. As was also expected, the propagation velocity of the GLW generally increased under the presence of damage, which was attributed to the occurrence of mode decomposition in the damaged zone due to debonding. The amount of increase appeared to be dependent on damage size in a non-linear fashion. This could be due to interference effects when the decomposed modes reach the end of the damaged zone, as was seen in previous studies (see section 3.3.1). Further experiments would be required to confirm this hypothesis.

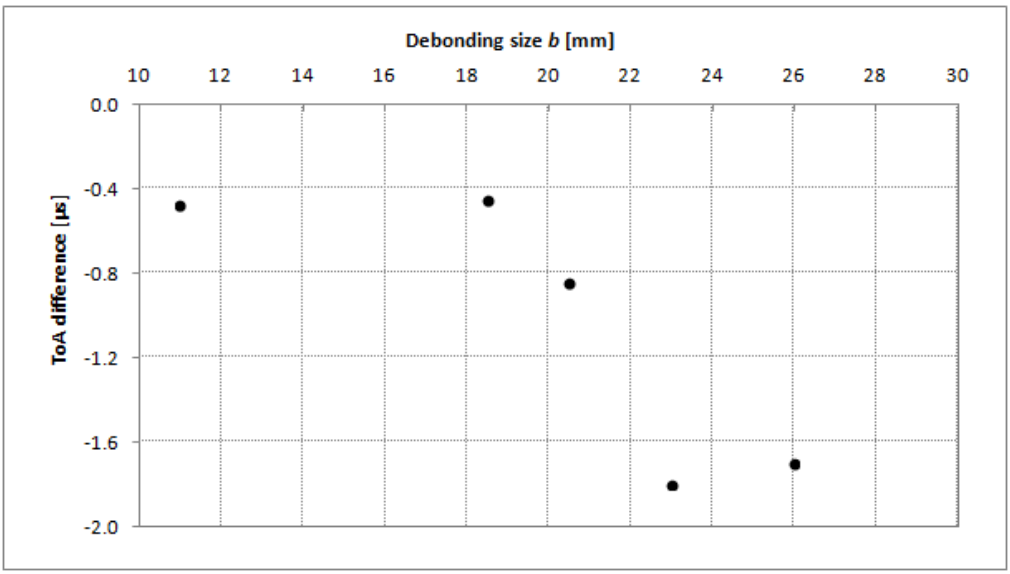

Figure 38 | Absolute difference in ToA at receiver against debonding size (f=120kHz).

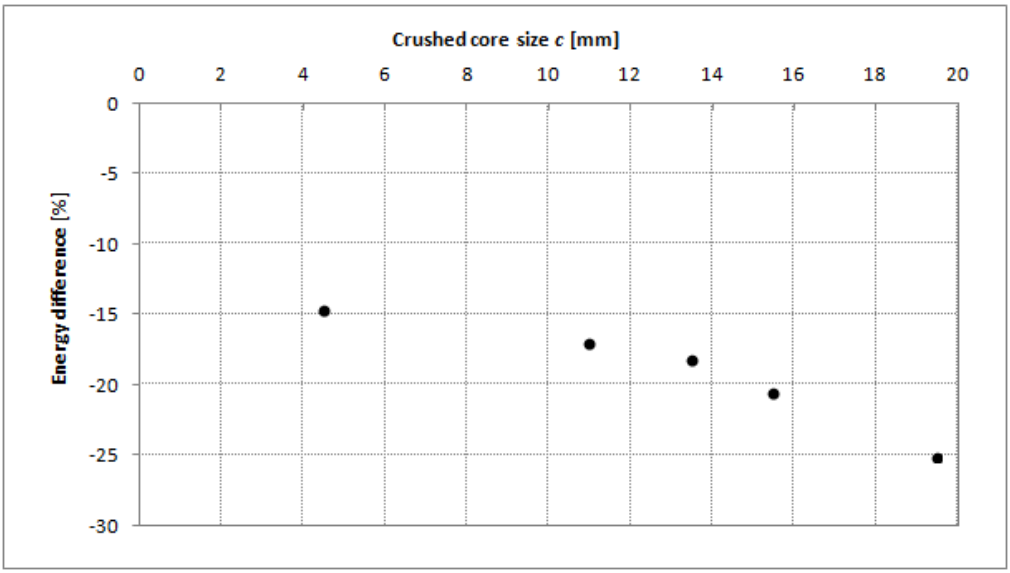

Figure 39 | Relative difference in through-transmitted energy against crushed core size (f=120kHz).

To further confirm the leaky propagation of lamb waves at a central frequency of 160kHz, the through-transmitted energy difference compared to the undamaged baseline is plotted against central frequency for different damage sizes in Figure 40. A negative percentage energy difference indicates that the through-transmitted energy is lower under the presence of impact damage when compared to the undamaged baseline. Figure 40 shows a sudden change to a positive energy difference, indicating that the through-transmitted energy at 160kHz is higher under the presence of impact damage when compared to the undamaged baseline. This confirms LLW propagation, since debonding was expected to decrease attenuation of an LLW.

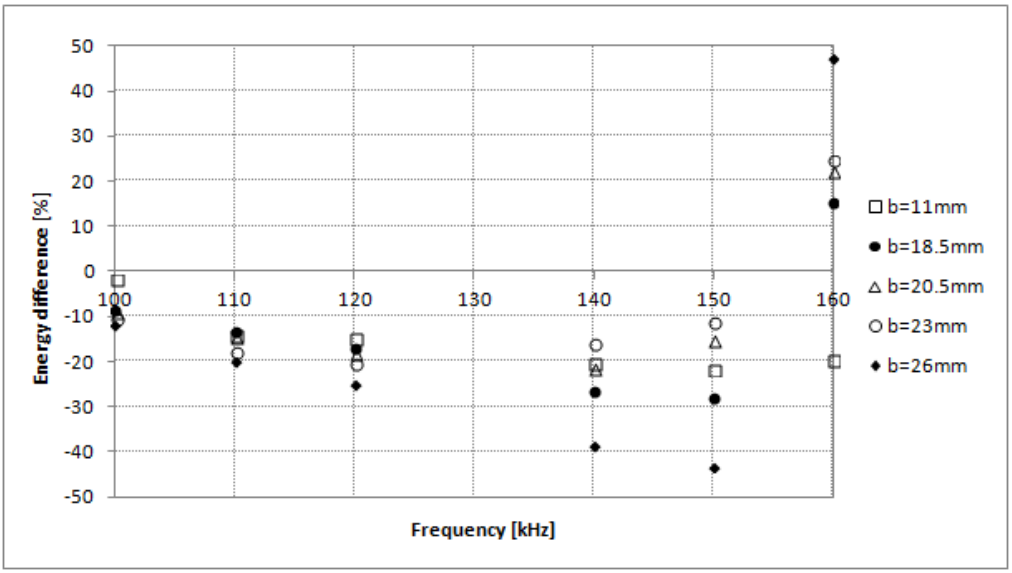

Figure 40 | Relative difference in through-transmitted energy as a function of frequency for different debonding sizes *b*.

One data point for *b*=11mm deviates from this expectation and shows a negative energy difference even at 160kHz. To further investigate this point, the energy difference at 160kHz central frequency is plotted against damage size in Figure 41. It can be seen that the energy difference increase is nearly linear with damage size from a negative value at *b*=11mm. This may be explained using the diffraction limit. The group velocity of the LLW at 160kHz was found to be 3800m/s (see Figure 27), which corresponded to a wavelength of roughly 24mm. The diffraction limit then predicts that this mode is insensitive to damage sizes below 12mm. However, the energy difference at *b*=11mm is non-zero, and thus some sensitivity is present. Possibly, the LLW mode is insensitive to debonding below the diffraction limit, but is still affected by matrix cracks. After all, the size *a* of the area containing matrix cracks was estimated to be 18.5mm (see Table 10).

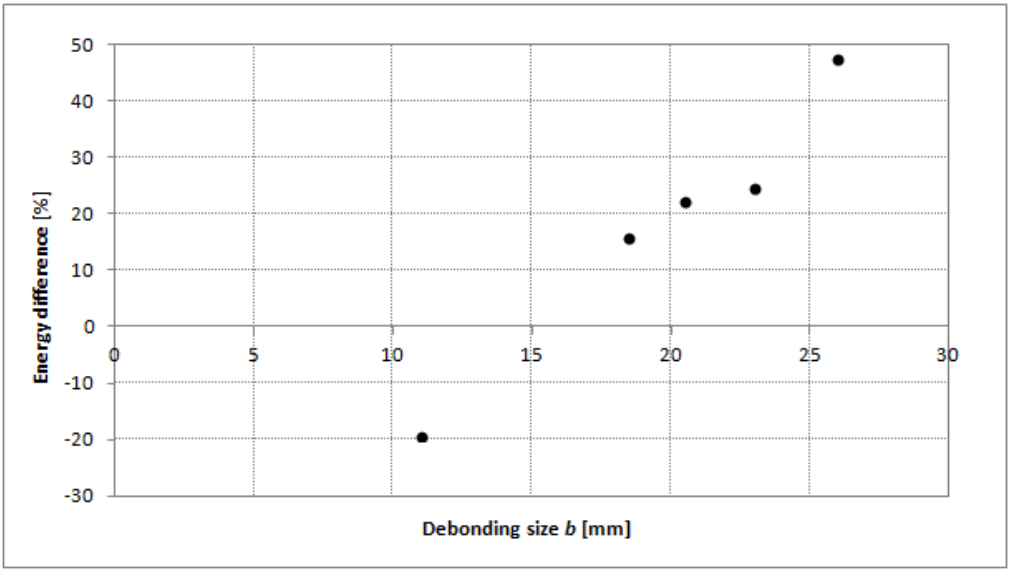

Figure 41 | Relative difference in through-transmitted energy at 160kHz central frequency as a function of debonding size *b*.

5 Modelling

In this section, the development of an FE model and analysis is discussed. The purpose of this analysis was to model the response of the sandwich composite structure to acoustic signals under the presence of impact damage. The modelling approach is first described in detail for a sandwich panel without damage, followed by a short review on convergence. Then, the modelling of damage and the post processing of the simulation output is treated. Finally, the results of the simulations are presented and compared to experimental results.

5.1 FE Model

The finite element model for prediction of experimental results was created in Abaqus/CAE®. A total of six models were used: one undamaged baseline and five models with different damage sizes representing the five specimens used in experiments (see Table 11). Three-dimensional models were used in order to study the interaction of guided waves with three-dimensional damage modes. This section provides an overview of the modelling approach for the undamaged baseline, the introduction of damage is discussed in section 5.3.

5.1.1 Sandwich Panel

To model the entire sandwich panel as an exact duplicate of the actual panel would require high calculation costs and very detailed modelling. Therefore, assumptions were made in order to reduce the calculation time and improve model simplicity.

The first simplification was that the panel could be accurately modelled by assuming the panel to be regular, meaning that the mechanical properties and thicknesses of its constituents are equal for any parallel through thickness cross section. Only one quarter of the panel needed to be modelled then, and symmetry planes were defined to take into account the entire area of the panel (see Figure 42).

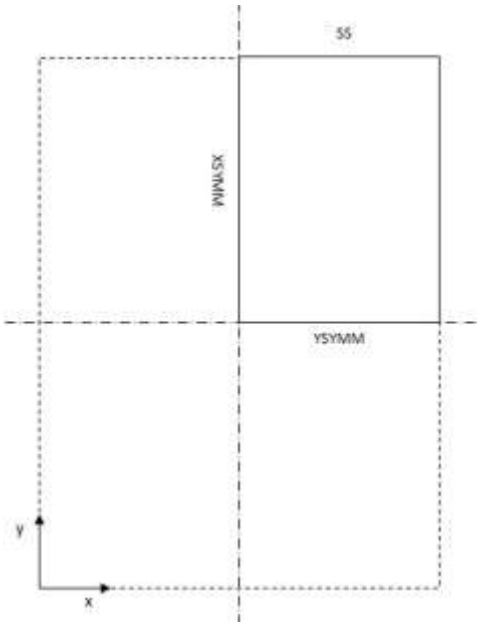

Figure 42 | Boundary condition definition.

A second simplification was the reduction of the sandwich construction to a skin and core model, i.e. the bonding layer between skin and core was not modelled. In reality, the cavities in the porous core were filled with resin, thus creating a matrix/core composite layer between skin and core. Because the pores were small and the panel was produced in a one-shot technique (i.e. no material is added for bonding), this layer was expected to be of negligible influence to acoustic wave propagation.

Further simplifications included approximation of the core as an isotropic material; identical tool- and bag-side skins; assumption of perfect bonding between skin and core; assumption of uniform density distribution in the skin; assumption of perfect contact between skin and transducers; and assumption of linear elastic material behaviour. It should be noted that due to the modelling of the constituent materials as linearly elastic, damping was not accounted for in the model. Hence, the numerical results did not provide any information on attenuation due to viscoelastic behaviour (Osmont, Devillers et al. (2001), Castaings and Hosten (2003)). This means that the model did not give a representative output for signal magnitude and thus through-transmitted energy. The relative influence of impact damage on through-transmitted energy could, however, still be modelled.

The core was modelled as a three dimensional deformable isotropic solid. A solid, homogeneous section was assigned with isotropic material as outlined in Table 12. The thickness of the core was set to $2.0 \cdot 10^{-3}$m, where the standard unit of distance in the model was taken as meters.

Continuous, three-dimensional brick elements were used with 8 nodes and reduced integration (element type C3D8R) with 6 degrees of freedom. The element size is presented in section 5.1.4.

Skins were modelled as three-dimensional deformable planar shells. A continuum shell composite section was assigned with three thickness integration points and Simpson thickness integration rule. The thickness of the section was set to $0.17 \cdot 10^{-3}$m. The material behaviour was defined in engineering constants as given in Table 12, which were determined in section 4.1.
For meshing, four-node shell elements with reduced integration (element type S4R) with 6 degrees of freedom were used. The element size was made equal to that of the core elements, to make sure the nodes in the skin coincided with the nodes in the core.

Table 12 | Core and skin engineering constants.

Core			Skin		
E	$160 \cdot 10^6$	Pa	E_1	$23.5 \cdot 10^9$	Pa
v	0.38		E_2	$23.5 \cdot 10^9$	Pa
ρ	106.6	kg/m^3	E_3	$7.9 \cdot 10^9$	Pa
			v_{12}	0.13	
			v_{13}	0.32	
			v_{23}	0.32	
			G_{12}	$3.8 \cdot 10^9$	Pa
			G_{13}	$3.0 \cdot 10^9$	Pa
			G_{23}	$3.0 \cdot 10^9$	Pa
			ρ	1852	kg/m^3

5.1.2 PIEZOELECTRIC TRANSDUCERS

Abaqus/CAE® offers the possibility to model the piezoelectric behaviour of materials. Thus, the transducers could be modelled by creating their geometry and assigning the material characteristics as specified by the piezoelectric material supplier (Boon 2014). The benefit of modelling the transducers was that the output signal could be directly compared to experimental results. Alternative modelling approaches include the assignment of displacements or forces and/or moments to the transmitter contact area nodes and analysing the stresses and displacements at the receiver area.

Piezoelectric transducers were modelled as 3D deformable solids. Material orientation was defined and a section was assigned with material characteristics as given in Table 13. The piezoelectric parts were meshed with 8-node linear piezoelectric brick (C3D8E) elements of characteristic size equal to that of the skin and core elements. Element size optimization is discussed in section 5.2.

Table 13 | Piezoelectric material properties.

Density	ρ	7850 kg/m^3
Electrical permittivity	$\varepsilon_{11}{}^T$ $\varepsilon_{22}{}^T$ $\varepsilon_{33}{}^T$	$1.72 \cdot 10^{-8}$ F/m $1.72 \cdot 10^{-8}$ F/m $1.68 \cdot 10^{-8}$ F/m
Charge constant strain coefficient matrix	d	$\begin{bmatrix} 0 & 0 & 0 & 0 & 669 & 0 \\ 0 & 0 & 0 & 669 & 0 & 0 \\ -208 & -208 & 443 & 0 & 0 & 0 \end{bmatrix} \cdot 10^{-12} \left[C/N \right]$
Elastic stiffness matrix	S^D	$\begin{bmatrix} 13.2 & 8.76 & 7.34 & 0 & 0 & 0 \\ 8.76 & 13.2 & 7.34 & 0 & 0 & 0 \\ 7.34 & 7.34 & 16.2 & 0 & 0 & 0 \\ 0 & 0 & 0 & 4.37 & 0 & 0 \\ 0 & 0 & 0 & 0 & 4.37 & 0 \\ 0 & 0 & 0 & 0 & 0 & 2.24 \end{bmatrix} \cdot 10^{10} \left[N/m^2 \right]$

5.1.3 ASSEMBLY

Since perfect bonding was assumed, skin-core bonding could be simulated by applying tie constraints. The interaction between skin and piezoelectric transducers was also defined through tie constraints. Symmetry boundary conditions were enforced on the mirror planes as indicated in Figure 42. Simply supported boundary conditions were defined on one short edge as indicated in Figure 42 to simulate the specimen support. To simulate grounding of the piezoelectric transducers, a uniform electrical potential boundary condition of magnitude 0 was assigned to the surface connected to the skin. An example of the assembly is given in Figure 43.

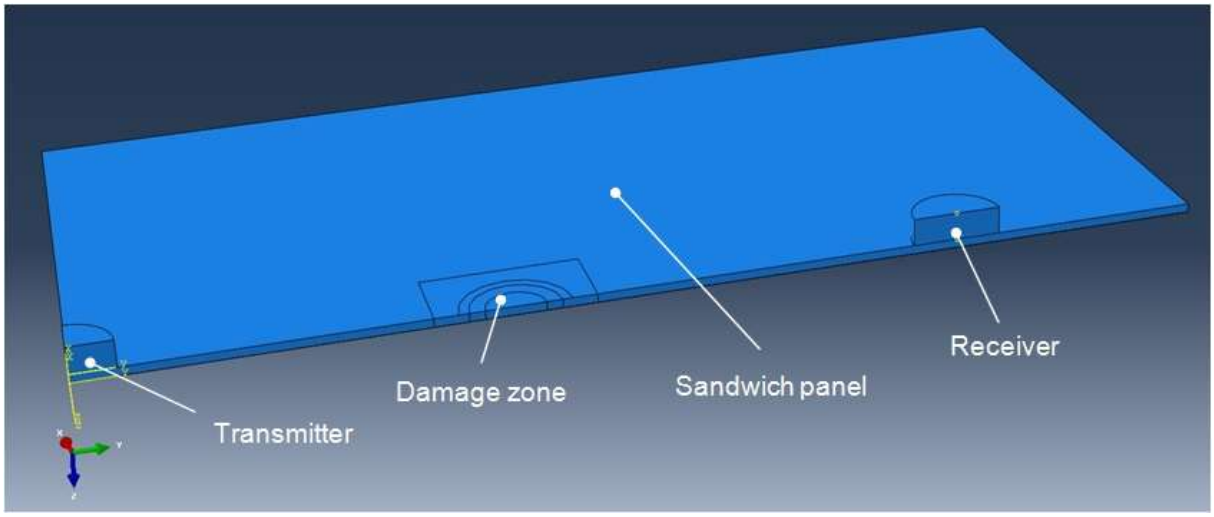

Figure 43 | Assembly of a damaged sandwich panel model.

5.1.4 INPUT AND OUTPUT

An input signal was defined for the actuator as an electrical potential boundary condition with magnitude 20 and amplitude a 120kHz, 5-cycle Hanning windowed pulse which was generated in Matlab® (see Figure 44 for a plot of the signal). The time step of this pulse was chosen to coincide with the increment size of the analysis, e.g. $1 \cdot 10^{-7}$ (see also section 5.2), and the signal contains a total of 417 data points. Thus, the duration of the pulse was 41.6μs. The duration of the simulation was determined by setting the number of iterations to 1200, which gives a duration of 120μs. This was sufficient to capture the first energy peak to arrive at the receiver (the S_0 mode), without using unnecessary simulation time

History output requests were defined for the electrical potential (EPOT) on the central node of the top surfaces of both transmitter and receiver. The central nodes were chosen because these were considered to be most representative of the average electrical potential as generated on the top surface of the actual piezoelectric transducers used in the experimental work.

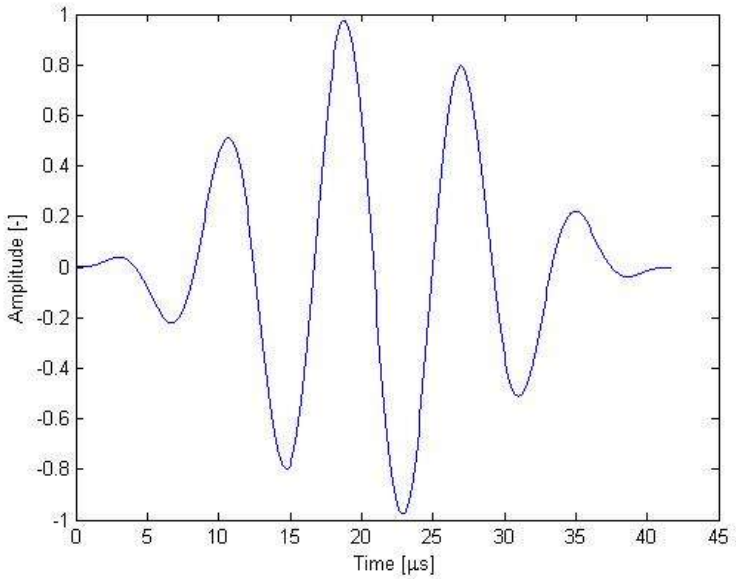

Figure 44 | 120kHz, 5 cycle Hanning windowed input signal.

5.2 Convergence

In the FE modelling of transient acoustic signals in plate like structures, the element size is often chosen such that the model contains at least 10 nodes per wavelength (Song, Huang et al. (2009), Mustapha and Ye (2014)). As the phase velocity of the S_0 mode at 120kHz was expected to be roughly 2350m/s (based on the dispersion curves in Figure 17), the corresponding wavelength was estimated to be $19.6 \cdot 10^{-3}$m. It followed that an element size of approximately $2.0 \cdot 10^{-3}$m would give sufficient accuracy. A brief convergence study was performed to verify this assumption, relating relative element size to ToF of the received signal.

To determine the convergence of the ToF when element size was decreased, six simulations of the undamaged sandwich panel model were ran with element size decreasing from $2.4 \cdot 10^{-3}$m to $1.5 \cdot 10^{-3}$m. After element size $1.5 \cdot 10^{-3}$m the convergence study was terminated as the ToF stabilized. The error in ToF was calculated from:

$$r_{ToF} = \frac{ToF_{FE} - ToF_{\exp}}{ToF_{\exp}} \cdot 100\% \qquad (5.1)$$

Where ToF_{exp} is the value for the ToF of a 120kHz pulse as was found experimentally (i.e. 83.42μs) and ToF_{FE} was calculated in post processing as described in section 5.4. Figure 45 and Table 14 show the results of the convergence study. From this, it was concluded that an element size of $1.8 \cdot 10^{-3}$m should be used to achieve the highest accuracy.

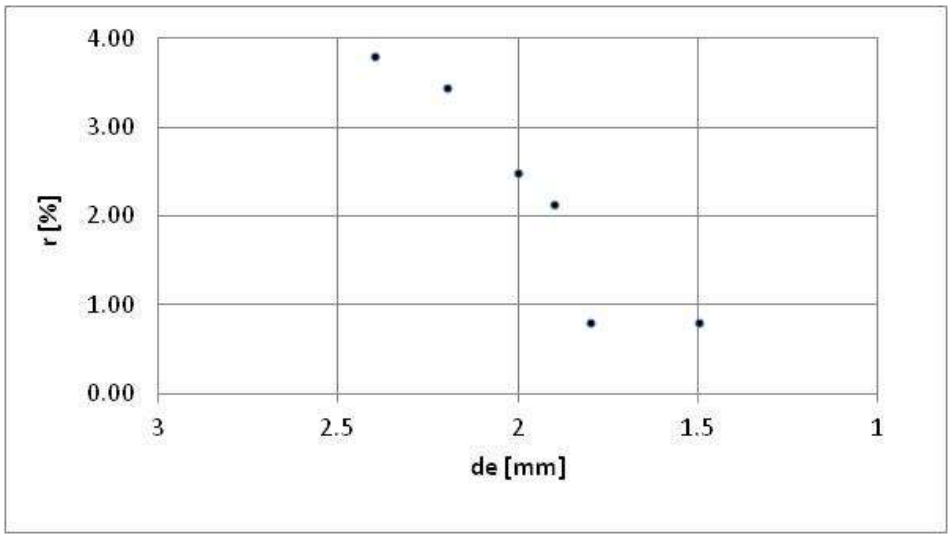

Figure 45 | Error in ToF against element size *de*.

Table 14 | Element size convergence results.

de [mm]	ToF [μs]	r [%]
1.5	84.10	0.82
1.8	84.10	0.82
1.9	85.20	2.13
2.0	85.50	2.49
2.2	86.30	3.45
2.4	86.60	3.81

A second parameter that influenced the output of the model is the time step size. Boon (2014) used a time step of 0.1μs for a 150kHz input signal. To determine convergence of the ToF under the influence of step size, five simulations were ran with time step decreasing from 0.4 to 0.07μs, while element size was kept constant at $1.8 \cdot 10^{-3}$m. Again, the ToF was calculated and compared to ToF_{exp} using equation (5.1). The results of this convergence study are given in Figure 46 and Table 15. Based on these results, a time step of 0.1μs was applied.

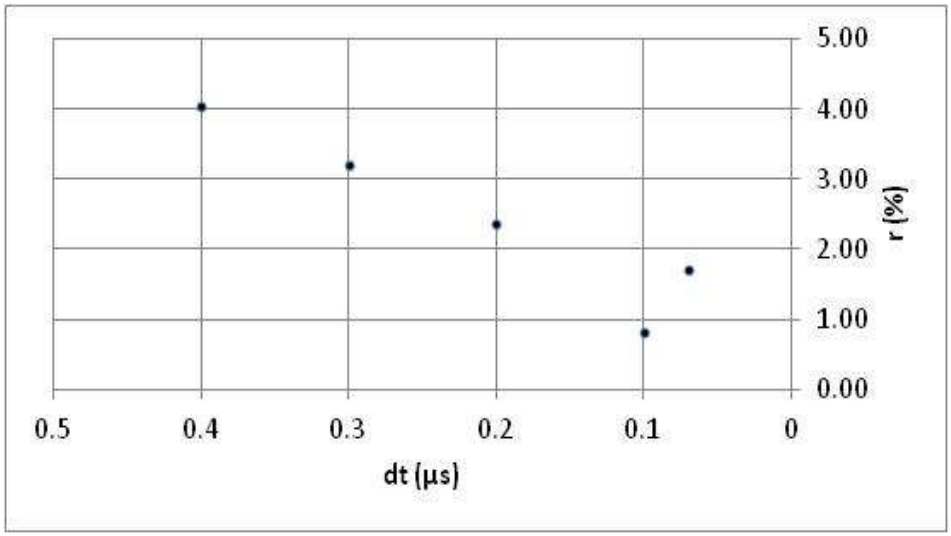

Figure 46 | Error in ToF against time step size.

Table 15 | Time step convergence results.

dt [μs]	ToF [μs]	r [%]
0.07	84.84	1.70
0.1	84.10	0.82
0.2	85.40	2.37
0.3	86.10	3.21
0.4	86.80	4.05

5.3 Damage

Impact damage was simulated based on the damage characteristic dimensions as determined from C-scan images and microscopy (see section 4.3). The characteristic dimensions are identified in Table 16 and Figure 47. To model the damage, semi-circular sections were created in the skins and core: one in the bagside skin with diameter *a*; one in the toolside skin with diameter *b*; and two in the core with diameter *b* and *c* respectively. These dimensions were chosen to correspond to the dimensions found experimentally (see Table 10). In all parts, the semi-circular sections were enveloped by a rectangular section for meshing purposes.

One of the main functions of the matrix is to stabilize the fibres in compression. Thus, matrix cracking was modelled as loss of this function by removing the ability of the material to carry compressive stress. This was done by defining a damaged GFRP material with the elastic properties option 'no compression' enabled and the remaining properties equal to those of the

undamaged GFRP material. This material was assigned to the semi-circular section with radius *a* in the bagside skin.

Debonding between layers can be simulated with a contact constraint (Gao, Ali et al. 2010) or by locally removing the tie constraint (Mustapha, Ye et al. 2011). In the latter case, however, the model would allow skin and core nodes to overlap, which was impossible in the experiments and would thus lead to incorrect boundary conditions. To avoid this, three-dimensional spring elements (SPRINGA or SPRING2) can be introduced between untied skin and core nodes with zero stiffness in tension and large stiffness in compression (Burlayenko and Sadowski 2009). However, Abaqus/CAE® offers the possibility to define surface-to-surface contact interactions. In the current model, contact constraints were employed as follows. A mechanical interaction property was defined with frictionless tangential behaviour and hard contact normal behaviour, default constraint enforcement method and allowing separation after contact. Surface-to-surface contact interaction was then defined between the core and the toolside skin for the semi-circular sections with diameter *b*.

Core damage as a result of impact can be modelled by locally reducing the material elastic properties. Shipsha, Hallstrom et al. (2003) found that the elastic modulus of a crushed foam core was roughly halved in the direction perpendicular to the direction of crushing, while it was diminished to roughly 3% in the crushing direction. Their tests also showed that the shear modulus in the plane parallel to the crushing direction was reduced to roughly 20%, which confirmed earlier findings by Thwaites and Clark (1995). Hence, a damaged core material was defined with modified properties as given in Table 17. This material was assigned to the semi-circular section in the core with radius *c*. Since this material was not isotropic, an orientation was assigned to the section.

Table 16 | Damage characteristic dimensions.

dimension [mm]	description	Location	Modelled damage
a	Matrix cracks in skin laminate	Bagside skin	No compression
b	Debonding between skin and core	Toolside skin	Interaction definition
c	Crushed core	Core	Modified engineering constants

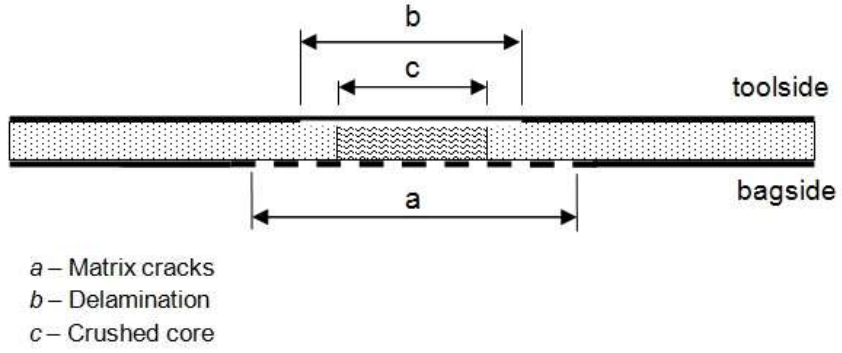

Figure 47 | Damage characteristic dimensions.

Table 17 | Modified core engineering constants.

	E1 (MPa)	E2 (MPa)	E3 (MPa)	G12 (MPa)	G13 (MPa)	G23 (MPa)	v12	v13	v23
Undamaged	160	160	160	50	50	50	0.38	0.38	0.38
Damaged	80	80	5	25	10	10	0.38	0.38	0.38

5.4 Post Processing

A typical output from the FE model is given in Figure 48, showing the S_0 mode (the first waveform to arrive at the receiver). To come to a comparison to experimental results, this output was post-processed as follows. First, the Abaqus© output data was converted to the Vallen© .tra format using the Vallen© Wave Importer software. Then, the wavelet transform was performed using the Vallen© Wavelet software. The result is shown in Figure 49. From the wavelet transform, the time of transmission and arrival were derived as well as the maximum energy of the signal at the central frequency of 120kHz, as described in section 3.5.

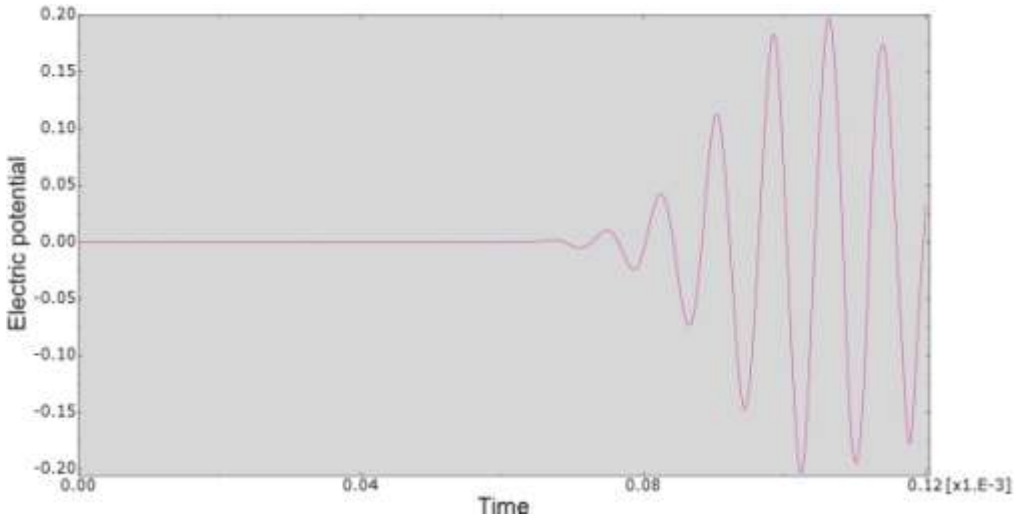

Figure 48 | FE model electrical potential at receiver central node, input signal 120kHz.

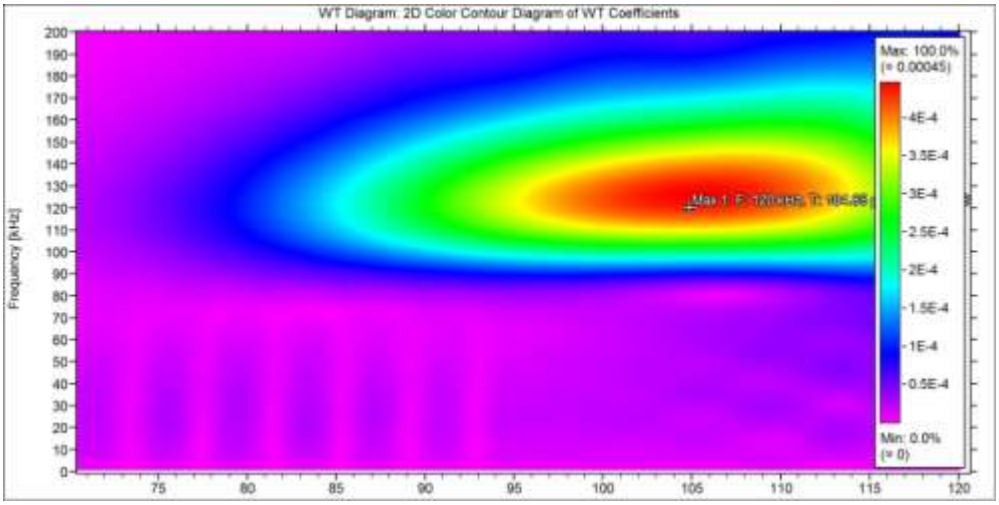

Figure 49 | WT of electrical potential at receiver central node, input signal 120kHz.

5.5 Results

The FE modelling results are presented in Table 18 and Figure 50 to Figure 52. As with the experimental results, the difference in Time of Arrival (ToA) at the receiver between the damaged and undamaged panel is expressed as an absolute number, while the difference in energy is expressed as a relative number. The difference in ToA was calculated as follows:

$$\Delta ToA = ToA_d - ToA_u \qquad (5.2)$$

Where the indices d and u indicate damaged and undamaged respectively.

The difference in through-transmitted energy ΔE was calculated from:

$$\Delta E = \frac{E_d - E_u}{E_u} \cdot 100\% \qquad (5.3)$$

Table 18 | FE analyses results.

#	Debonding size b [mm]	ToA [μs]		|WT| [mV]	
		Undamaged	Damaged	Undamaged	Damaged
1	11.0	104.95	104.85	0.00054	0.00043
2	18.5	104.95	103.55	0.00054	0.00039
3	20.5	104.95	102.75	0.00054	0.00038
4	23.0	104.95	102.45	0.00054	0.00036
6	26.0	104.95	101.05	0.00054	0.00033

The ΔToA and ΔE found in experiments and FE modelling are plotted in combined figures. The plots show that the FE model predicts the same trend of decreasing ToA (Figure 50) and energy (Figure 51) as was found in the experiments. However, the FE model appears to generally over-estimate the decrease, especially in case of through-transmitted energy. A possible explanation is that, since viscoelastic effects were not accounted for in the model, attenuation of the undamaged baseline was not adequately modelled. The increase of attenuation due to impact damage could thus be larger relative to the baseline.

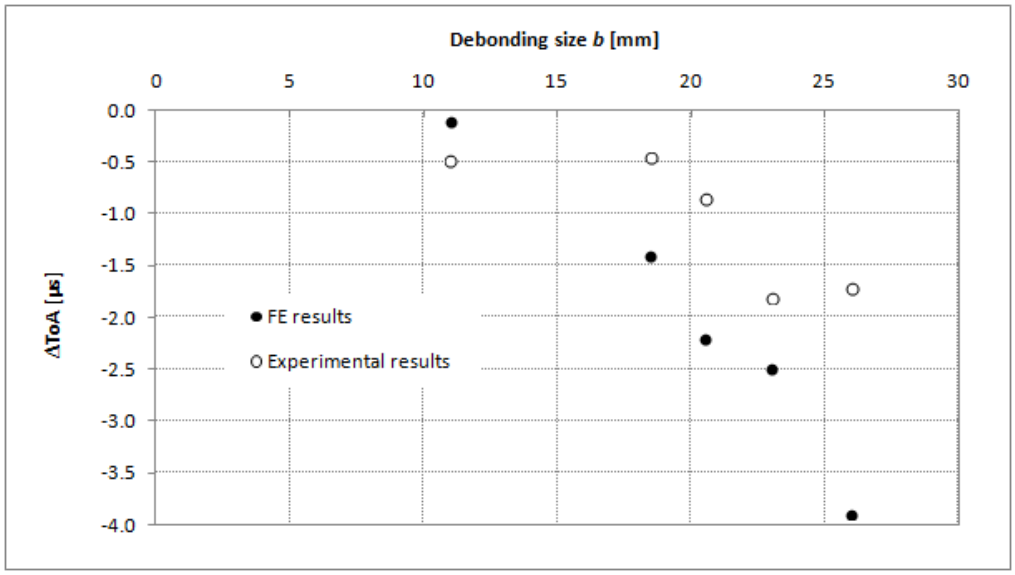

Figure 50 | Absolute difference in ToA against debonding size (f=120kHz).

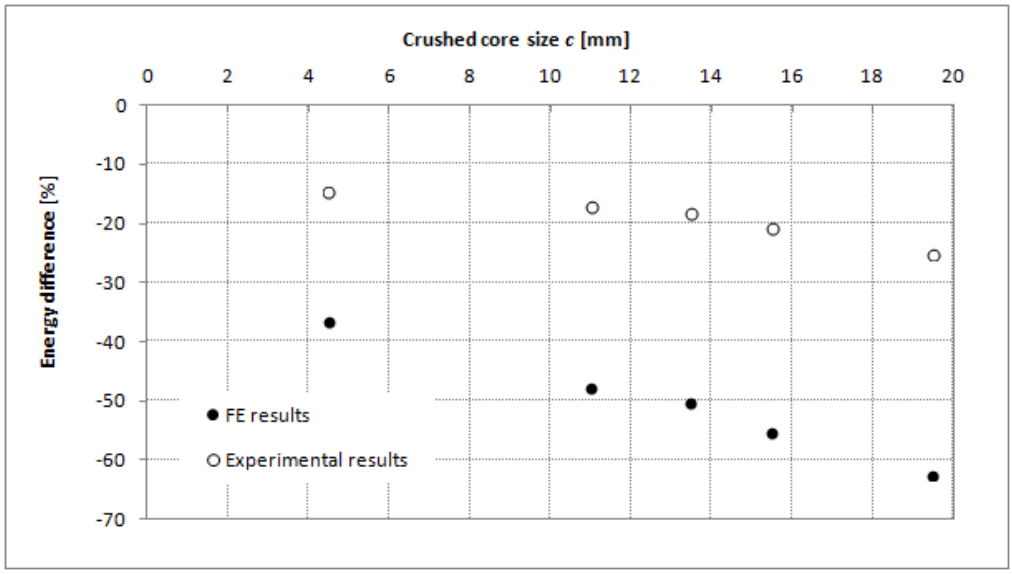

Figure 51 | Relative difference in WT against damage size (f=120kHz).

To obtain some measure of the error in the FE model in the time domain, the modelled c_g was compared to experimental results. For the undamaged baseline model the time difference of the WT peak between transmitter and receiver was 84.1μs, which over the distance of 0.194m corresponded to a c_g of 2307m/s. The average c_g found in section 4.2 at central frequency 120kHz was 2356m/s. The error of the modelled c_g can then be calculated to be 2.1%.

A measure of error for the damaged panel models was calculated from the ToA of the signal at the receiver. The error was calculated using:

$$r_{ToF} = \frac{ToA_{FE} - ToA_{Exp}}{ToA_{Exp}} \cdot 100\% \qquad (5.4)$$

Where ToA_{FE} is the modelled ToA and ToA_{Exp} the experimental ToA. The results are plotted in Figure 52, which shows that the error remains within 2%.

The modelling error in through-transmitted energy was not calculated since attenuation was not accurately modelled. Such number would thus be meaningless.

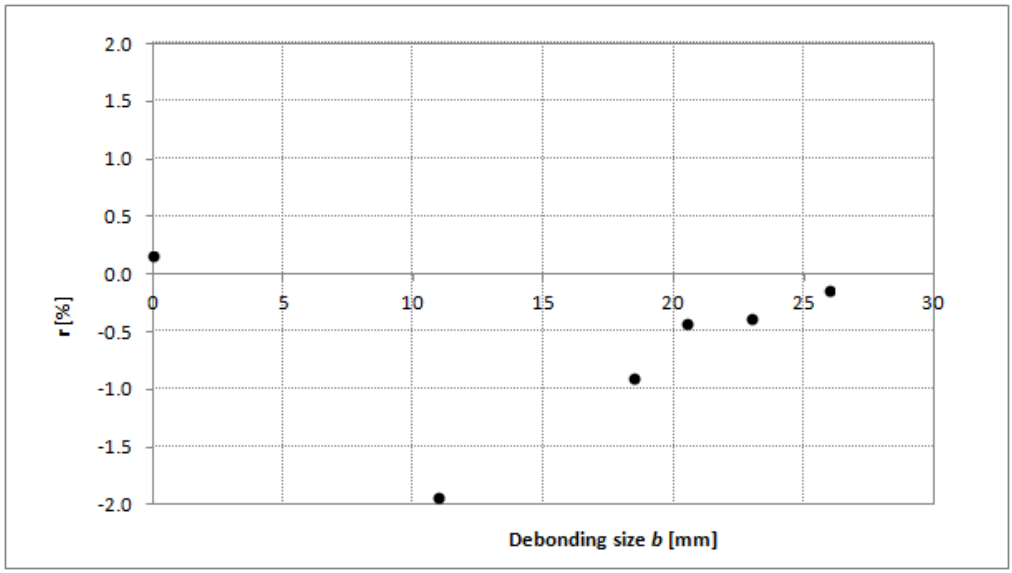

Figure 52 | Error in ToA against damage size.

The normalized transient amplitude of the signal at the receiver is plotted in Figure 53 for the undamaged baseline and in Figure 54 for the model and specimen with damage, where the specific case of 23 mm debonding size was used. These figures allow for comparison of the FE model output with experimental results. The amplitude was normalized with respect to the peak amplitude of the respective signals. The figures confirm that the arrival time of the peak amplitude is predicted well by the FE model. It can also be seen that the shape of the pulse is not predicted well, which is due to the fact that the model was not capable of simulating attenuation adequately.

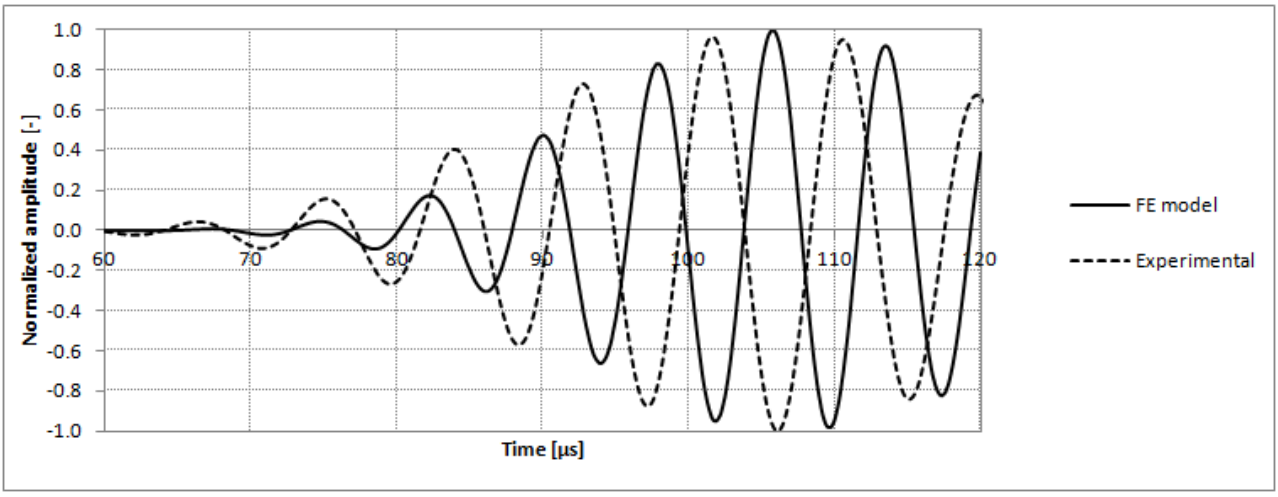

Figure 53 | Received signal from the undamaged baseline, normalized with peak amplitude, with 120kHz central frequency.

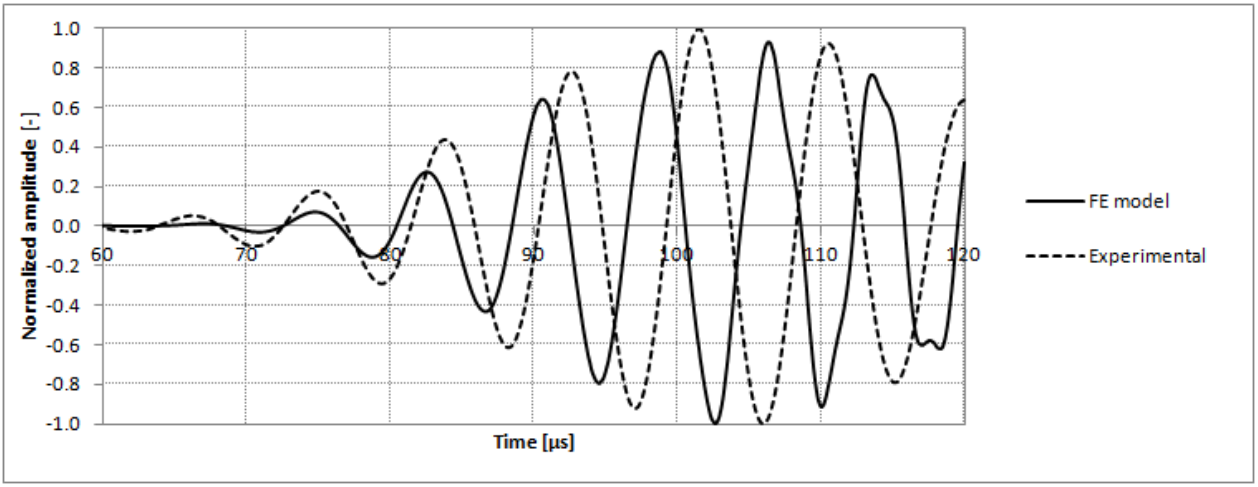

Figure 54 | Received signal from the FE model and specimen with impact damage (debonding size 23mm), normalized with peak amplitude, with 120kHz central frequency.

6 Results and Discussion

The aim of the research presented in this report was to investigate the functionality of active acoustic SHM using a pitch-catch setup for the DragonFly fuselage. A number of deliverables and research questions were defined in section 1.2. In this section, the results are presented and discussed.

In the study of open literature it was found that the way in which guided waves propagate through a sandwich composite medium was only partly documented. The fragments from previous studies were combined into a comprehensive overview of propagation modes, ordered by the frequency-thickness products at which they occur. Two Lamb wave propagation modes were found to be of interest for the detection of BVID in sandwich composites using a pitch-catch setup: the Leaky Lamb Wave (LLW) and Global Lamb Wave (GLW). The occurrence of these modes was found to depend on the central frequency of the acoustic signal, the wavelength and phase velocity of the Lamb wave in the sandwich structure, and the bulk shear and longitudinal velocities in the core. Dispersion curves for the sandwich composite structure were generated using an analytical model developed by Pant, Laliberte et al. (2014), approximating the sandwich structure as a lumped continuum model. The dispersion curve of the S_0 thus obtained could be reproduced experimentally, but only for the GLW propagation mode.

Applications of both LLWs and GLWs in active acoustic SHM with a pitch-catch setup were encountered in open literature. However, LLWs were found to be of limited use in the thin DragonFly fuselage because subsequent leaky wave modes were estimated to largely overlap, thus complicating feature extraction. In open literature GLWs were investigated using only simulated impact damage. Although this allows for the study of the sensitivity to individual damage modes without interference from other damage modes, this excludes the complexity of actual impact damage. In this study, then, previous work was expanded upon by investigating the sensitivity to actual impact damage to verify whether the results from simulated impact damage could be replicated. Based on the literature review, impact damage was expected to decrease the ToF and increase the attenuation of the through-transmitted S_0 GLW mode, while decreasing attenuation of the S_0 LLW mode. These expectations were confirmed both experimentally and through FEM simulations.

The impact damage resistance of the DragonFly fuselage structure was investigated both theoretically and experimentally. BVID, defined as impact damage with residual indentation less than 0.5mm, was shown to result from low velocity impacts with a hemispherical impactor at impact energy levels below 10J. The damage consisted of minor residual indentation on the impact side, debonding of the impacted skin and core, core crushing and matrix cracks in the skin opposite to the impact. C-scan images of impacted specimens were used in combination with optical microscopy to identify the damage modes and determine their respective sizes. The diameter of the damaged area increased near linearly with impact energy, as was expected from theory. Based on a literature study to the residual strength of impacted sandwich composites a damage size detectability threshold of 10 mm was defined for SHM.

A simple data analysis model for feature discrimination was developed based on the Wavelet Transform operation on received signals. The Wavelet Transform was used for conversion of transient signals into detailed magnitude plots in the time-frequency domain. This method was shown to allow for reliable extraction of the through-transmitted energy peak at any frequency. Also, the time of arrival of this energy peak could be accurately determined. Furthermore, the method was shown to be very useful for post-processing of FEM simulation results. By using the same method for both experimental and simulation data, the model performance could be accurately verified.

A digital twin formulation of a sandwich composite test panel with piezoelectric transducers was developed, including impact damage. The panel was made up of two planar shells for the skins and a solid for the core, simulating bonding between skin and core by introducing tie constraints. Mechanical properties of the constituent materials were determined through mechanical testing and calculations. Impact damage was simulated as follows: core crushing by locally modifying the core properties, matrix cracking by locally removing the compressive load bearing capacity of the skin and debonding by locally replacing the tie constraint between skin and core by a surface-to-surface contact interaction. Piezoelectric transducers were simulated by replicating their geometry and piezoelectric material definition and meshing with piezoelectric brick elements. A 5-cycle Hanning windowed pulse with 120 kHz central frequency was used as input signal for the transmitter. Mesh size was optimized for the expected wavelength. Another optimization was performed for the time step increment. Simulations of the transient response run with an undamaged panel showed an error of the modelled group velocity of 2.1%. The error of the modelled time of arrival in damaged panels was below 2.0%.

Experiments were conducted to verify the theoretical wave propagation model and the FEM simulations. It was found that the group velocity of the S_0 mode at low frequencies was close to the value predicted with a lumped continuum model for the sandwich structure. For some frequencies, however, the group velocity was found to be higher. It was argued that this was due to the propagation of the wave as an LLW, which was supported by the fact that the group velocity was close to that of the skin. Further confirmation of LLW propagation was found from the response to the presence of impact damage, which corresponded to the expectation that impact damage would decrease attenuation of a through-transmitted signal if the propagation was leaky.

Experimental and modelling results showed that an SHM system capable of detecting Barely Visible Impact Damage could be made for the DragonFly fuselage structure using an active acoustic system with a pitch-catch setup. The central frequency for interrogation of the structure was chosen in the GLW range of the S_0 mode (120 kHz), which proved to be beneficial for several reasons:

- The S_0 mode has the highest propagation velocity at this frequency, which makes it possible to clearly distinguish the signal of interest from boundary reflections and slower modes, as it is always the first to arrive at the sensor.
- The wave length of the GLW S_0 mode is short enough to detect damage sizes down to 10mm, in accordance with the diffraction limit. The wave length of the LLW S_0 mode was too long to detect the smaller debonding size.

- The GLW S_0 mode may be expected to be sensitive to all damage modes identified for BVID, since particle displacement occurs through the thickness of the panel, as opposed to the A_0 mode. This was, however, not verified experimentally or in simulations.

The results of the study presented here suggest, then, that early damage detection is possible with the chosen SHM setup. It is worth noting here that several challenges would need to be overcome to come to a successful application in the actual DragonFly fuselage structure. Some of those challenges are briefly addressed here.

The largest ToA difference due to impact damage found was 1.8μs. This corresponds roughly 2%. This difference is very small if we compare it to the effect of other influences, such as structural difference of the medium. Let us consider, for example, that the difference between the maximum and minimum ToA found in different undamaged panels was as high as 4.5μs, or roughly 4%. This difference may be largely attributed to minor structural variations between sandwich panel specimens. Other factors of influence are variations in the environmental conditions. As a case in point, a decrease of group velocity in excess of 4% was found in a sandwich panel by Vargalui (2015) as the result of a 45°C temperature increase. Other external influences include humidity and stress state of the structure. It is apparent, then, that successful feature extraction and damage identification depends on a thorough understanding of the conditions that influence this feature. Without that, false positive responses are very likely to occur.

To conclude this thesis, let us return to the research questions and assess to what extent they have been answered and what suggestions can be made for further research.

How can BVID in a lightweight sandwich composite structure be characterized and how can this characterization be translated to FEM simulations?
Literature research and experimental investigation resulted in a characterization of BVID in the DragonFly fuselage with three damage modes: matrix cracking, core crushing and skin-core debonding. Those damage modes were successfully translated to FEM simulations. The simulated response of the damaged structure to acoustic signals showed the same trend as experimental results, although the magnitude of the effect was generally overestimated. A study to the individual influence of each damage mode and an update of the FEM model would be required to verify if the modelling error can be reduced further. Another expansion of the modelling effort could be to model the occurrence of GLW and LLW propagation in order to verify the experimental result from the current study.

How do acoustic waves propagate through a lightweight sandwich composite structure and how is this propagation affected by BVID?
The distinction between four propagation modes was made in this study: GLW, True modes, LLW and Rayleigh Waves. Empirical evidence was found for the occurrence of the fundamental symmetric GLW and LLW propagation modes. Both theoretical and experimental investigations showed that these propagation modes are affected differently by BVID. Most notably, the through-transmitted energy was decreased for the GLW modes, while it was increased for the LLW modes.

It should be noted that the experimental results on the LLW propagation were limited and conclusions based on those results should be treated with caution. Further experimentation and modelling is required to conclusively confirm its occurrence in the DragonFly fuselage. This investigation would require an optimized setup for higher frequencies (e.g. piezoelectric transducers with good frequency response at the higher frequencies).

Can we develop a digital twin formulation of this type of structure with active acoustic SHM system that allows us to predict the effect of BVID on selected features of the through-transmitted acoustic signal?

A digital twin formulation was developed successfully, but as was concluded in this section the effect of several influences (e.g. environmental conditions, structural variations, etc.) would have to be included in the model to avoid false-positive responses. This aspect of SHM represents a vast and challenging field of study.

References

Abrate, S. (2001). "Modeling of impacts on composite structures." Composite Structures **51**(2): 129-138.

Anderson, T. and E. Madenci (2000). "Experimental investigation of low-velocity impact characteristics of sandwich composites." Composite Structures **50**(3): 239-247.

ASTM (1994). Standard Test Method for In-Plane Shear Response of Polymer Matrix Composite Materials by Tensile Test of a ±45º Laminate. **D 3518/D 3518M - 94 (Reapproved 2001)**.

ASTM (2000a). Standard Test Method for Tensile Properties of Polymer Matrix Composite Materials. **D 3039/D 3039M - 00 (Reapproved 2006)**.

ASTM (2000b). Standard Test Method for Density and Specific Gravity (Relative Density) of Plastics by Displacement. **D 792 - 00**.

ASTM (2005). Standard Test Method for Measuring the Damage Resistance of a Fibre-Reinforced Polymer Matrix Composite to a Drop-Weight Impact Event. **D 7136/D 7136M - 05**.

ASTM (2006). Standard Test Method fo Constituent Content of Composite Materials. **D 3171 - 06**.

ASTM (2012). Standard Test Method for Compressive Residual Strength Properties of Damaged Polymer Matrix Composite Plates. West Conshohocken, PA, ASTM International. **D7137 / D7137M-12**.

Bertoni, H. L. and S. K. Park (1981). "Propagation of Elastic Waves in Honeycomb Panels for Application to Rapid Inspection Techniques." Journal of Nondestructive Evaluation **2**(3/4): 209-217.

Boon, M. (2014). Temperature and Load Effects in Modelling and Experimental Verification of Acoustic Emission Signals for Structural Health Monitoring Applications. Faculty of Aerospace Engineering. Delft, Delft University of Technology. **Master of Science**.

Bourasseau, N., et al. (2000). "Radome health monitoring with Lamb waves: experimental approach." Ndt & E International **33**(6): 393-400.

Burlayenko, V. N. and T. Sadowski (2009). "Free Vibration of Sandwich Plates with Impact-Induced Damage." Proceedings in Applied Mathematics and Mechanics **9**: 179-180.

Campbell, F. C. (2004). Manufacturing Processes for Advanced Composites. Oxford, Elsevier Advanced Technology.

Caprino, G. and R. Teti (1994). "Impact and Postimpact Behavior of Foam Core Sandwich Structures." Composite Structures **29**(1): 47-55.

Castaings, M. and B. Hosten (2003). "Guided waves propagating in sandwich structures made of anisotropic, viscoelastic, composite materials." Journal of the Acoustical Society of America **113**(5): 2622-2634.

Daniel, I. M., et al. (2012). "Response and Damage Tolerance of Composite Sandwich Structures under Low Velocity Impact." Experimental Mechanics **52**(1): 37-47.

Daniel, I. M. and O. Ishai (1994). Engineering Mechanics of Composite Materials. New York, Oxford University Press.

Diamanti, K., et al. (2005). "Lamb waves for the non-destructive inspection of monolithic and sandwich composite beams." Composites Part a-Applied Science and Manufacturing **36**(2): 189-195.

Edgren, F., et al. (2004). "Compressive failure of impacted NCF composite sandwich panels - Characterisation of the failure process." Journal of Composite Materials **38**(6): 495-514.

Freeman, B., et al. (2005). "The effect of low-velocity impact on the fatigue life of Sandwich composites." Composite Structures **70**(3): 374-381.

Fujita, T. and K. Toda (2004). "Operational performance of A(0)-mode Lamb wave interdigital transducers under water-loaded condition." Japanese Journal of Applied Physics Part 1-Regular Papers Short Notes & Review Papers **43**(8A): 5577-5581.

Gao, H. D., et al. (2010). "Efficient detection of delamination in multilayered structures using ultrasonic guided wave EMATs." Ndt & E International **43**(4): 316-322.

Giurgiutiu, V. (2008). Structural Health Monitoring with Piezoelectric Wafer Active Sensors. Amsterdam, Elsevier.

Guo, N. and M. K. Lim (1996). Lamb waves propagation in aluminum honeycomb structures. Review of Progress in Quantitative Nondestructive Evaluation, Vols 15a and 15b. D. O. Thompson and D. E. Chimenti. New York, Plenum Press Div Plenum Publishing Corp. **15:** 323-330.

Hay, T. R., et al. (2003). "Rapid inspection of composite skin-honeycomb core structures with ultrasonic guided waves." Journal of Composite Materials **37**(10): 929-939.

Hazizan, M. A. and W. J. Cantwell (2002). "The low velocity impact response of foam-based sandwich structures." Composites Part B-Engineering **33**(3): 193-204.

Kishimoto, K., et al. (1995). "Tome Frequency Analysis of Dispersive Waves by Means of Wavelet Transform." Journa of Applied Mechanics **62**: 841-846.

Kollár, L. P. S., G.S. (2003). Mechanics of Composite Structures. Cambridge, Cambridge University Press.

Lacy, T. E. and Y. Hwang (2003). "Numerical modeling of impact-damaged sandwich composites subjected to compression-after-impact loading." Composite Structures **61**(1-2): 115-128.

Lamb, H. (1917). "On Waves in an Elastic Plate." Philosophical Transactions of the Royal Society, London, Series A **93**: 114-128.

Love, A. E. (1911). Some Problems of Geodynamics. London, Cambridge University Press.

Lowe, M. J. S. and P. Cawley (1994). "The Applicability of Plate Wave Techniques for the Inspection of Adhesive and Diffusion Bonded Joints." Journal of Nondestructive Evaluation **13**(4): 185-200.

Martinez, D. M. J. (2013). DragonFly Solar Power Amphibious UAV. Design and Synthesis Exercise 2012/2013. Delft, TUDelft.

Meo, M., et al. (2005). "Impact identification on a sandwich plate from wave propagation responses." Composite Structures **71**(3-4): 302-306.

Mustapha, S. and L. Ye (2014). "Leaky and non-leaky behaviours of guided waves in CF/EP sandwich structures." Wave Motion **51**(6): 905-918.

Mustapha, S., et al. (2011). "Assessment of debonding in sandwich CF/EP composite beams using A(0) Lamb wave at low frequency." Composite Structures **93**(2): 483-491.

Osmont, D., et al. (2001). Health monitoring of sandwich plates based on the analysis of the interaction of Lamb waves with damages. Smart Structures and Materials 2001: Smart Structures and Integrated Systems. L. P. Davis. **4327:** 290-301.

Pant, S., et al. (2014). "Derivation and experimental validation of Lamb wave equations for an n-layered anisotropic composite laminate." Composite Structures **111**: 566-579.

Qi, X., et al. (2008). Ultrsonic Guided Wave Nondestructive Testing for Helicopter Rotor Blades. 17th World Conference on Nondestructive Testing, 25-28 Oct 2008. Shanghai, China.

Raghavan, A. and C. E. S. Cesnik (2007). "Review of Guided-wave Structural Health Monitoring." The Shock and Vibration Digest **39**(2): 24.

Rayleigh, L. (1885). "On Wave Propagating Along the Plate Surface of an Elastic Solid." Proceedings of the London Mathematical Society **17**: 4-11.

Reda Taha, M. M., et al. (2006). "Wavelet Transform for Structural Health Monitoring: A Compendium of Uses and Features." Structural Health Monitoring **5**(3): 267-295.

Rocha, S. e. a. (2013). Structural Health Monitoring of Aircraft Structures. New Trends in Structural Health Monitoring. W. Ostachowicz. Wien, Springer**:** 81-148.

Shipsha, A., et al. (2003). "Failure mechanisms and modelling of impact damage in sandwich beams - A 2D approach: Part I - Experimental investigation." Journal of Sandwich Structures & Materials **5**(1): 7-31.

Shipsha, A. and D. Zenkert (2003). "Fatigue behavior of foam core sandwich beams with sub-interface impact damage." Journal of Sandwich Structures & Materials **5**(2): 147-160.

Sohn, H., et al. (2004). "Wavelet-Based Active Sensing for Delmination Detection in Composite Structures." Smart Materials & Structures **13**: 153-160.

Song, F., et al. (2012). "Online Guided Wave-Based Debonding Detection in Honeycomb Sandwich Structures." Aiaa Journal **50**(2): 284-293.

Song, F., et al. (2009). "Guided wave propagation in honeycomb sandwich structures using a piezoelectric actuator/sensor system." Smart Materials & Structures **18**(12).

Soutis, C. and K. Diamanti (2008). "Active sensing of impact damage in composite sandwich panels by low frequency Lamb waves." Aeronautical Journal **112**(1131): 279-283.

Staszewski, W. J. e. a. (2009). "Health monitoring of aerospace composite structures - Active and passive approach." Composites Science and Technology **69**(11-12): 1678-1685.

Thwaites, S. and N. H. Clark (1995). "Non-Destructive Testing of Honeycomb Sandwich Structures using Elastic Waves." Journal of Sound and Vibration **187**(2): 253-269.

Tomblin, J. S., et al. (2001). Impact Damage Characterization and Damage Tolerance of Composite Sandwich Airframe Structures, U.S. Department of Transportation, Federal Aviation Administration.

Ugale, V. B., et al. (2013). "Experimental studies on thin sandwich panels under impact and static loading." Journal of Reinforced Plastics and Composites **32**(6): 420-434.

Vallen (2012). Acoustic Emission Sensors: Specification. Ickind, Germany, Vallen Systeme GmbH.

Vargalui, A. (2015). Temperature Effects on an Acoustic Emission Based Structural Health Monitoring System - Applie to Composite Materials. Faculty of Aerospace Engineering. Delft, Delft University of Technology. **Master of Science**.

Verschuren, P. D., H. (2010). Designing a Research Project. The Hague, Eleven International Publishing.

Wang, L. and F. G. Yuan (2007). "Group velocity and characteristic wave curves of Lamb waves in composites: Modeling and experiments." Composites Science and Technology **67**(7-8): 1370-1384.

Worden, K., et al. (2007). "The fundamental axioms of structural health monitoring." Proceedings of the Royal Society a-Mathematical Physical and Engineering Sciences **463**(2082): 1639-1664.

Appendix I. Material Data Sheets

HexForce® 01035 1200 Z6040

E GLASS FABRIC

Product Data

Textile Reinforcement for High Performance Composite

HexForce® reinforcements are available in a range of weave styles – from woven fabrics to multiaxials and specialties that offers a range of globally certified aerospace / industrial products in carbon, glass and aramid and specialty fibers that we sell under the HexForce® trademark.

DESCRIPTION		**October / 2014**
Type of yarns	Warp : EC9 68 Weft : EC9 68	
Nominal weight	200 g/m²	5.9 oz/sqy²
Weave style	TWILL 2/2	
Width	1200 mm	47.2 in
Finish type	Z6040	
Finish description		

CHARACTERISTICS		
Nominal construction	Warp : 14.7 yarn/cm Weft : 14.7 picks/cm	37.6 yarn/in 37.6 picks/in
Weight distribution	Warp : 50 % Weft : 50 %	
Thickness (*)	0.16 mm	0.006 in

***NB : The above average values are obtained with epoxy laminate at 55% of fibres in volume.**

IMPORTANT

HEXCEL®

For European sales office telephone numbers and a full address list, please go to : http://www.hexcel.com/contact/salesoffices

Product Information

ROHACELL® A

Polymethacrylimide Foam, Aircraft Grade

ROHACELL® A is a closed-cell rigid foam based on polymethacrylimide (PMI) chemistry, which does not contain any CFC's.

Thanks to stringent quality control and the availability of the extensive documentation ROHACELL® A meets the requirements of aircraft construction and is mostly used in this application field.

Because of its relatively large pore structure, ROHACELL® A is particularly suitable in aerospace applications for prepreg processing, but vacuum infusion processing can also be used at temperatures up to 130°C (266°F) and pressures up to 0.3 MPa (45 PSI).

The following cure methods are suitable: autoclave, vacuum bagged, RTM, VARTM, press and others. Sandwich components using ROHACELL® A as core material can be realized in a single work step (co-curing).

The thermo-formability of ROHACELL® provides a tremendous manufacturing advantage.

ROHACELL® A is also easy to shape by machining.

For further information, please contact our experts by phone +49 6151 18 1005 or e-mail rohacell@evonik.com.

January 2011

Properties of ROHACELL® A

Properties	Unit	ROHACELL® 31 A	ROHACELL® 51 A	ROHACELL® 71 A	ROHACELL® 110 A	Standard
Density	kg/m³	32	52	75	110	ISO 845
	lbs./cu.ft.	2.00	3.25	4.68	6.87	ASTM D 1622
Compressive strength	MPa	0.4	0.9	1.5	3.0	ISO 844
	psi	58	130	217	435	ASTM D 1621
Tensile strength	MPa	1.0	1.9	2.8	3.5	ISO 527-2
	psi	145	275	406	507	ASTM D 638
Shear strength	MPa	0.4	0.8	1.3	2.4	DIN 53294
	psi	58	116	188	348	ASTM C 273
Elastic modulus	MPa	36	70	92	160	ISO 527-2
	psi	5,220	10,150	13,340	23,200	ASTM D 638
Shear modulus	MPa	13	19	29	50	DIN 53294
	psi	1,885	2,755	4,205	7,250	ASTM C 273
Strain at break	%	3	3	3	3	ISO 527-2
						ASTM D 638

Technical data of our products are typical values for the nominal density.

® = registered trademark

Evonik Industries AG Performance Polymers 64293 Darmstadt Germany
Phone +49 6151 18-1005 E-mail rohacell@evonik.com
www.rohacell.com

EVONIK INDUSTRIES

poisson ratio of ROHACELL®

the values were determined in a tensile test according DIN 53455 / ASTM D 1622. Due the to the measuring method with the strain gauges there is a scattering of the values. The values represent a series of measurements carried out of Röhm in 1992.

RC Type	
RC 31 IG / A	0,43
RC 51 IG / A	0,4
RC 71 IG / A	0,37
RC 110 IG / A	0,38
RC 51 WF	0,34
RC 71 WF	0,37
RC 110 WF	0,37
RC 200 WF	0,33
RC 300 WF	0,38

BAKELITE® EPR 04908
BAKELITE® EPH 04908
new name: EPIKOTE™ Resin 04908
new name: EPIKURE™ Curing Agent 04908

Features

- Certified by German Lloyd
- Low viscosity
- Extended potlife
- Low exothermic heat

Application

Low viscous resin system designed for infusion applications with excellent wetting and adhesion characteristics on fibreglass, carbon- or aramid-fibres, particularly in boats and yacht-building and production of rotor blades. This system make it possible to manufacture construction elements of a superior quality, with outstanding surface characteristics and good resistance to thermal deformation and weathering.

Product physical properties: (at time of manufacturing)			
Property	**Unit**	**EPR 04908**	**EPH 04908**
Viscosity at 25°C	mPa·s	500 ± 250	10 ± 5
Epoxy equivalent weight	g/equiv.	165 ± 3	
Amine equivalent weigth	g/equiv.		50
Density at 20°C	g/cm³	1.15 ± 0.02	0.93 ± 0.02
Refractive index at 25°C		1.540 ± 0.003	1.468 ± 0.003
Mixing viscosity at 25°C	mPa·s	130 ± 10	
Pot life at 25°C	minutes	300 ± 50	
T_G (TMA)	°C	82	

Varziner Straße 49
47138 Duisburg-Meiderich
Postfach 120652
47128 Duisburg
Germany
Phone: +49 (0) 203 42 96 01
Fax: +49 (0) 203 42 94 222
www.hexionchem.com

BAKELITE® EPR 04908
BAKELITE® EPH 04908
new name: EPIKOTE™ Resin 04908
new name: EPIKURE™ Curing Agent 04908

Processing Details

Mixing ratio

EPR 04908	100 parts by weight
EPH 04908	30 parts by weight

Mixing tolerance
The maximum allowable mixing tolerance is ±2pbw, but it is particularly important to observe the recommend mixing ratio as exactly as possible. Adding more or less hardener will not effect a faster or slower reaction - but an incomplete curing which cannot correct in any way.
Resin and hardener must be mixed very thoroughly. Mix until no clouding is visible in the mixing container. Pay special attention to the walls and the bottom of the mixing container.

Processing temperature
A good processing temperature is in the range between 25°C and 35°C. Higher processing temperatures are possible but will shorten the pot life. A rise in temperature of 10°C reduces the pot life by approx. 50%. Different temperatures during processing have no significant effect on the strength of the hardened product.
Do not mix large quantities at elevated processing temperatures. The mixture will heat up fast because of the dissipating reaction heat (exothermic reaction). This can result in temperatures of more than 200°C in the mixing container.

Exemplify curing cycle:
4- 6h at 80°C

Varziner Straße 49
47138 Duisburg-Meiderich
Postfach 120652
47128 Duisburg
Germany
Phone: +49 (0) 203 42 96 01
Fax: +49 (0) 203 42 94 222
www.hexionchem.com

HEXION™
Specialty Chemicals

Technical Information
Division Epoxy / Phenolic Resins
Epoxy Resins

BAKELITE® EPR 04908
BAKELITE® EPH 04908
new name: EPIKOTE™ Resin 04908
new name: EPIKURE™ Curing Agent 04908

Properties of the cured, non-reinforced resin system: (curing: 4h at 70°C + 6h at 80°C)		
Property	**Unit**	**Value**
Density	g/cm³	1.15
Tensile strength	MPa	74
Tensile strain	%	9.4
Modulus in tensile	MPa	2900
Flexural strength	MPa	112
Modulus in flexure	MPa	3100
Water absorption after 24h 23°C	pbw	0,180
Water absorption after 168h 23°C	pbw	0,432

Properties of the cured, reinforced resin system (curing: 4h at 70°C + 6h at 80°C)		
Property	**Unit**	**Value**
Tensile strength	MPa	447
Flexural strength	MPa	588
Modulus in flexure	MPa	23400
ILSS	MPa	40
T_G (DMTA)	°C	89

The values are measured on laminates made with glass fabric 181/Interglas 91745.

Vanziner Straße 46
47138 Duisburg-Meiderich
Postfach 120652
47128 Duisburg
Germany
Phone: +49 (0) 203 42 96 01
Fax: +49 (0) 203 42 94 222
www.hexionchem.com

BAKELITE® EPR 04908
BAKELITE® EPH 04908
new name: EPIKOTE™ Resin 04908
new name: EPIKURE™ Curing Agent 04908

Shelf life

The resin and hardener can be stored at 20- 25°C for at least 12 months in their carefully sealed original containers.
It is rarely possible that the resin or the hardener crystallize at temperatures below 15°C. The crystallisation is visible as a clouding or solidification of the content of the container. Before processing, the crystallisation must be removed by warming up. Slow warming up to 50- 60°C in a water bath or oven and stirring or shaking will clarify the contents in the container without any loss of quality. Use only completely clarify products. Before warming up, open containers slightly to permit equalization of pressure. Caution during warm up! Do not warm up over open flame!

Precautions

When handling epoxy resins and hardeners, will you please observe the APME documentation "Epoxy resins and curing agents".

Vanziner Straße 49
47138 Duisburg-Meiderich
Postfach 120652
47128 Duisburg
Germany
Phone: +49 (0) 203 42 96 01
Fax: +49 (0) 203 42 94 222
www.hexionchem.com

Appendix II. Coupon Production Logbook Sheet

1. General information:	
a. Name:	**Ewoud Aaij**
b. Date:	**22-01-2015**
c. Time:	**13:00**
d. Location:	**Delft DASML**
e. Laminate ID (dd_mm_yyyy__number):	**22012015090**
2. Fibre:	
a. Fibre type: (Glass, carbon, etc.)	**Glass**
b. Manufacturer:	**Hexcel**
c. Manufacturers' identification code:	**Hexforce 01035 1200 Z6040**
d. Batch & roll number:	**Batch 85M208142632z**
e. Fibre properties:	
▪ Weave style (Satin, plain, UD, etc):	**Twill 2/2**
▪ Sizing:	**Z6040 – epoxy silane**
▪ Fibre areal weight:	**200 g/m^2**
f. Lay-up:	**$[0°]_{16}$**
g. Laminate length & width (cm):	**60x60**
4. Resin + hardener:	
a. Name:	**Epikote 04908**
b. Manufacturer:	**Hexion**
c. Batch number:	**Resin: DG3L40035A** **Hardener: DG3D70073A**
d. Mixing ratio:	**100:30 parts by weight**
5. Consumables:	
a. Type of peel ply and/or release film:	**Perforated foil (fine)** **WL 3900 RMP. 22.030**
b. Type and size of flow mesh:	**White** **Ce-sense BSP white**
c. Type of vacuum bag:	**Clear** **WL 5400**
d. Type of sealant tape:	**Black** **AT 199**
e. Type and length of tube:	**PE 9mm inner diameter** **Length 150 cm**
f. Type and length of spiral:	**60 cm**
6. Resin preparation:	
a. Amount of part A used (grams):	**883 | 790**
b. Amount of part B used (grams):	**267 | 241**
c. Amount of additional parts used (grams):	**-**
d. Time at start mixing:	**17:10 | 17:35**
e. Amount of time degassed:	**10 min**
f. Vacuum pressure during degassing:	**Down to 6 mBar**
g. Resin left-over after infusion (grams):	**110+**

7. Production:		
h.	Temperature and humidity (ºC/%RH):	**19.5 °C / 26 %RH**
i.	Leak at max. vacuum (mbar/min):	**0.3 mbar/min**
j.	Injection pressure (mbar):	**53 mbar**
k.	Time at start infusion:	**17:30 | 17:50**
l.	Time at pressure increase:	**18:03**
m.	Time at closing of inlet:	**18:07**
n.	Curing pressure (mbar):	**507**
o.	Time & date at switch-off pump:	**10:00 on 23-01-2015**
8. Results / other remarks:		
During infusion it became apparent that insufficient resin was prepared. Infusion was paused by closing resin inlet and additional resin was mixed, degassed and added to the reservoir. Pouring of the resin resulted in air bubbles in the resin. Infusion was then continued. Coupon cutting sketch is given in Figure 1, a series of pictures of the production process is given in Figures 2 to 5.		

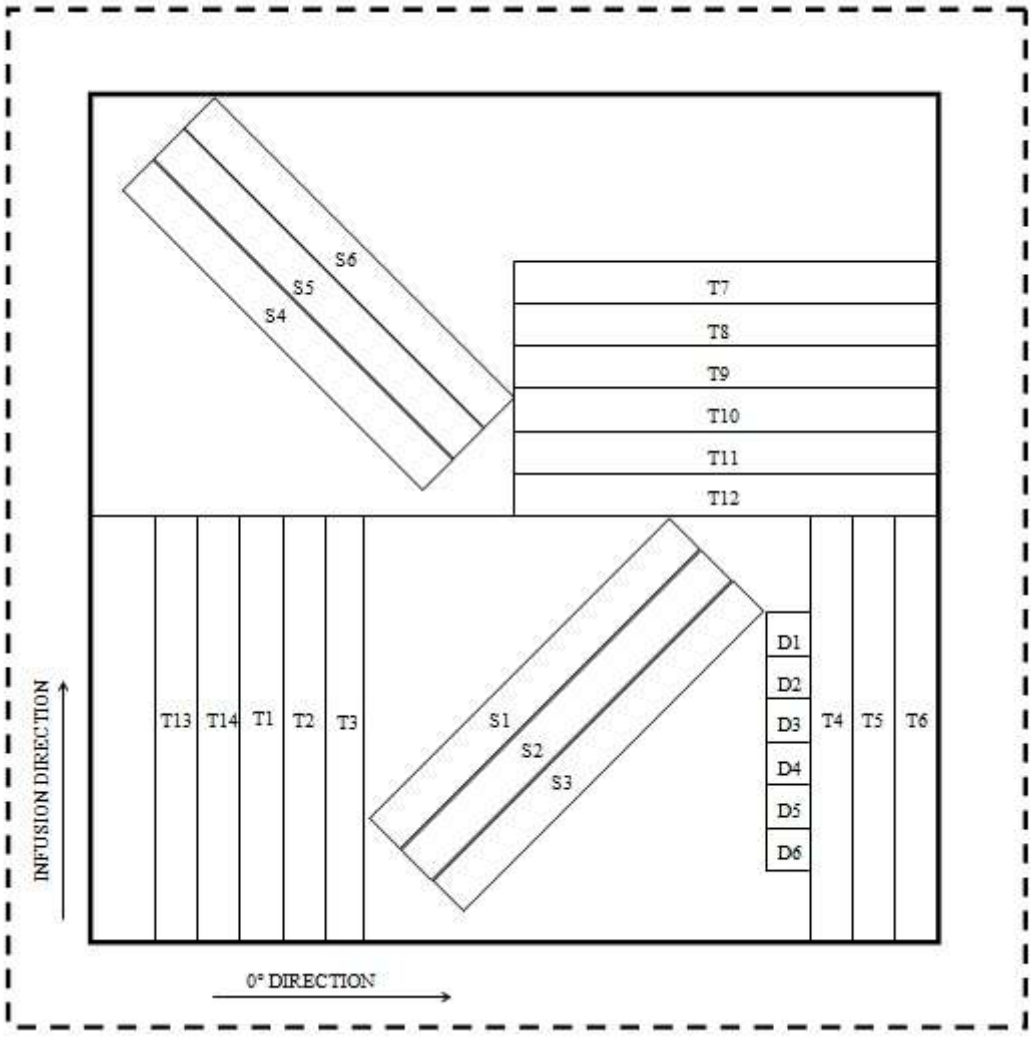

Figure 1 | Coupon cutting sketch.

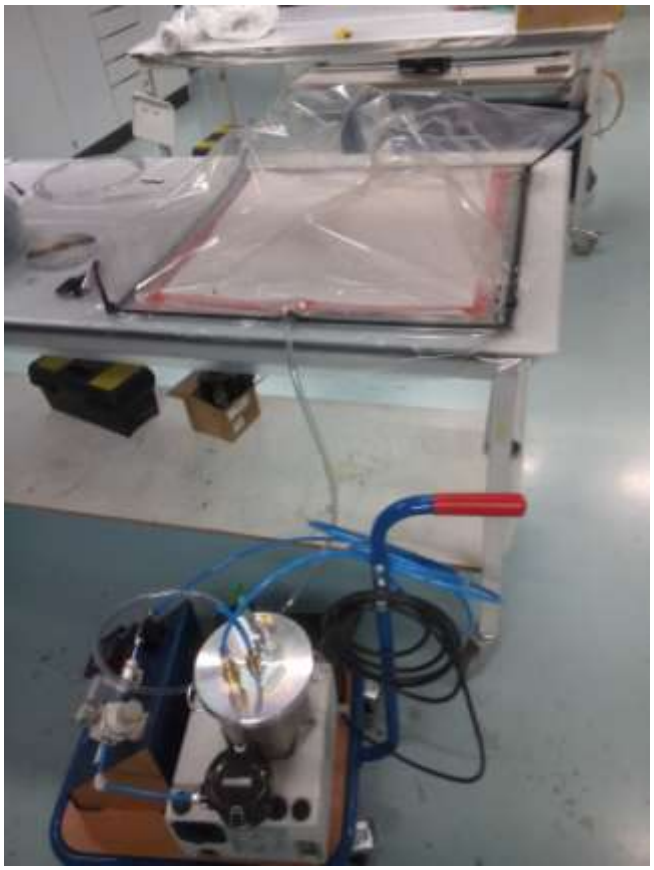

Figure 2 | Vacuum infusion set-up.

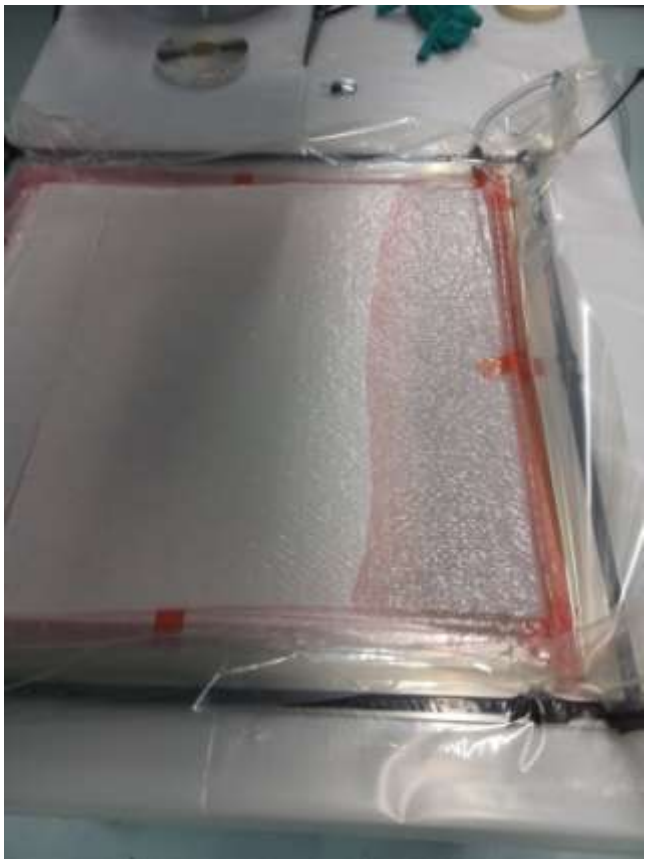

Figure 3 | Infusion after 2 minutes.

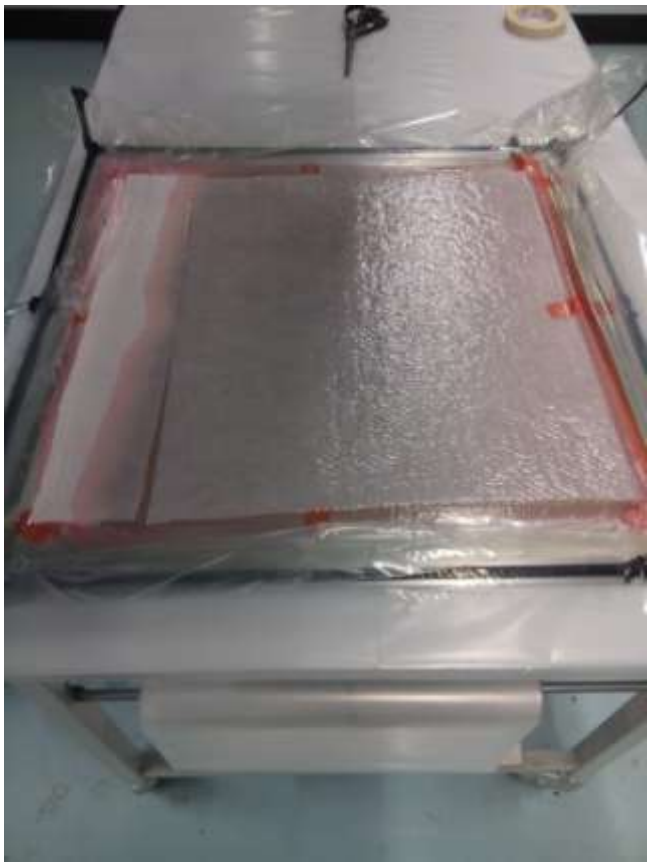

Figure 4 | Infusion after 25 minutes.

Figure 5 | Cured panel.

Appendix III. Tensile Test Report

General Information

This tensile test is conducted to determine Young's modulus and Poisson's ratio in the longitudinal (0°) and transverse (90°) direction, as well as the in-plane shear modulus.

Test standard:	ASTM D3039 (reapproved 2006)
	ASTM D3518 (reapproved 2001)
Executed:	Delft, 19-2-2015, by Ewoud Aaij
Test equipment:	Zwick 250kN
	hydraulic grips
	extensometer (for longitudinal strain measurement)
	strain gauges (for transverse strain measurement)

Materials

Laminate:	22012015090, see Appendix Coupon Production
Average ply thickness:	0.17 mm
Density:	1852 kg/m^3
Fibre volume fraction:	0.45

Specimen Preparation

Specimen are cut from laminate 22012015090 with an Unitom-5 cutting machine.

Sampling:	see Appendix Coupon Production
Tabs:	Paper
Strain gauges:	Kyowa KFG-5-120-C1-23
	Resistance 119.8±0.2Ω
	Length 5mm
	Gauge factor 2.12±1.0% (24°C, 50%RH)
	Location transverse centred

Specimen numbers T1, T2, T3, T12 and S3 were rejected due to cutting irregularities, because such irregularities could propagate early failure and thus corrupt measurements. The remaining specimen are measured with calliper (thickness and width) and with a ruler (length). Values are reported in Table 1, pictures of the specimen after testing are included in Figure 1.

Table 1 | Specimen dimensions.

ID	Purpose	Thickness (mm)				Width (mm)				Length (mm)			
T1	Tension 90° direction	Rejected											
T2	Tension 90° direction	Rejected											
T3	Tension 90° direction	Rejected											
T4	Tension 90° direction	2.64	2.72	2.71	2.69	25.39	25.86	25.30	25.52	251.00	251.00	251.00	251.00
T5	Tension 90° direction	2.63	2.69	2.66	2.66	24.95	23.58	23.83	24.12	251.00	251.00	251.00	251.00
T6	Tension 90° direction	2.65	2.74	2.71	2.70	25.15	25.45	24.81	25.14	250.50	250.50	250.00	250.33
T7	Tension 0° direction	2.79	2.79	2.74	2.77	25.12	25.04	24.94	25.03	250.00	250.00	250.00	250.00
T8	Tension 0° direction	2.82	2.88	2.77	2.82	25.34	25.14	24.80	25.09	250.00	250.00	250.00	250.00
T9	Tension 0° direction	2.78	2.81	2.71	2.77	25.24	25.17	25.09	25.17	250.00	250.00	250.00	250.00
T10	Tension 0° direction	2.77	2.87	2.78	2.81	25.18	25.24	25.31	25.24	250.00	250.00	250.00	250.00
T11	Tension 0° direction	2.75	2.78	2.74	2.76	25.28	24.96	24.87	25.04	250.00	250.00	250.00	250.00
T12	Tension 0° direction	Rejected											
T13	Tension 90° direction	2.68	2.79	2.76	2.74	24.92	24.81	25.16	24.96	250.50	250.50	251.00	250.67
T14	Tension 90° direction	2.67	2.79	2.76	2.74	25.40	25.31	25.02	25.24	250.00	250.00	250.00	250.00
S1	Tension 45° direction	2.71	2.72	2.64	2.69	24.89	25.29	25.59	25.26	249.50	249.50	249.00	249.33
S2	Tension 45° direction	2.73	2.71	2.68	2.71	25.40	25.39	25.45	25.41	249.00	249.00	249.00	249.00
S3	Tension 45° direction	Rejected											
S4	Tension 45° direction	2.79	2.79	2.79	2.79	25.48	25.25	25.11	25.28	250.00	250.00	250.00	250.00
S5	Tension 45° direction	2.72	2.78	2.72	2.74	25.53	25.13	25.11	25.26	251.00	251.00	250.50	250.83
S6	Tension 45° direction	2.77	2.76	2.83	2.79	25.08	25.48	24.72	25.09	251.00	251.00	251.00	251.00

Figure 1 | Specimen after tensile tests.

Test Conditions

Lab environment:	temperature 22.3°C, humidity 33%RH
Test end:	Maximum load (no failure)
	18kN for tension specimen
	5.5kN for shear specimen
Alignment:	Specimen are aligned using fittings

Results and Discussion

Data collected:	Longitudinal strain in mm
	Standard force in N
	Transverse strain in V

Calculations are performed according to test standards. In addition, the transverse strain in V (ε_v) is converted to dimensionless strain (ε_t) using the following formula:

$$\varepsilon_t = \varepsilon_V r \frac{2}{GF}$$

Where r is the selected strain ratio and GF is the gauge factor. The strain ratio was set to 0.001 strain per Volt for the 0° and 90° directions, and to 0.004 strain per volt for the 45° direction.

The strain ranges used in the various calculations are:

Young's modulus:	0.001 to 0.003
Poisson's ratio:	0.001 to 0.003
Shear modulus:	0.0005 to 0.0045

Test results are given in Figures 1 to 5 and Table 2. As can be seen in the figures, the results are generally consistent. It can be noted in Figure 2 that the transverse strain of specimen T7 is off by roughly 50%. This is due to the fact that the strain gauge turned out to be not well bonded. The data of specimen T7 have not been used in the calculation of Poisson's ratio. Specimen T6 failed at the top grip due to a cutting irregularity, but this event occurred outside the strain range used in the calculations and the data could still be used. The Poisson's ratio of the shear specimen is not used in the current study, but is reported here as a verification of the data consistency.

Table 2 | Result summary.

0° direction				
ID	S_0 (mm^2)	L_0 (mm)	E (GPa)	ν
T7	69.3	49.92	23.59	~~0.06~~
T8	70.8	50.20	23.56	0.12
T9	69.7	49.96	23.68	0.13
T10	70.9	50.04	23.26	0.13
T11	69.1	49.99	23.43	0.13
Mean			23.5	0.13
s			0.16	0.003
CV (%)			0.69	2.18
90° direction				
ID	S_0 (mm^2)	L_0 (mm)	E (GPa)	ν
T4	68.6	50.17	23.66	0.12
T5	64.2	50.00	22.89	0.12
T6	67.9	49.99	23.95	0.12
T13	68.4	50.01	23.36	0.13
T14	69.2	49.96	23.38	0.12
Mean			23.4	0.12
s			0.39	0.002
CV (%)			1.68	1.78
45° direction				
ID	S_0 (mm)	L_0 (mm)	G (GPa)	ν
S1	67.9	50.20	3.83	0.38
S2	68.9	50.03	3.77	0.37
S4	70.6	50.16	3.73	0.37
S5	69.2	50.03	3.81	0.37
S6	70.0	50.18	3.79	0.37
Mean			3.8	0.37
s			0.038	0.007
CV (%)			1.01	1.82

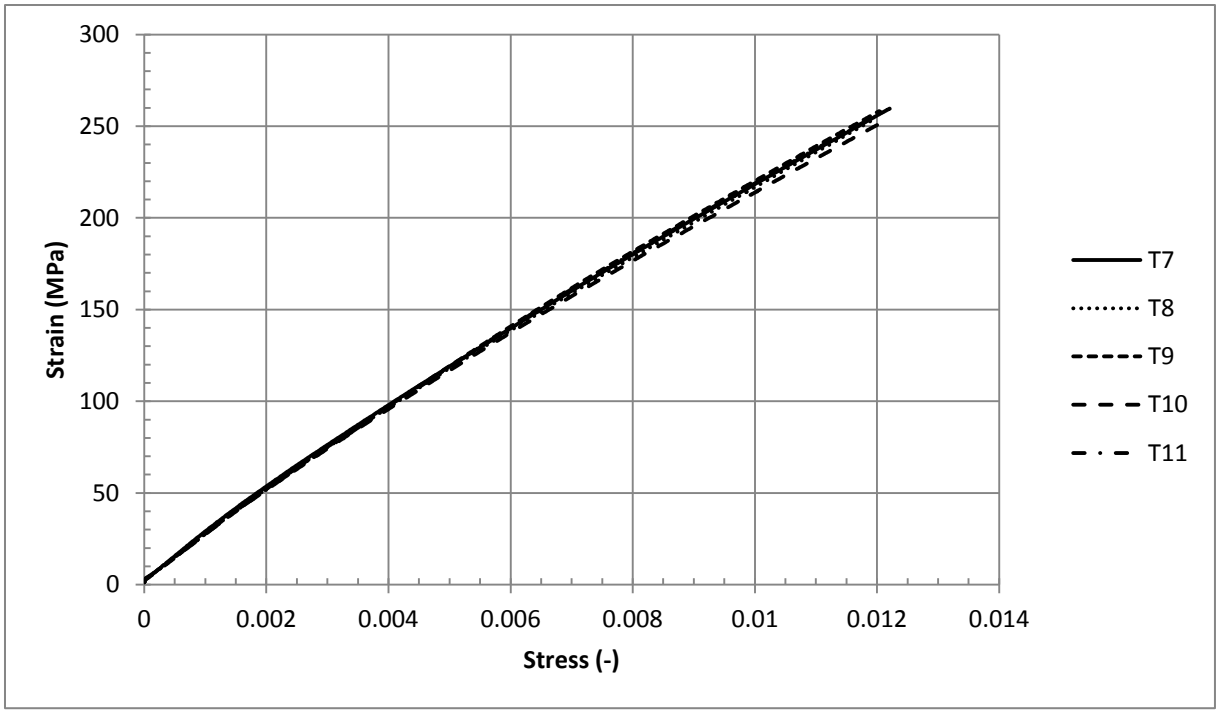

Figure 2 | Stress-Strain Curve (0°-direction).

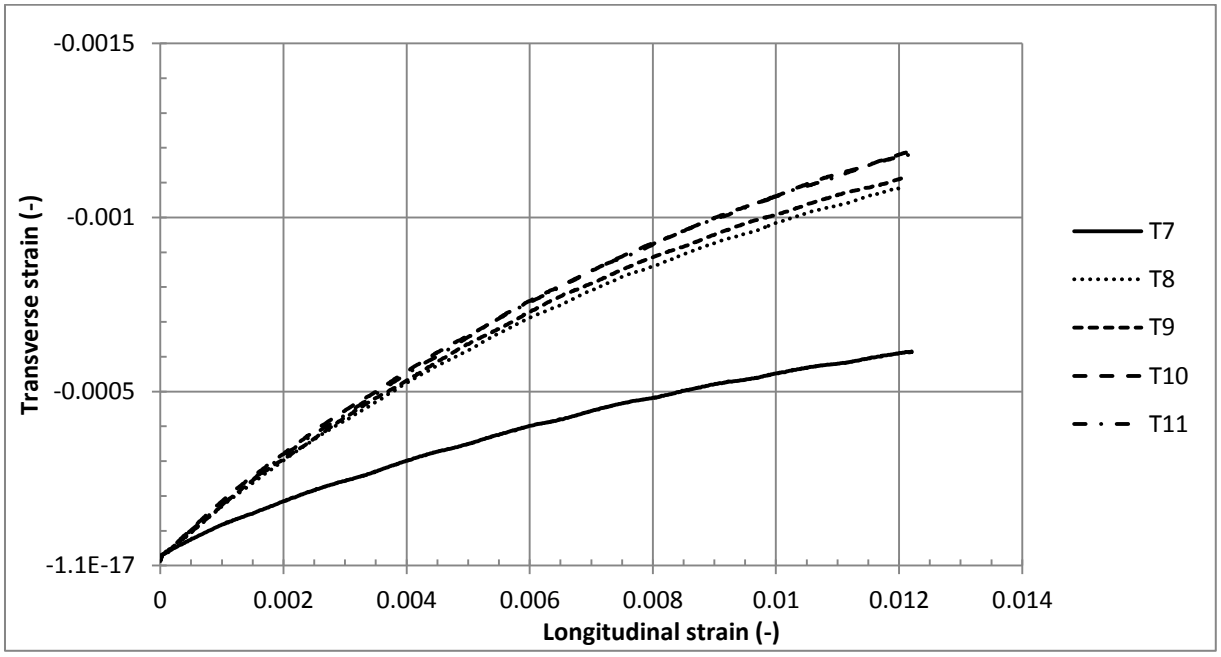

Figure 3 | Transverse strain as a function of longitudinal strain (0°-direction).

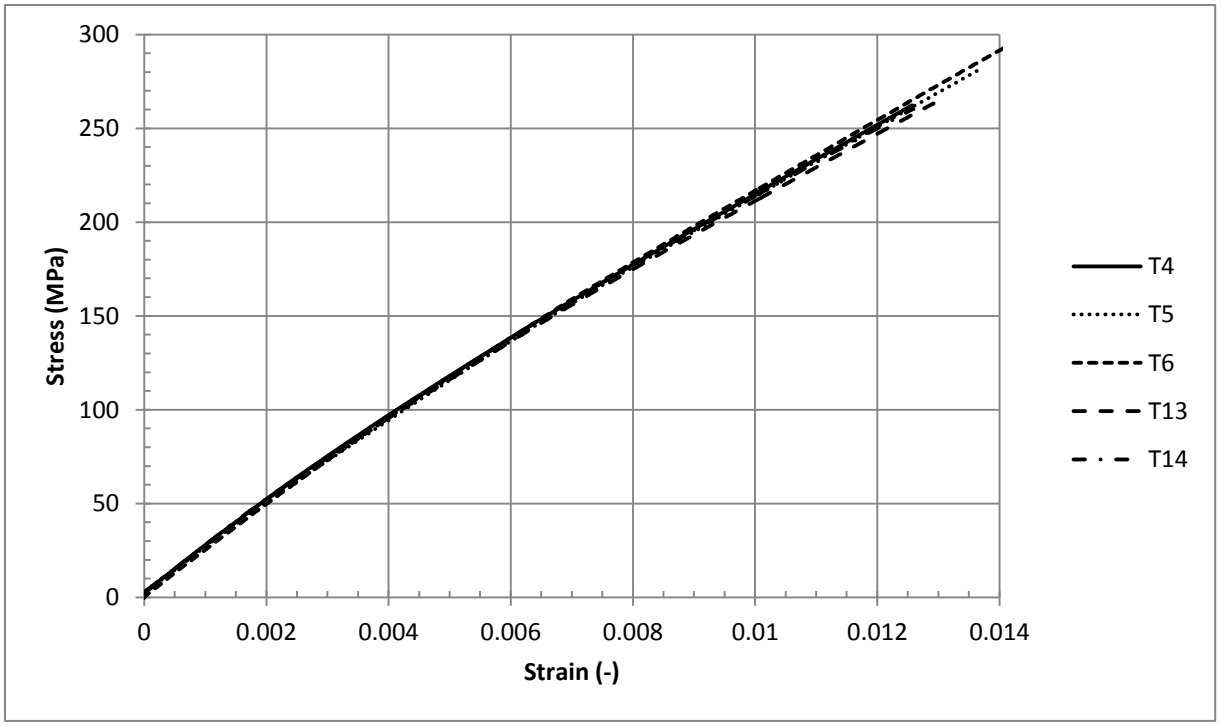

Figure 4 | Stress-Strain Curve (90°-direction).

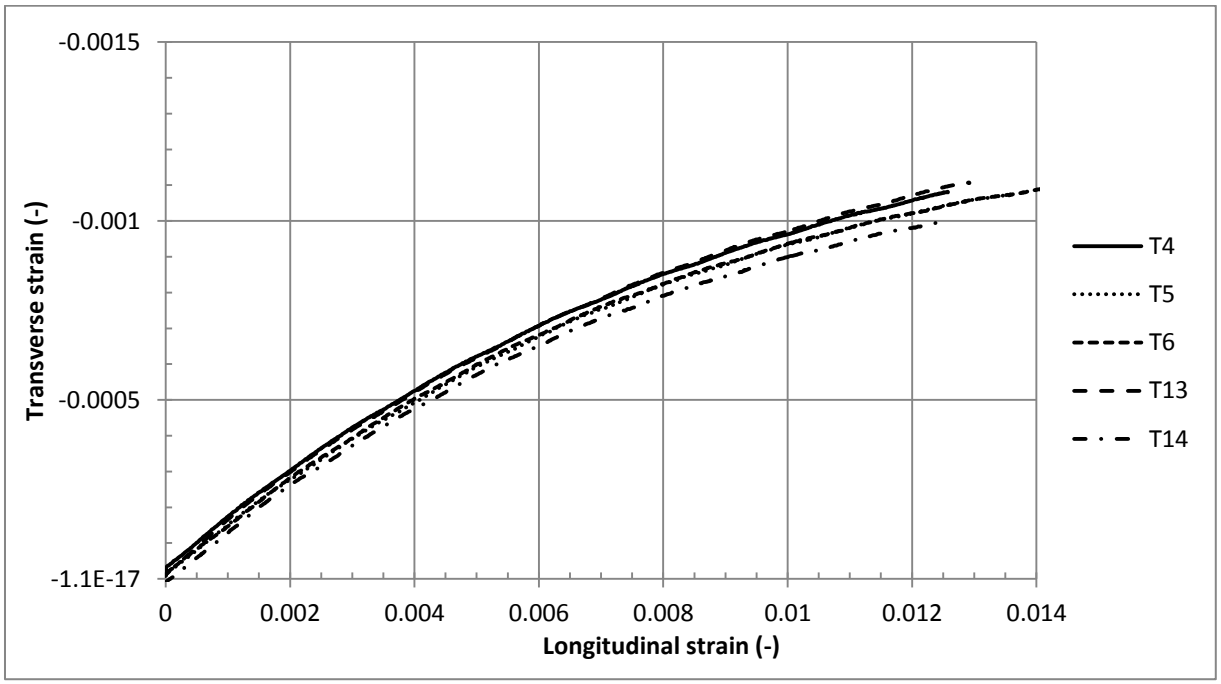

Figure 5 | Transverse strain as a function of longitudinal strain (90°-direction).

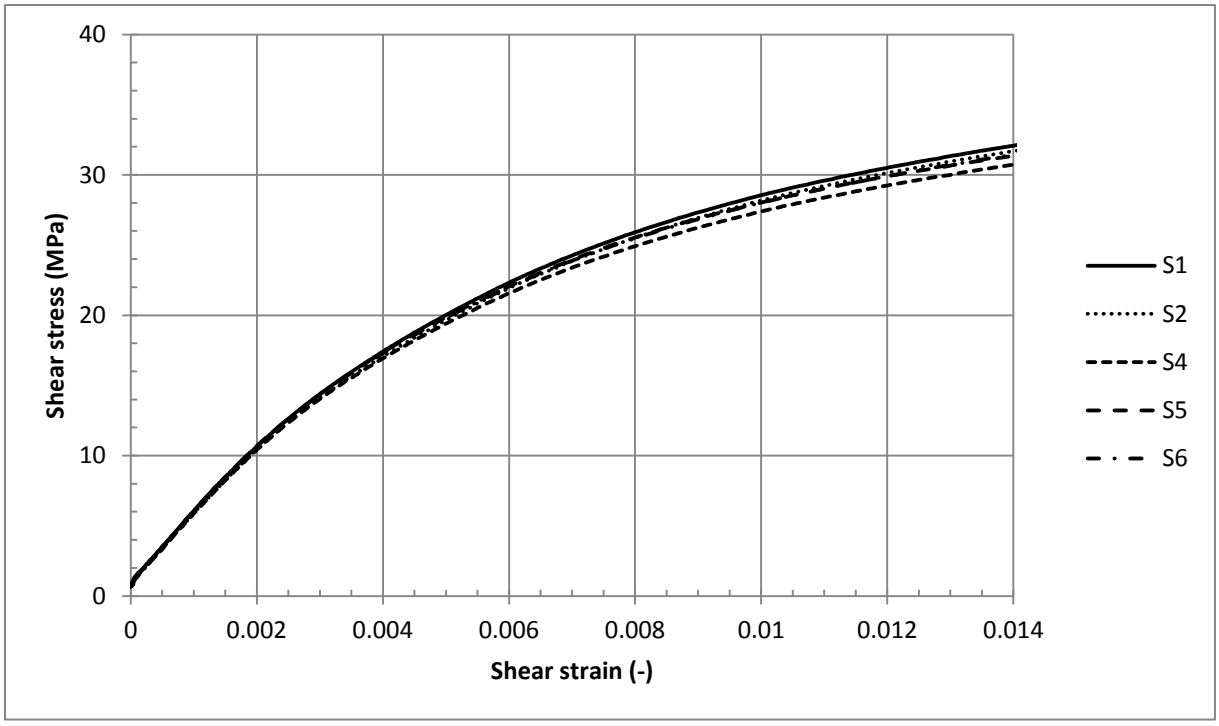

Figure 6 | Shear stress-Shear strain Curve.

Appendix IV. Constituent Content Test Report

Standard	Method II of Methods ASTM D 3171-06
Date of test	26 February 2015
Specimen	Laminate ID 22012015090
	See Coupon preparation
Specimen preparation	The specimen is sanded lightly with P240 emery cloth on the bag-side to remove irregularities due to release foil perforation.

Values used			**Source**
Laminate density	D	1852 kg/m3	Appendix: Laminate Density Test Report
Reinforcement density	ρ_r	2629.6 kg/m3	Hexforce Technical Fabrics Handbook
Matrix density	ρ_m	1150 kg/m3	Hexion Datasheet
Fabric areal weight	A_r	0.2 kg/m2	Hexforce datasheet
Number of plies	N	16	

Measurements

Specimen weight	M	5.78E-02 kg
Specimen thickness	t_1	2.71 mm
Equipment used: Dial indicator	t_2	2.67 mm
	t_3	2.66 mm
	t_4	2.68 mm
	t_5	2.71 mm
	t_6	2.72 mm
	t_7	2.71 mm
	t_8	2.71 mm
	t_9	2.70 mm
	t_{10}	2.72 mm
	t_M	2.70E-03 m
Specimen width	w_1	6.95E-02 m
Equipment used: Caliper	w_2	6.99E-02 m
	w_3	6.97E-02 m
	w_M	6.97E-02 m
Specimen length	l_1	0.1700 m
Equipment used: ruler	l_2	0.1705 m
	l_3	0.1700 m
	l_M	0.1702 m

Calculations

Specimen area	A	1.19E-02	m2
Specimen density	ρ_c	1852	kg/m3
Reinforcement content, weight percent	W_r	63.99	%
Reinforcement content, volume percent	V_r	45.07	%
Matrix content, weight percent	W_m	36.01	%
Matrix content, volume percent	V_m	54.93	%
Cured ply thickness	h_p	0.000169	m

Remarks

Matrix and reinforcement content (volume percent) add up to 102%, not 100%, because reported densities are datasheet values. The actual constituent densities are not determined here. For the purpose of this study, the reinforcement density is taken to be the fixed value. The density of the matrix is more likely to deviate from the datasheet value due to processing parameters.

A picture of the sample is given in Figure 1.

Figure 1: Sample for determination of constituent content.

Appendix V. Laminate Density Test Report

Standard	Method A of Methods ASTM D 792-00
Date of test	26 February 2015
Specimen	See Figure 1

Measurements and calculations

Water temperature	T_w [°C]	22.7
Water density	D_w [kg/m^3]	997.6118

		D2	D5	Mean	s
Apparent mass in air	a [g]	3.192	3.066	3.129	0.0891
Apparent mass in water	b [g]	1.472	1.413	1.443	0.0417
Specific gravity (@23ºC)	sp gr [-]	1.856	1.855	1.856	0.0007
Density specimen (@23ºC)	D^{23C} [kg/m^3]	1852	1851	1852	0.7071
Specific gravity (@23ºC)	sp gr 23/23°C	1.857	1.856	1.857	0.0007

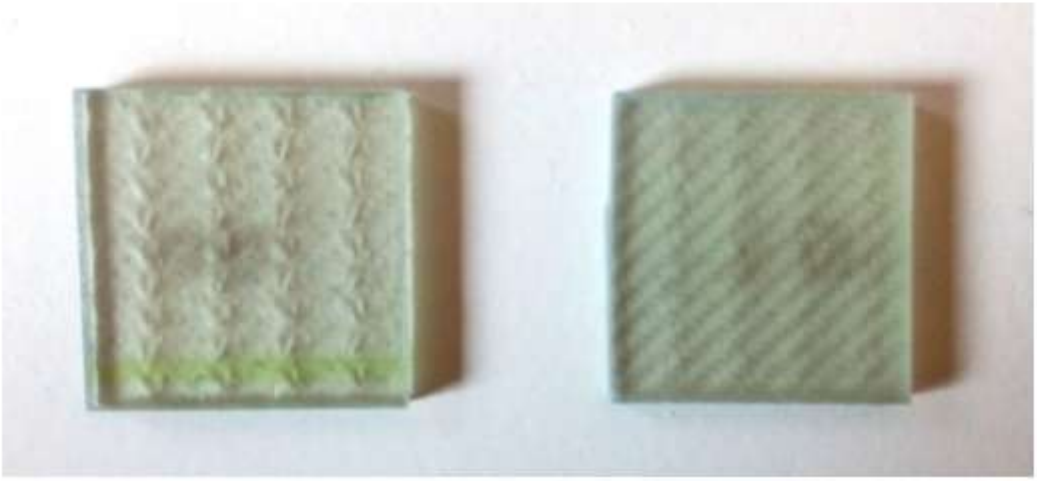

Figure 1: Specimen for determination of density.

Appendix VI. Sandwich Coupon Production

1. General information:	
f. Name:	**Ewoud Aaij**
g. Date:	**26-02-2015** **05-03-2015** **19-03-2015**
h. Location:	**Delft DASML**
i. Laminate ID (dd_mm_yyyy__number):	**26022015SW1** **05032015SW2** **19032015SW3**
2. Fibre:	
a. Fibre type: (Glass, carbon, etc.)	**Glass**
b. Manufacturer:	**Hexcel**
c. Manufacturers' identification code:	**Hexforce 01035 1200 Z6040**
d. Batch & roll number:	**Batch 85M208142632z**
e. Fibre properties:	
▪ Weave style (Satin, plain, UD, etc):	**Twill 2/2**
▪ Sizing:	**Z6040 – epoxy silane**
▪ Fibre areal weight:	**200 g/m^2**
h. Lay-up:	**[0°/CORE/0°]**
i. Laminate length & width (cm):	**26022015SW1: 40x30** **05032015SW2: 30x50** **19032015SW3: 60x50**
3. Core	
a. Core type:	**Foam (PMI)**
b. Manufacturer:	**Evonik**
c. Manufacturers' identification code:	**Rohacell 110A**
d. Batch & roll number:	**81406359**
e. Core properties:	
▪ Density (kg/m^3):	**106.6**
▪ Thickness (mm):	**2**
f. core length & width (cm):	**26022015SW1: 30x30** **05032015SW2: 50x50** **19032015SW3: 50x50**
4. Resin + hardener:	
e. Name:	**Epikote 04908**
f. Manufacturer:	**Hexion**
g. Batch number:	**Resin: DG4M40122A** **Hardener: DG3D70073A**
h. Mixing ratio:	**100:30 parts by weight**
5. Consumables:	
g. Type of peel ply and/or release film:	**-**
h. Type and size of flow mesh:	**White** **Ce-sense BSP white**
i. Type of vacuum bag:	**Clear** **WL 5400**
j. Type of sealant tape:	**Black** **AT 199**
k. Type and length of tube:	**PE 9mm inner diameter**

	Length 300 cm
l. Type and length of spiral:	**-**
6. Resin preparation:	
p. Amount of part A used (grams):	**26022015SW1: 400** **05032015SW2: 665** **19032015SW3: 670.5**
q. Amount of part B used (grams):	**26022015SW1: 120** **05032015SW2: 199** **19032015SW3: 202**
r. Amount of additional parts used (grams):	**-**
s. Mixing time:	**10 min**
t. Amount of time degassed:	**30 min**
u. Vacuum pressure during degassing:	**2 mBar**
v. Resin left-over after infusion (grams):	**26022015SW1: 170** **05032015SW2: 520** **19032015SW3: 290**
7. Production:	
w. Temperature and humidity (ºC/%RH):	**26022015SW1: 21.8 °C / 41 %RH** **05032015SW2: 21.2 °C / 32 %RH** **19032015SW3: 23 °C / 34 %RH**
x. Leak at max. vacuum (mbar/min):	**26022015SW1: 0.13** **05032015SW2: 0.08** **19032015SW3: 0.00**
y. Injection pressure (mbar):	**26022015SW1: 53** **05032015SW2: 49** **19032015SW3: 53**
z. Duration of infusion:	**26022015SW1: 0:26** **05032015SW2: 0:29** **19032015SW3: 0:56**
aa. Duration pressure increase before closing inlet:	**0:05**
bb. Curing pressure (mbar):	**26022015SW1: 498** **05032015SW2: 497** **19032015SW3: 500**
cc. Curing under pressure duration:	**26022015SW1: 22:58** **05032015SW2: 24:00** **19032015SW3: 24:00**

8. Results/ other remarks:

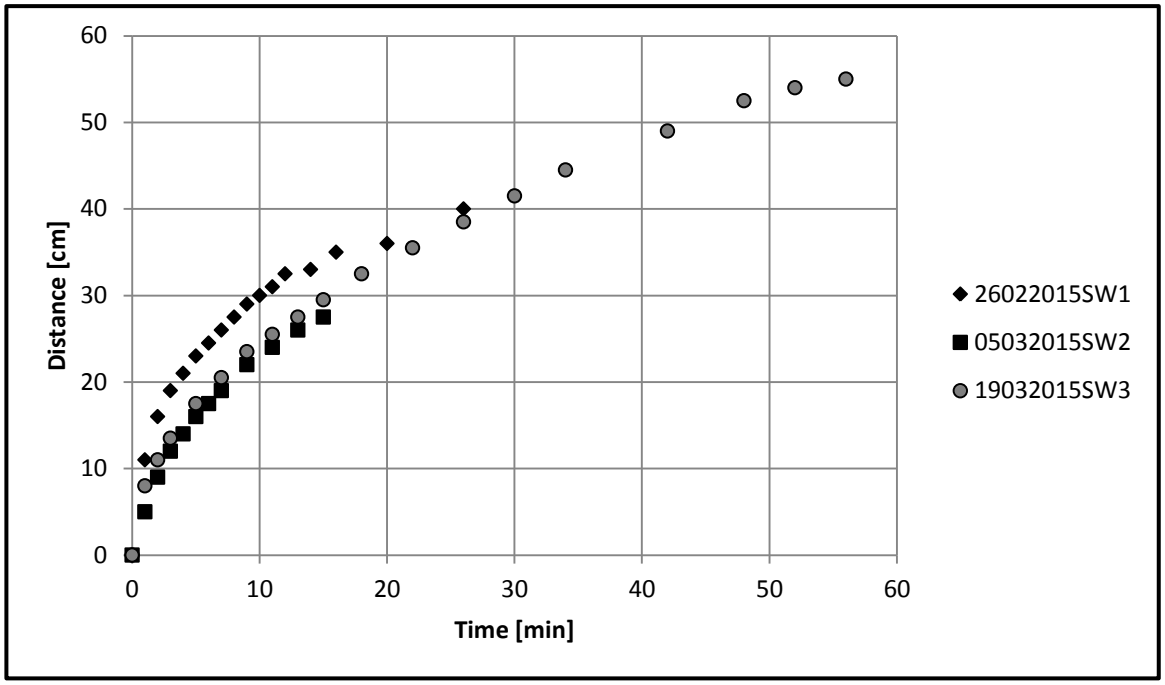

Figure 1 | Infusion speed.

Judging from Figure 1, the infusion speed of double the distance is roughly quadrupled. For example, a panel with infusion distance 1.20m may be expected to require 3:45 hours.

The panels are cut to size with a diamond blade buzz saw after post-curing for 1 week at room temperature. The final dimensions are:

26022015SW1: 24x30 cm
05032015SW2: 24x50 cm
19032015SW3: 2 sections of 24x50 cm, labelled 19032015SW3a and 19032015SW3b

A sketch of the stacking sequence is given in Figure 2. Pictures of the production process are given in Figures 3 and 4.

Vacuum foil is inserted between foam core and glass fabric during lay-up to create separate resin flow in top and bottom skin (see Figure 2).

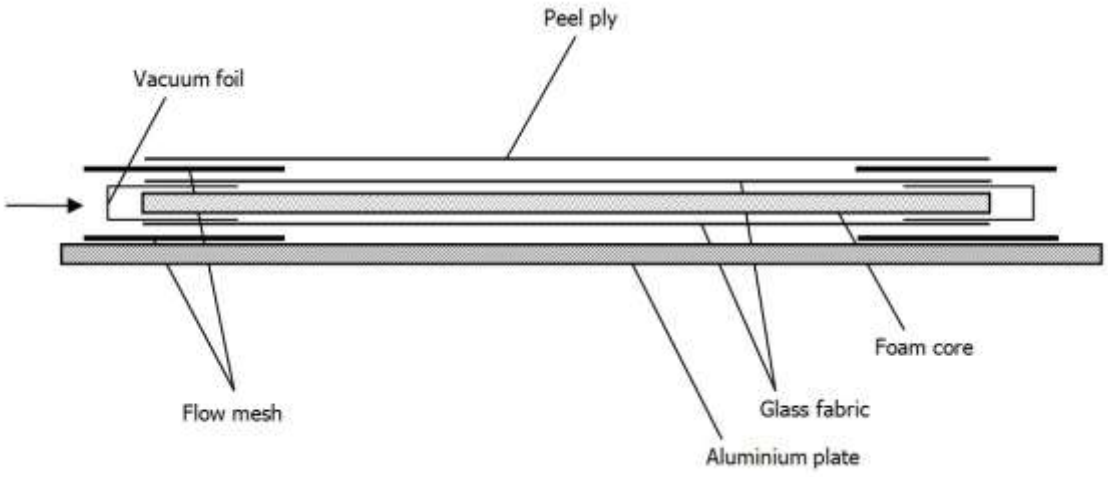

Figure 2 | Laminate build-up. Arrow indicates infusion direction.

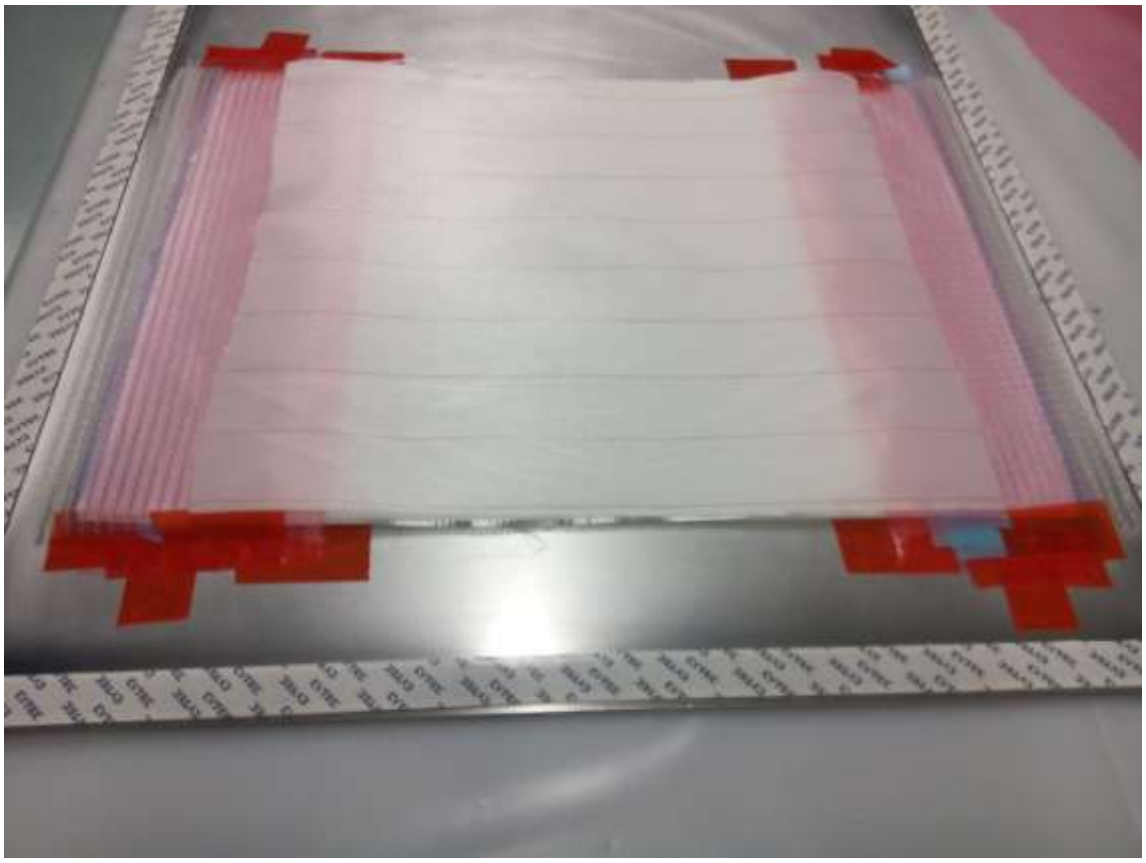

Figure 3 | Dry stack prior to vacuum bagging.

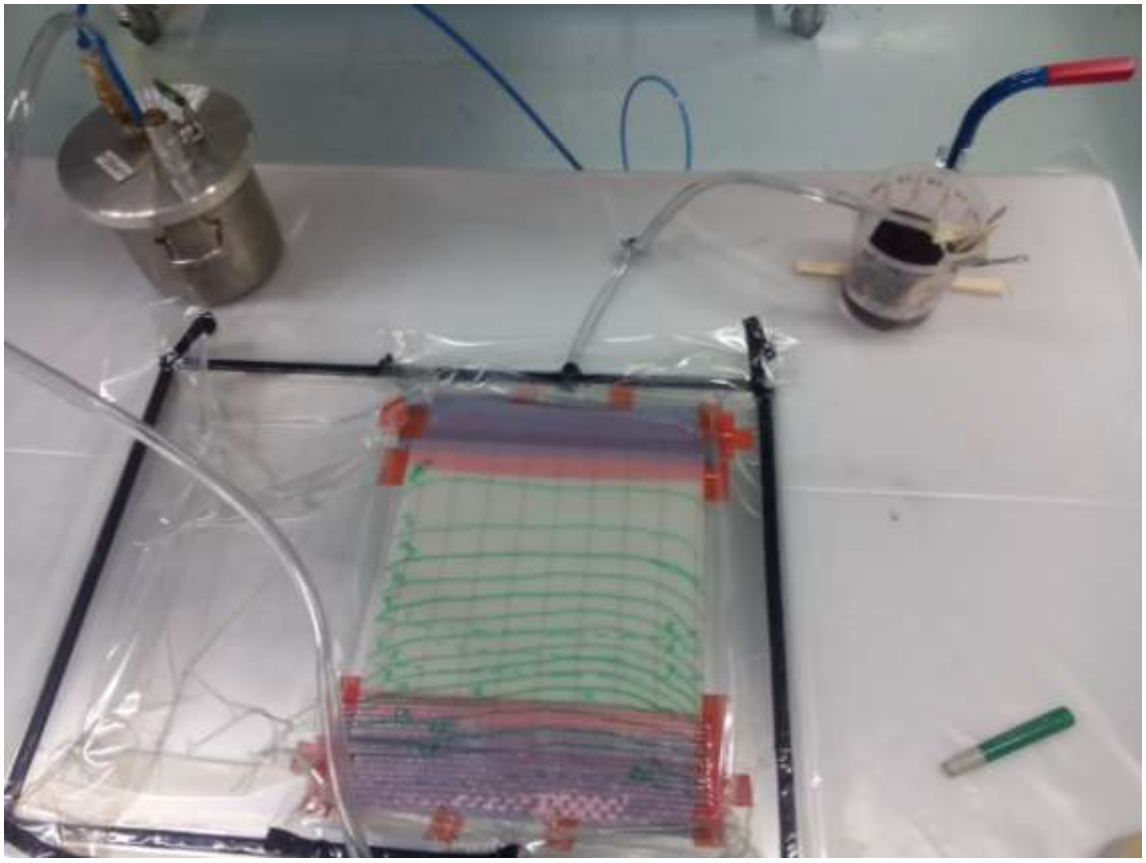

Figure 4 | Infusion after closing of inlet.

Appendix VII. Optical Microscopy Images

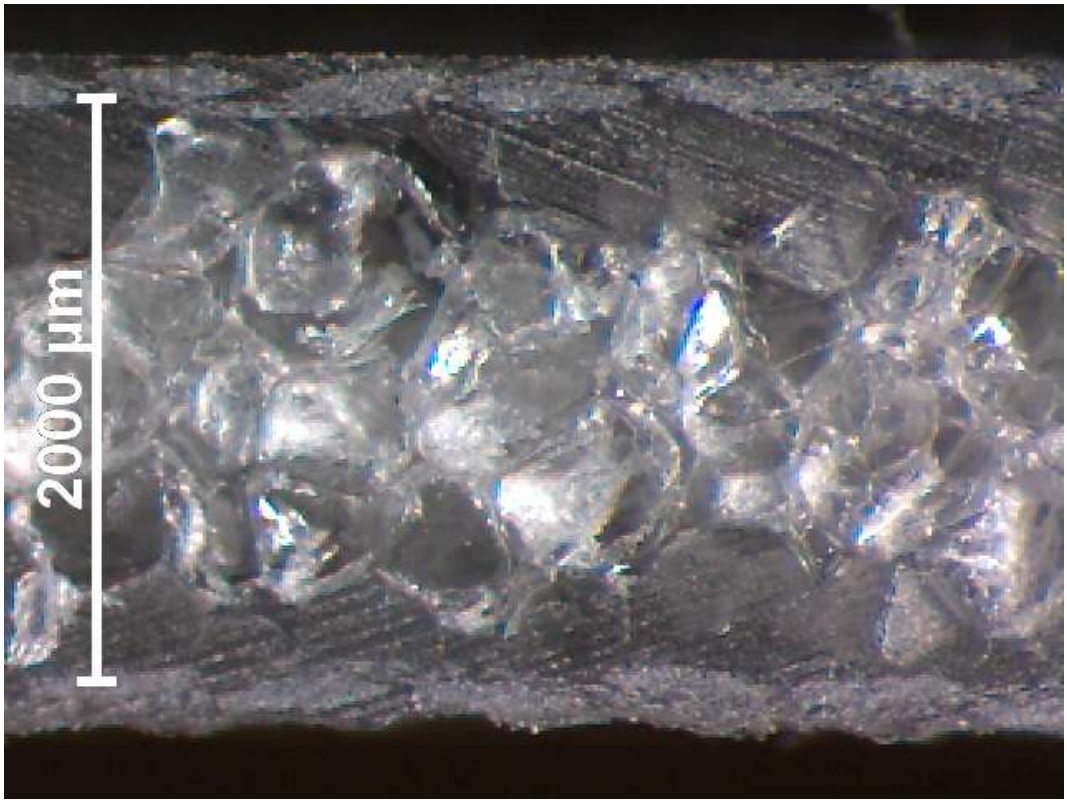

Figure 1 | Specimen 26022015SW1 undamaged.

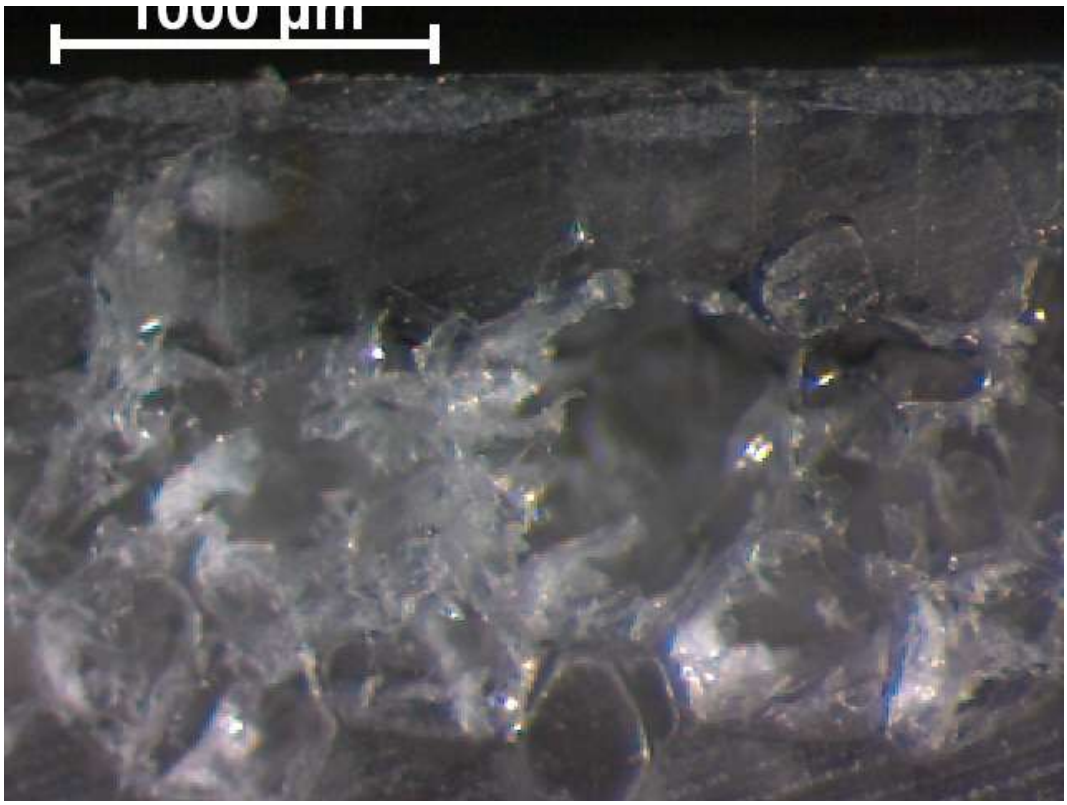

Figure 2 | Specimen 26022015SW1 crushed core at Impact 2.

Appendix VIII. C-Scan Images

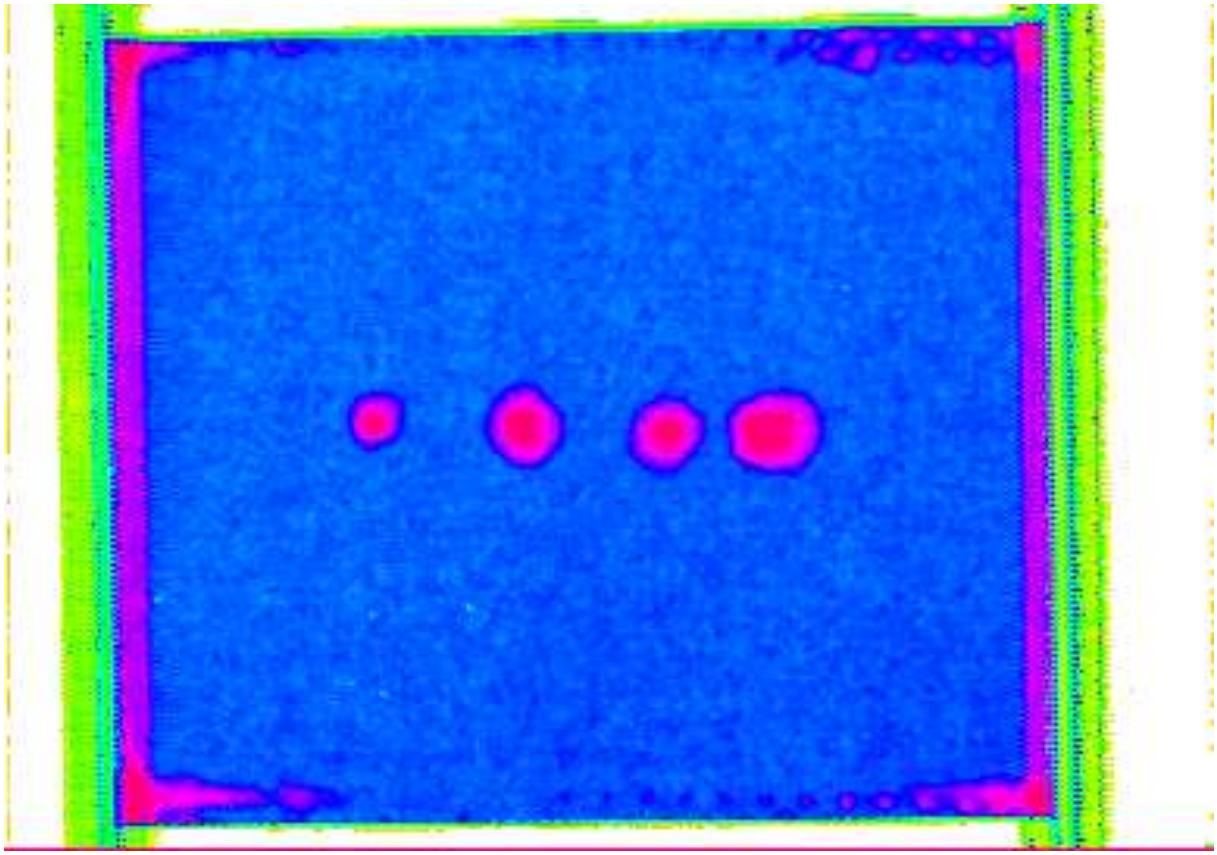

Figure 1 | First impact series, specimen 26022015SW1. Impact numbers from left to right: 4, 3, 2, 1.

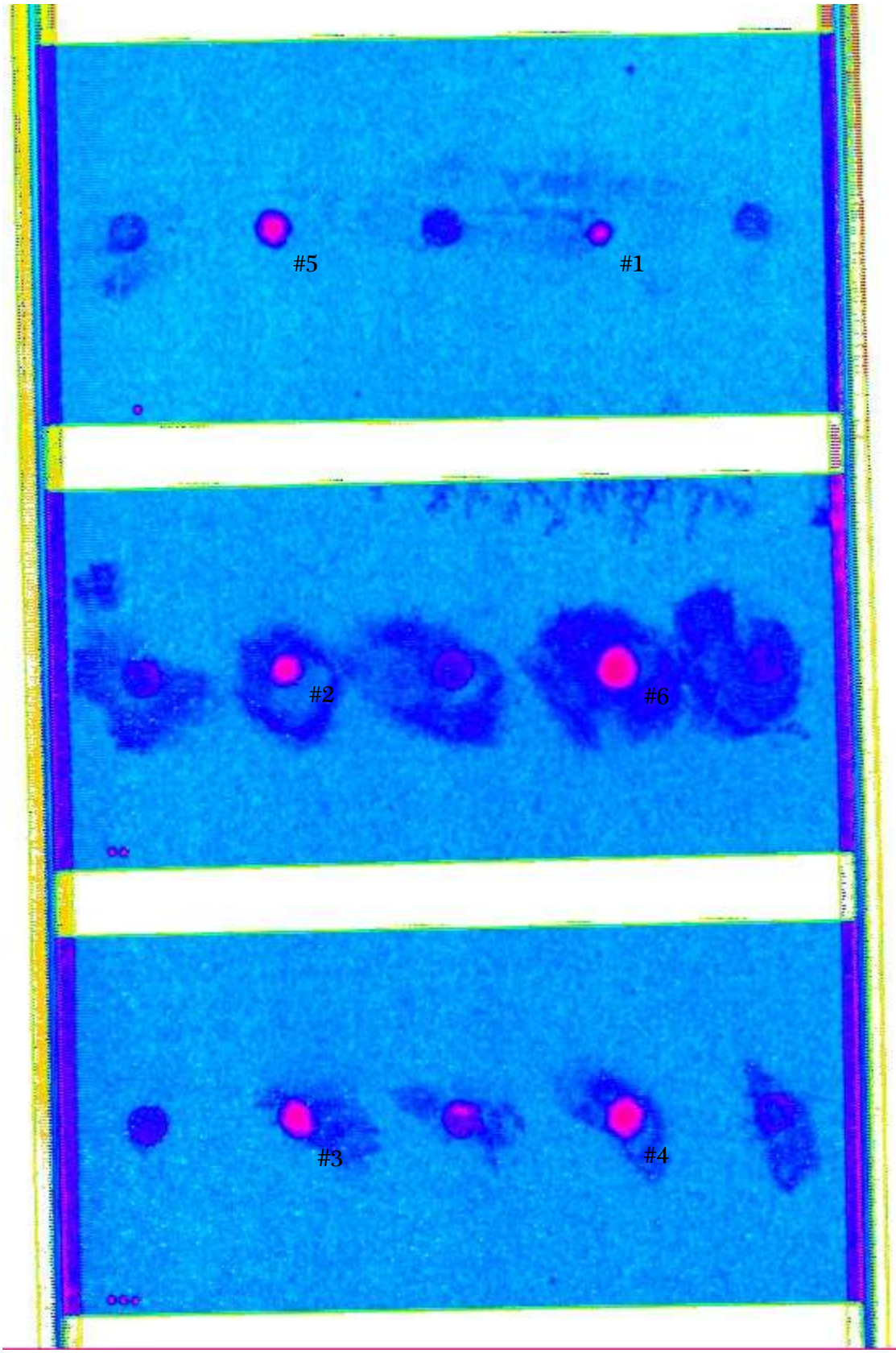

Figure 2 | Second impact series. Impact numbers as given in the figure.